ENERGY BAND ENGINEERING OF COMPLEX METAL OXIDES

GANCHIMEG PERENLEI

A thesis submitted in fulfilment of the requirements for the degree of

Doctor of Philosophy

School of Chemistry, Physics and Mechanical Engineering,

Science and Engineering Faculty,

Queensland University of Technology

Brisbane

2015

ABSTRACT

Solar energy is the ideal energy source for photocatalysis since it is clean, cost-effective and renewable. Capture of this energy requires a low cost material with a tailored band gap, matched to the solar frequency spectrum. A commonly used method for capturing lower energy photons is narrowing the band gaps of UV-active semiconductors. In general, complex metal oxides are ideal candidates when designing new types of visible-light-active catalyst materials.

Bi_2O_3-based complex materials have been selected in this investigation due to their versatile structure, which accommodates a wide range of compositions. Specifically, the Bi_2O_3-ZnO-Nb_2O_5/Ta_2O_5 systems have been used as parent/initial compounds for the systematic investigation of the effects of substitutions on the electronic band structure. This research has focused on understanding the crystal and electronic structures of the parent compounds before attempting to tune the energy band gaps to lower energy regions by metal substitution. Several transition metals have then been selected as potential substituents based on their relative position in the periodic table.

The selected substituents have then been introduced into the parent crystal structure to determine their contributions to the band gap reduction. In this research, all parent and metal substituted compounds have been synthesised and their experimentally measured band gaps have been compared with theoretically calculated band gaps. The photocatalytic ability under UV irradiation of the parent compounds for the decolorization of organic dye in aqueous solution has been examined. Required modifications of such tests for the newly designed materials, due to likely interference of the strong absorbance of dye in the visible light region, are discussed.

KEYWORDS

Complex metal compounds, bismuth oxide-based materials, semiconductor, photocatalyst, energy absorption, crystal structure, electronic structure, band gap, *d*-orbitals, transition metals, cation substitution, density functional theory.

TABLE OF CONTENTS

LIST OF FIGURES

LIST OF TABLES

LIST OF ABBREVIATIONS

AO7	Acid orange 7
BET	Brunauer-Emmett-Teller
BZN	Bismuth zinc niobium oxide
BZTa	Bismuth zinc tantalum oxide
BZV	Bismuth zinc vanadium oxide
BCdN	Bismuth cadmium niobium oxide
BCdT	Bismuth cadmium tantalum oxide
BCdV	Bismuth cadmium vanadium oxide
BCoN	Bismuth cobalt niobium oxide
BCoT	Bismuth cobalt tantalum oxide
BCoV	Bismuth cobalt vanadium oxide
BCuN	Bismuth cupper niobium oxide
BCuT	Bismuth cupper tantalum oxide
BCuV	Bismuth cupper vanadium oxide
BNiN	Bismuth nickel niobium oxide
BNiT	Bismuth nickel tantalum oxide
BNiV	Bismuth nickel vanadium oxide
ca	Circa
°C	Degree Celsius
°2θ	Degrees two theta
CASTEP	Cambridge serial total energy package
CB	Conduction band
CIF	*Crystallographic information file*
DFT	*Density functional theory*

DOS	Density of states
e^-	Electron
EDS	Energy dispersive X-ray spectroscopy
FTIR	<u>Fourier transform infrared</u>
GGA	Generalized gradient approximation
ICSD	Inorganic crystal structure database
IES	Infrared emission spectroscopy
h	Hours
h^+	Hole
Mid-IR	Mid-Infrared
LDA	Local density approximation
MS	Mass spectroscopy
Ox	Oxidation
PBE	Perdew-Burke-Ernzerhof
PDF	*Powder Diffraction File*
Red	Reduction
SEM	Scanning electron microscopy
TGA	Thermo gravimetric analysis
TM	Transition metals
UV	Ultraviolet
VB	Valence band
Vis	Visible light
XRD	X-ray diffraction

DECLARATION OF ORIGINAL AUTHORSHIP

The work contained in this thesis has not been previously submitted to meet requirements for award at this or any other higher education institution. To the best of my knowledge and belief, the thesis contains no material previously published or written by other person except where due reference is made.

QUT Verified Signature

Signature:

Date: _3/11/2015_

ACKNOWLEDGEMENTS

LIST OF PUBLICATIONS

Ganchimeg Perenlei, Peter C. Talbot and Wayde N. Martens. *Sol-Gel Synthesis and Characterization of Cubic Bismuth Zinc Niobium Oxide Nanopowders.* Journal of Nanomaterials, 2014. **2014**(695973): p. 1-6.

Ganchimeg Perenlei, Jose A. Alarco, Peter C. Talbot and Wayde N. Martens. *Electronic Structure Studies and Photocatalytic Properties of Cubic $Bi_{1.5}ZnNb_{1.5}O_7$.* International Journal of Photoenergy, 2015. **2015**(575376): p. 1-11.

Ganchimeg Perenlei, Jose A. Alarco, Peter C. Talbot and Wayde N. Martens. *Synthesis, Characterization and Electronic Structure Studies of Cubic $Bi_{1.5}ZnTa_{1.5}O_7$ for Photocatalytic Applications.* International Journal of Photoenergy, 2015. **2015**(349030): p. 1-8.

Ganchimeg Perenlei, Jose A. Alarco, Peter C. Talbot and Wayde N. Martens, *Synthesis, Optical and Electronic Properties of $Bi_{1.5}CdM_{1.5}O_7$ (M = Nb, Ta).* (Manuscript will be submitted to *RSC Advances*)

Ganchimeg Perenlei, Jose A. Alarco, Peter C. Talbot, and Wayde N. Martens, *Energy Band-Gap Engineering of $Bi_{1.5}MM'_{1.5}O_7$ (M = Zn, Cu, Ni, Co; M' = Ta, Nb, V) Compounds*. (Manuscript will be submitted to *RSC Advances*)

CHAPTER   1

INTRODUCTION

1.1   OUTLINE OF THIS CHAPTER AND THE THESIS

After a brief introduction to the research topics in section 1.2, this chapter includes the research problems that have been investigated during the course of the study, and their rationale (section 1.3). This is followed in section 1.4 by an outline of the research objectives and the aims as defined to respond to the research problems. A schematic of the linkages between chapters and scientific papers, arising from this research throughout the course of the studies is then presented in section 1.5.

This thesis is a collection of research papers based on original work that has been submitted or prepared for submission by the author(s) to various scientific journals. The research papers in Chapters 3, 4 and 5 have been reformatted from the style of the journals to the general format followed in this thesis, but keeping references, scientific and spelling conventions in the style of the journal to which the corresponding work has been submitted. Figure and table numbers in the research papers have been changed to follow the thesis chapter numbers and order. Some repetitions exist between introductory and aspects of the experimental sections of several of the papers, as they are required to stand alone for publications.

1.2   BRIEF INTRODUCTION TO THE RESEARCH TOPICS

Semiconductor photocatalysis has received tremendous attention over the past few decades, as it may provide viable solutions for environmental pollution issues. The efficient and cost-effective conversion of sunlight into useful chemical energy is one of the most challenging, current scientific problems. Most photocatalysts have wide band gaps, which limit not only their effective utilisation of solar energy, but also their use in practical applications. Thus, the search for new materials that display ideal properties and required band gaps has become the main focus of photocatalytic research for efficient harvesting of solar energy. Several strategies for designing highly efficient, visible-light-absorbing photocatalysts have been developed in recent years. Cation doping into wide band gap semiconductors to narrow their band gaps is one of the most commonly used techniques.

This research investigates the optical absorption properties and the electronic band structures of Bi_2O_3-based complex materials. Design and fabrication of visible-light-active photocatalysts is pursued via tuning the appropriate energy band to lower energy regions using metal substituents in the crystal structures of wide band gap semiconductor materials. The research has been conducted using Bi_2O_3-ZnO-Nb_2O_5/Ta_2O_5 systems as parent/initial/starting structures, since these compounds demonstrate potential for a wide range of *d*-metal substitutions. This thesis shows main reasons why these structures have been selected for this research to make visible-light-responsive materials by modifying their electronic structures by transition metal substitutions into their crystal structures.

This work reviews the concepts of photocatalysis and semiconductors. It then examines previous attempts to narrow the band gaps of ultraviolet (UV) active

photocatalysts using various types of dopants, mostly transition metals. Initial parent compound have been synthesised and optical and photocatalytic properties have been characterised. The effects of different synthetic methods on the properties of the materials and the photocatalytic reaction efficiency have also been studied in this initial phase.

Experience in density functional theory (DFT) calculation of this family of compounds has been built simultaneously, since a predictive theoretical tool is required to elevate the work from a purely empirical approach. Given the initial failure of DFT to obtain band gaps for these materials, this thesis will embark on the question whether this failure is intrinsic to the Local Density Approximation (LDA) or the Generalized Gradient Approximation (GGA) approximations or whether some of the structural assumptions in the Crystallographic Information File (CIF) for selected compounds from the Inorganic Crystal Structure Database (ICSD) may be the source of the problems. Calculations for random solid solutions assumed in the CIF structure files will be compared to calculations assuming substitutions at specific sites and to experimental determinations of the band gaps using optical absorption measurements. These comparisons are then extended to a wide range of *d*-metal substitutions from the same rows and columns in the periodic table, to identify more general trends. The outcome of this research will assist in the understanding of the electronic structures of *d*-metal containing or doped compounds in the Bi_2O_3-based family and help determine the most appropriate substituent cations for tuning of wide band gap semiconductors. This may also clarify several misconceptions regarding the crystal and electronic structures of these complex metal oxides containing 3*d*-transition metals.

1.3 THE RESEARCH PROBLEMS AND RATIONALE OF THE STUDY

Most commercially available photocatalysts exhibit wide band gaps ($\geq$ 3 eV), which are not suitable for the efficient utilisation of the solar spectrum for photocatalytic applications. Thus, an intense search for lower-energy-responsive semiconductor materials has a significant presence in the literature [1]. The discovery of new materials with efficient visible-light absorption, high charge-carrier mobility, and correct band-edge positions is extremely challenging. In recent years, great efforts have been devoted to design narrow band gap photocatalysts through modifications of the electronic structures of the existing wide band gap semiconductors [2, 3].

Synthesising solid solutions and doping the crystal structures of the host materials with foreign elements, particularly transition metals, are among the most common approaches to engineer band gaps [4, 5]. Some controversies exist in the literature regarding the role of transition metal dopants in these materials [6, 7]. Some researchers consider that doping with transition metals in the crystal structure of the host materials will be beneficial by narrowing the band gap through raising of the valence band (VB) level. Other researchers emphasize that the photocatalytic performance of the host materials will be degraded due to introduction of localized *d*-orbitals as impurity bands, which will act as traps for electron and holes, resulting in low carrier mobility [6]. These assumptions have generally been inferred from experiments; however, systematic theoretical analyses on the effect of transition metal substitutions on the electronic band structure are scarce in the literature.

The literature shows that co-doping with more than one element simultaneously is more effective than mono-doping [8, 9]. However, in most cases, mono-dopants have

been made into a single site of the crystal structure (either *A* or *B* site) of the host materials. The selection of a suitable parent material is essential to systematically investigate the effect of transition metal substitutions.

Complex metal oxide pyrochlores appear to be a good choice, since they can accommodate a wide range of cation substitutions at the *A* and/or *B* sites. Thus, bismuth zinc niobium oxide (BZN) with molecular formula $Bi_{1.5}ZnNb_{1.5}O_7$ has been selected as parent compound for the systematic investigation of the effects of substitutions on the electronic band structure. Previous research work has thoroughly characterised BZN structurally where microwave properties and potential applications have been investigated; however, optical properties and their connection to the electronic band structure have not been investigated. A study investigated BZN using DFT, but limited itself to the determination of the enthalpy and potential stability of substitutions at specific sites [10].

To engineer band gaps of materials, a thorough understanding of the crystal and electronic structure is necessary, including the contributions of each element and potential substituents. Electronic band structures of complex materials containing 3*d*, 4*d* or 5*d*-metals usually have been analysed with more sophisticated DFT approaches to deal with the strong correlations/localization of the main *d*-electron orbital configurations [11]. The electronic band structure calculations of many crystal structures containing *d*-orbitals, using standard DFT have therefore been considered as unreliable and have remained largely unexplained [12]. However, in this case, the absence of any band gap at all in the initial *d*-metal containing compounds investigated appears to be caused by the assumption of random solid solutions. Our calculations indicate that this may not accurately represent the materials.

1.4   THE RESEARCH OBJECTIVES AND AIMS

The overall objective of this study has been to develop new type of visible-light-sensitive photocatalysts by controlling the band gaps. A primary aim of this research has been to investigate the crystal and electronic structures of complex metal oxides based on bismuth oxide and to further narrow their band gaps by substituting other cations into their crystal structures. The specific aims of the study have been the following:

- To review related literature on wide band gap photocatalysts, to identify band gap reduction methods, and to clarify controversial topics in the relevant literature.

- To select the parent compounds and to investigate their crystal and electronic structures using computational techniques, such as DFT calculations.

- To identify the suitable cations to substitute into the crystal structure of the parent compound to tune their electronic structures to obtain narrow band gaps.

- To prepare the parent and modified materials and to characterise their crystal structures and optical properties using techniques, such as XRD and UV-Vis spectroscopy.

- To compare the experimentally measured and theoretically calculated results to optimise the band gap engineering techniques and to observe the effect of cation substitutions in the crystal and electronic structures.

- To investigate the photocatalytic ability of the prepared materials for practical applications, such as water purification.

1.5   LINKAGE BETWEEN THESIS CHAPTERS AND RESEARCH PAPERS

Chapter 1: Introduction
(General introduction of thesis, thesis outline, research problems, research objectives, and linkage of the thesis chapters and research

Chapter 2: Literature review
(Concept of photocatalysis, wide band gap photocatalysts, some methods to modify their electronic structures, and issues with DFT calculations of band gaps)

Chapter 3: Results and discussion (includes 2 papers)
(Preparation and characterisations of parent material, investigation of optical properties, calculations of electronic structure and photocatalytic application)

Chapter 4: Results and discussion (includes 1 paper)
(Change of main cations at the *B* site in the crystal structure of the parent material, its synthesis, studies of optical and photocatalytic properties, and electronic structure calculations)

Chapter 5: Results and discussion (includes 2 papers)
(Effect of systematic substitutions of transition metals into the crystal structure of the parent material, and investigations of optical properties and electronic structures)

Chapter 6: Conclusions and future work
(General conclusions of the thesis, research outcomes and relevance, some recommended future work resulting from this research)

Figure 1-1: Flow chart of the chapters and the linkage of scientific papers in this thesis (arrows indicate interactions of the chapters and dashed arrows indicate connection between related scientific papers)

1.6   REFERENCES

1.   Tong, H., *et al.*, *Nano-photocatalytic materials: Possibilities and challenges.* Advanced Materials, 2012.

2.   Zhou, B., *et al.*, *Visible-light sensitive cobalt-doped $BiVO_4$ (Co-$BiVO_4$) photocatalytic composites for the degradation of methylene blue dye in dilute aqueous solutions.* Applied Catalysis B: Environmental, 2010. **99**(1): p. 214-221.

3.   Ye, J. and Z. Zou, *Visible light sensitive photocatalysts $In_{1-x}M_xTaO_4$ (M= 3d transition-metal) and their activity controlling factors.* Journal of Physics and Chemistry of Solids, 2005. **66**(2): p. 266-273.

4.   Zaleska, A., *Doped-TiO_2: a review.* Recent Patents on Engineering, 2008. **2**(3): p. 157-164.

5.   Fuerte, A., *et al.*, *Visible light-activated nanosized doped-TiO_2 photocatalysts.* Chemical Communications, 2001(24): p. 2718-2719.

6.   Herrmann, J.-M., *Fundamentals and misconceptions in photocatalysis.* Journal of Photochemistry and Photobiology A: Chemistry, 2010. **216**(2): p. 85-93.

7.   Kudo, A. and Y. Miseki, *Heterogeneous photocatalyst materials for water splitting.* Chem. Soc. Rev., 2008. **38**(1): p. 253-278.

8.   Almeida, C.G., *et al.*, *Photocatalytic hydrogen production with visible light over Mo and Cr-doped $BiNb(Ta)O_4$.* International journal of hydrogen energy, 2014. **39**(3): p. 1220-1227.

9.   Nisar, J., *et al.*, *Mo-and N-doped $BiNbO_4$ for photocatalysis applications.* Appl. Phys. Lett. , 2011. **99**(5): p. 051909-051909-3.

10.   Hinojosa, B.B., *Atomic structure effects on bulk and surface properties of mixed metal oxides from first principles simulations.* 2010, University of Florida.

11.   Zaanen, J., G. Sawatzky, and J. Allen, *Band gaps and electronic structure of transition-metal compounds.* Physical Review Letters, 1985. **55**(4): p. 418.

12.   Calaminici, P., *et al.*, *Density functional theory optimized basis sets for gradient corrected functionals: 3d transition metal systems.* Journal of Chemical Physics, 2007. **126**(4): p. 44108-44300.

CHAPTER 2

LITERATURE REVIEW

2.1   FUNDAMENTALS OF PHOTOCATALYSIS

Photocatalysis is a rapidly growing field of research. The multi-disciplinary nature of the field of photocatalysis has recently expanded to include photochemistry, electrochemistry, radiochemistry, physical chemistry, material science, surface science, chemical engineering and other disciplines [1]. The significance of photocatalysis is that it may offer viable solutions for major environmental problems, which directly affect human health. Applications of this technology are widespread; however, significant applications are hydrogen production via solar water splitting, organic photochemical reactions, and, air and water purification [2-4].

Photocatalysis can be defined as the acceleration of a photoreaction in the presence of a catalyst. There are two types of photocatalytic processes: homogeneous and heterogeneous. In homogeneous photocatalysis, the reactants and the catalysts exist in the same phase [5]. Homogeneous photocatalysis is usually based on a direct photolysis process and most common photocatalysts are hydrogen peroxide (H_2O_2/UV), ozone (O_3/UV), and the photo-Fenton system (Fe^{3+}/H_2O_2/UV) [6]. On the other hand, heterogeneous photocatalysis is a commonly used process that involves two active phases including a solid phase (catalyst) and a liquid/gas phase (water/air) under the irradiation of the light. The reaction starts when the catalyst (a semiconductor material) is initially photo-excited by absorbing an incident photon's energy. That event subsequently generates electron-hole pairs (called excitons), which then interact with the molecules on the surface of the semiconductors [7]. To simplify the analysis of the process, a photocatalytic reaction is generally considered to consist of three basic steps: (i) photon absorption; (ii) charge separation and migration; and, (iii) surface reactions.

In the electronic structures of semiconductor catalysts (SC), the conduction band (CB) is separated from the valence band (VB) by a band gap (E_g). Under irradiation by photons with energy equivalent to or higher than the band gap of a particular semiconductor, some electrons (e^-) are excited from the VB to the CB, leaving an equal quantity of empty states, called holes (h^+), in the VB [8, 9]. The photo-generated exciton then migrates to the surface of a particle, where they react with adsorbed species as shown in equations (2.1 – 2.3).

$$SC + h\lambda \longrightarrow SC\ (e^- + h^+) \tag{2.1}$$

$$e^- + Ox_2 \longrightarrow Red_2 \tag{2.2}$$

$$h^+ + Red_2 \longrightarrow Ox_2 \tag{2.3}$$
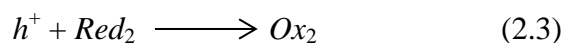
On the surface, electrons and holes act as powerful reductive and oxidising agents, respectively. However, a large proportion of the excitons may recombine in the bulk or at the surface of the semiconductor, resulting in a decrease in photocatalytic activity. The surface characteristics (active sites) and quantity (surface area) play important roles in the photocatalytic reaction [10]. In general, higher surface area of the catalysts yields higher photocatalytic performance. Investigation of the effect of increased surface area and porosity through decreasing particle size of the materials, on the photocatalytic activity has been extensively reported in the literature [11-13]. However, in some cases, high specific area is detrimental to optimum photocatalytic efficiency [14]. Thus, the choice of a suitable synthetic method to prepare catalysts is one of the important factors in photocatalytic research.

Apart from surface properties, the effects of operating parameters such as type, composition, band edge position, charge mobility, dosage of catalyst, light intensity, pH of the solution, type and initial concentration of pollutant, and, the presence of additives such as ions, all influence the application of heterogeneous photocatalysis. For example, in photocatalytic water purification processes, the effect of catalyst loading on degradation of dyes in aqueous solution has been studied and the initial rates have been found to be directly proportional to catalyst concentration [15]. Thus, the catalyst concentration must be optimised for the photodegradation of a particular pollutant in wastewater. The recent report suggested that the optimum catalyst loading of up to 0.4 - 0.5 g/l of TiO_2 should be used for the dye degradation experiment [15]. An excess catalyst concentration beyond the optimum concentration may result in the agglomeration of catalyst particles, hence the part of the catalyst surface become unavailable for photon absorption, and degradation rate decrease [16]. In addition, the ability to utilise the maximum amount of the solar spectrum is one desirable property of catalyst materials due to the cleanliness, cost-effectiveness and renewability of the freely available sunlight for degrading and mineralising recalcitrant organic compounds.

2.2 SEMICONDUCTOR PHOTOCATALYSTS

Recent research focus has been devoted to the discovery and development of novel materials, mostly semiconductors, for photocatalytic technology in the literature. Semiconductor, solid materials exhibit high stability and mobility of charge carriers, which facilitates their transport to the surface where they can interact with absorbed molecules [2, 17]. However, metal-loaded zeolites can also act as photocatalysts by utilising isolated photoactive centres dispersed in a non-absorbing solid matrix, called single-site photocatalysts [18].

Over the past few decades, a large number of semiconductor materials have been investigated for photocatalytic purposes; however, only a few of them have demonstrated significant activity, such as TiO_2, WO_3, Fe_2O_3, NiO, ZnO, ZnS, CdS, GaP and $SrTiO_3$. Among them, TiO_2 is the photocatalyst most extensively used in practical applications which include the detoxification of effluents, disinfection, superhydrophilic self-cleaning, elimination of inorganic/organic gaseous pollutants, and synthesis of organic fuels [19-21]. This extensive applicability is because TiO_2 is chemically and biologically inert, photocatalytically stable, relatively low cost, non-toxic and corrosion resistant [22]. However, TiO_2 (Degussa P25) exhibits a band gap of ~3.2 eV, which corresponds to the absorption wavelength of *ca.* 380 nm, and limits its commercial potential [11, 23]. The energy band diagram of TiO_2, indicating the electron energy as a function of the distance from the surface to the bulk of the solid, is presented in Figure 2-1 [24]. The VB is mainly formed by O 2*p* orbitals, whereas the CB is mainly constituted by Ti 3*d* orbitals.
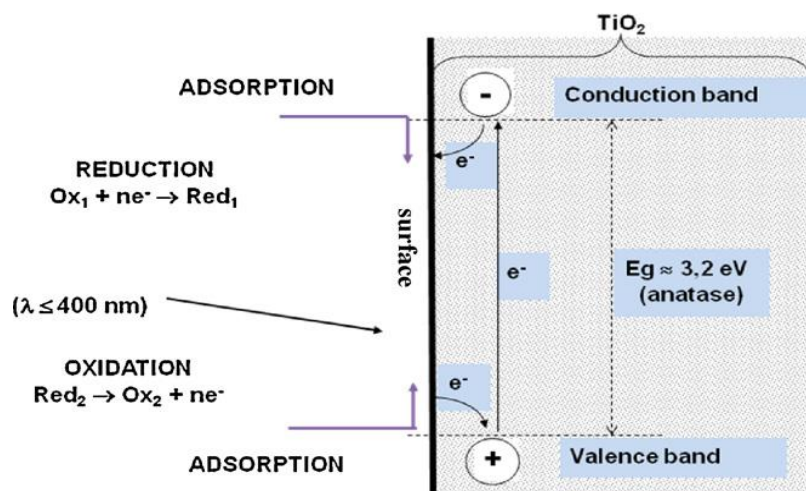
Figure 2-1: Energy band diagram of anatase TiO_2 (Adapted from [24])

Semiconductors, including TiO_2, that have wide band gaps (≥ 3.0 eV), have limited potential for photocatalytic applications. These photocatalysts are only active in the UV light region, which makes up less than 5 % of the total solar radiation. An increasing number of novel photoactive semiconductor materials have therefore been developed in order to overcome the limitations of existing photocatalysts and to improve photocatalytic activity [25]. Thus, great effort has been devoted to the discovery of new semiconducting materials with intrinsic visible photocatalytic activity. The modification of existing UV light photocatalysts, by shifting their absorption band into the visible light range, has attracted much attention for the efficient utilisation of solar or indoor artificial light in the applications of photocatalytic water splitting and organic contaminant degradation [26]. To more effectively reach this goal, present day science requires the combined application of both experimental and theoretical methods in their investigation. Alongside the experimental work, theoretical electronic structure calculations using quantum mechanical simulations have become almost obligatory tools to understand key features, essential for tailoring of new photocatalytic materials.

2.3   ELECTRONIC STRUCTURE ENGINEERING OF SEMICONDUCTORS

Band gap engineering of conventional semiconductors with wide band gaps has been extensively investigated for designing suitable photocatalysts [13, 25, 27]. Several techniques, such as elemental doping and substitution (total or partial) to form solid solutions, have been commonly used for reducing the band gap of oxide semiconductors [28]. Ion (cation or anion) doping of simple oxide is mostly used to narrow their band gaps, while in complex compounds, making solid solutions through cation substitutions, either fully or partially replacing one ion by another is the preferred approach. Modification of the VB or CB to narrow the band gap of semiconductors and extend their absorption of light into the visible region can be introduced individually or simultaneously as shown in Figure 2-2.
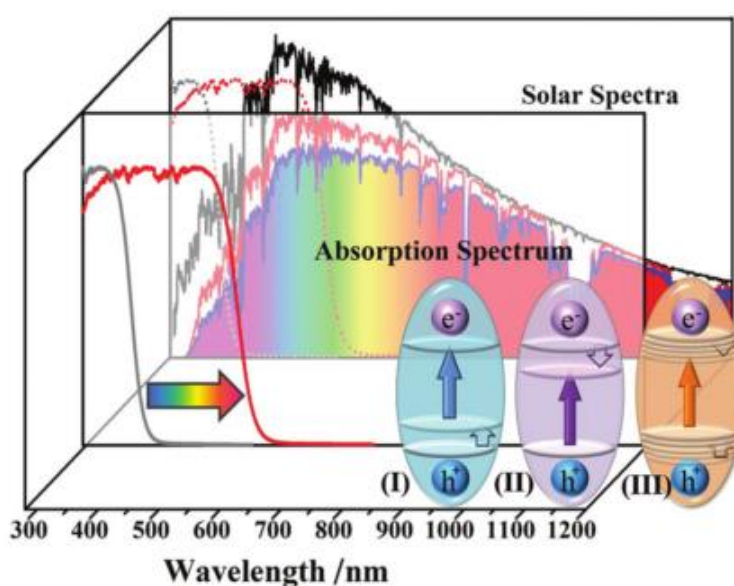
Figure 2-2: Strategies to tailor band structures of semiconductor materials: modification of (I) VB level, (II) CB level and (III) both VB and CB levels

(Adapted from [29])

2.3.1 Doping Method

According to the literature, for simple oxide materials the VB level is more frequently adjusted than the CB level [29]. This may be due to the fact that many semiconductors have relatively fixed CB edge potential. Doping simple oxides, such as TiO_2, with relatively small amounts of metal and non-metal ions has been considered as a good strategy to narrow their band gaps. Various anions, such as N, C, S, and B, have been used as dopants into the crystal structure of TiO_2 [25, 30-33]. Some of these dopants have reduced the original band gaps of the host materials. For instance, it has been suggested that hybridised N $2p$ with O $2p$ states raise the VB orbitals in TiO_2 by 0.2 eV compared to the pure O $2p$ states [32]. However, most others have not shown any significant reduction in the original band gap size of TiO_2 photocatalysts.

On the other hand, cation doping has also been considered for band gap engineering of simple oxide semiconductors. It is believed that cation dopants introduce new states, which act as donor levels above the VB, thus contributing to narrowing the original band gaps. Transition metal ions, such as Sc, Ti, Cr, Mn, Fe, Co, Ni, Cu and Zn, have generally been used as dopants. For example, TiO_2 photocatalyst doped with various cations, such as Cr, Mn, Co, Fe, V, Ag, Au, Pt, Pd and Pb, have been extensively reviewed in the literature [13, 25-27, 34].

More recent reports have shown that the co-doping of more than one cation is more effective than mono-doping in order to minimize the band gap size. Two or more elements have been simultaneously doped into different sites of the crystal structures of various semiconductor materials. In this case, either cation - cation or cation - anion pairs can be used as donor-acceptor pairs to achieve significant shifts of both VB and CB levels. For instance, the comparative studies of co-doped (Mo-N) $BiNbO_4$ have shown much reduced band gap results when compared to that of $BiNbO_4$ mono-doped with cationic (Mo) or anionic (N) [35]. This research has also reported that the co-doped material was more stable than the mono-doped materials.

Moreover, the concentration of dopants needs to be carefully considered to enable the choice of appropriate donor-acceptor combinations. A high concentration of dopants may create impurities in the crystal and electronic band structures, which may cause serious carrier recombination and produce inferior-quality materials. However, the assumptions and elemental behaviours identified above have generally been inferred from experimental results; systematic theoretical analyses on the effect of transition metal ion dopants on the electronic band structure of simple oxide photocatalysts are scarce in the literature.

2.3.2 Substitution Method

In recent years, a variety of semiconductors with increasing degrees of compositional complexity have been investigated for electronic structure modification, since they allow for further tailoring and fine-tuning of properties. Multi-metal oxides, such as Ag^+, Pb^{2+} or Bi^{3+}-based compounds, have received great interest due to their hybridized d^{10} or $d^{10}s^2$ states with O $2p$ states in the VB [29]. It has also been reported that the Bi $6s^2$ states significantly disperse the VB, which facilitates the migration of holes [29, 36].

In substituted complex oxide semiconductors, the energy gap is usually modified by an electron donor level or an upshifted VB level above O $2p$ orbitals. The formation of this new VB level is necessary for oxide photocatalysts [10]. Semiconducting $InTaO_4$ and $BiTaO_4$, doped with $3d$-metal ions, such as Ni and Cu, have also been reported [37, 38]. The authors claim that partially substituted In by Ni ($In_{0.9}Ni_{0.1}TaO_4$) introduces a new band in the visible light region due to the hybridization of Ni $3d$ orbitals with O $2p$ or Ta $5d$ orbitals, and a significantly improved photocatalytic activity by localising the charge carriers when compared to un-doped $InTaO_4$ [37]. Similarly, $BiTa_{1-x}Cu_xO_4$ (x=0.125) has resulted not only in enhanced photocatalytic activity under UV light ($\lambda > 300$ nm) irradiation but also induced visible light ($\lambda > 400$ nm) response. In this case, the band structure indicates that charge transfer upon photoexcitation occurs from the donor levels formed by doped Cu [38].

However, these examples of transition metal ion substituted compounds have generally been experimentally driven and have not been matched with a corresponding level of investigation by electronic band structure modelling. Moreover, to determine the effects of $3d$-metal ion (Zn, Cu, Ni, Co, Fe, Mn, Cr) substitution on the electronic structures and optical properties of the complex compounds, systematic investigation using both experimental and theoretical techniques is necessary in order to know how to reduce the band gaps and maximize the activity of the photocatalysts.

The engineering of CB of complex compounds has also been investigated for certain applications. There are several approaches for modification of CBs of semiconductor materials using metal ion (cation) substitutions in the crystal structures of complex metal oxides. One of the methods to lower the CB minimum is using d-block cations with d^0 electronic configurations. A comparative study of electronic structures and optical properties of $BiMO_4$ and $InMO_4$ (M = V, Nb, Ta) has been carried out using DFT calculations and UV-Vis diffuse spectra in order to understand their different photocatalytic activities [39, 40]. The energy level of V $3d$ in VO_4 is significantly lower than those of Nb $4d$ in NbO_6 and Ta $5d$ in TaO_6 systems [41].

Transition metal ion substitutions in Bi_2GaMO_7 materials (M = V, Sb, Nb, Ta) are other examples of band gap engineering using Bi_2O_3-based pyrochlores. The difference in ionic radii of the cations ($V^{5+} < Sb^{5+} < Nb^{5+} < Ta^{5+}$) brings a change in the lattice parameter of the crystal structure of the semiconductor, which influences the configuration of the CB level in electronic band structure. The band gaps determined from previous studies are 1.95, 2.13, 2.75, 3.01 eV for Bi_2GaSbO_7,

Bi_2GaVO_7, Bi_2GaNbO_7 and Bi_2GaTaO_7 photocatalysts prepared by the solid state reaction route, respectively [42-45].

The substitution of *p*-block cations with a d^{10} electronic configuration in the semiconductor is another effective method for lowering the CB minimum. The effect of IIIA cations substitutions on the optical and photocatalytic properties of $Bi_2MM'O_7$ (M = Al, Ga, In; M' = Nb, Ta) system has been investigated [44, 46, 47]. An increase in the ionic radius of M^{3+} substituents, Al^{3+} (0.57 Å) < Ga^{3+} (0.62 Å) < In^{3+} (0.92 Å), has resulted in an increase in the lattice parameter, but a decrease in the band gap energies of the semiconductors. The band gaps of solid-state synthesised Bi_2MNbO_7 (M=Al, Ga, In) are measured to be 2.9, 2.75 and 2.7 eV, respectively [46].

The substitutions of rare earth cations (R) with partly filled 4*f* levels have also been found to form a new energy level in the band structure of Bi_2RNbO_7 (M = La, Y, Ce, Sm, Dy, Gd, Nd, Pr) [48-50]. It is because the 4*f* band lays above the O 2*p* orbitals in the VB level, thus the R 4*f* to Nb 4*d* optical transition/photon absorption may determine the effective band gap energy of the photocatalysts. A similar trend, where the CB minimum is depressed with increased ionic radii of the metal ions, has also been observed when some alkaline earth metal ions are used as substituents in other types of semiconductor materials [51]. However, most of semiconductors containing IA and IIA cations are only active in the UV or near UV region [52-54].

2.4 DENSITY FUNCITONAL THEORY AND BAND GAP PROBLEMS

The laws of quantum mechanics govern the interactions between atoms and electrons. However, when the systems of atoms and electrons acquire some degree of complexity, accurate and efficient computational tools are required to cope with the difficult calculations. Recent development of computational approaches for quantum mechanical calculations has led researchers to improved understanding of materials properties at an atomistic level. In particular, density functional theory (DFT) is referred to as an ''*ab initio or first principles*'' quantum mechanical simulation technique that explores the ground state properties of crystals, such as total energy, lattice constants, molecular geometry, structural properties, energy band structures, density of states, charge densities, wave functions, optical and surface properties, elastic constants and phonon spectra, in various types of materials [55]. In photocatalytic research, DFT calculations are commonly used in the electronic structure investigations to calculate the band gap of semiconductor materials.

DFT calculated band gaps using the Local Density Approximation (LDA) and Generalized Gradient Approximation (GGA) are known to be significantly smaller than experimentally determined band gap values [56]. In fact, the Kohn-Sham band structure generally underestimates band gaps of many materials by more than 50 % as compared to their optically measured band gaps [57]. The underestimation of band gaps is one of the outstanding problems with DFT, that it is often referred to in the literature as the ''band gap problem'' [58]. In recent years, a few strategies have been developed to solve this problem via more efficient descriptions of the ground state properties. These new approaches tend to become very computationally intensive and could still be considered as work-in-progress, since not many

developments have been published and the suggested new approaches are not regularly used in the literature yet.

The difficulties in band gaps with DFT calculations are particularly apparent in transition metal-based compounds [59]. This may be due to inadequacy of DFT accounting for *d*-orbitals' splitting in tetrahedrally and octahedrally coordinated fields. Significant progress in the understanding of optical, electronic and molecular magnetic properties of complexes of transition metal ions containing open shell *d*-electrons has been achieved using crystal field/ligand field theories. These theories use local coordination symmetry arguments to identify the splitting of originally degenerate levels in spherical symmetry. The splitting of a *d*-orbital in octahedral coordination, as determined with crystal field theory, is illustrated in Figure 2-3 [60].
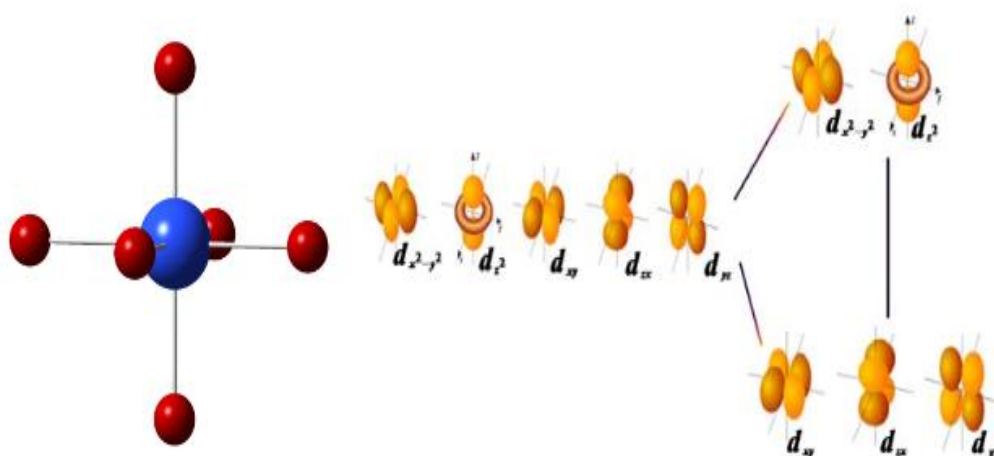
Figure 2-3: Crystal field splitting of *d*-orbitals in octahedral field

(Adapted from [60])

Here, the five *d*-orbitals of an isolated metal ion or atom are degenerate. If a spherically symmetric field of negative charges is placed around the metal ion, the orbitals will remain degenerate, but all of them will be raised in energy as a result of the repulsion between the negatively charged electrons in the orbitals and the additional electronic cloud around the ion.

When the symmetry of the surrounding coordination is taken into consideration, each *d*-orbital is affected differently, and how a particular *d*-orbital is affected can be approximated by assuming the coordinating anions as point charges. This effect is clearly seen in the splitting of the energy levels for the five *d*-orbitals of a metal surrounded by a set of octahedrally coordinated anions. When a negative point charge enters a region of high electron density ($d_{x^2-y^2}$, d_{z^2}), the orbital energy rises significantly owing to the repulsion between the electron density and the negative point charge. When the negative point charge approaches the ion along a nodal surface, the orbital energy does not increase as much (d_{xy}, d_{xz}, d_{yz}).

Therefore, systematic investigations on *d*-metal containing compounds using DFT calculations are necessary for gaining insight into electronic structures of the transition metal-based complex systems in general. This may assist for more accurate calculations of theoretical band gaps for the transition metal doped compounds.

2.5   REFERENCES

1.   Teoh, W.Y., J.A. Scott, and R. Amal, *Progress in heterogeneous photocatalysis: from classical radical chemistry to engineering nanomaterials and solar reactors.* The Journal of Physical Chemistry Letters, 2012. **3**(5): p. 629-639.

2.   Hoffmann, M.R., *et al.*, *Environmental applications of semiconductor photocatalysis.* Chem. Rev. , 1995. **95**(1): p. 69-96.

3.   Bhatkhande, D.S., V.G. Pangarkar, and A.A. Beenackers, *Photocatalytic degradation for environmental applications: A review.* Journal of chemical technology and biotechnology, 2002. **77**(1): p. 102-116.

4.   Tachibana, Y., L. Vayssieres, and J.R. Durrant, *Artificial photosynthesis for solar water-splitting.* Nature Photonics, 2012. **6**(8): p. 511-518.

5.   Amat, A., *et al.*, *Solar photo-catalysis to remove paper mill wastewater pollutants.* Solar Energy, 2005. **79**(4): p. 393-401.

6.   Chanon, M., *Homogeneous photocatalysis* 1997. 426.

7.   Serpone, N., *Brief introductory remarks on heterogeneous photocatalysis.* Sol. Energy Mater. Sol. Cells 1995. **38**(1-4): p. 369-379.

8.   Ryabchuk, V., *Photophysical processes related to photoadsorption and photocatalysis on wide band gap solids: A review.* International Journal of Photoenergy, 2004. **6**(3): p. 95-114.

9.   Serpone, N., A.V. Emeline, and S. Horikoshi, *Photocatalysis and solar energy conversion (chemical aspects).* 2009.

10.   Kudo, A. and Y. Miseki, *Heterogeneous photocatalyst materials for water splitting.* Chem. Soc. Rev., 2008. **38**(1): p. 253-278.

11.   Linsebigler, A.L., G. Lu, and J.T. Yates Jr, *Photocatalysis on TiO$_2$ surfaces: Principles, mechanisms, and selected results.* Chem. Rev. , 1995. **95**(3): p. 735-758.

12.   Zhang, Z., *et al.*, *Role of particle size in nanocrystalline TiO$_2$-based photocatalysts.* J. Phys. Chem. B, 1998. **102**(52): p. 10871-10878.

13.   Fuerte, A., *et al.*, *Visible light-activated nanosized doped-TiO$_2$ photocatalysts.* Chemical Communications, 2001(24): p. 2718-2719.

14.   Saquib, M. and M. Muneer, *TiO$_2$-mediated photocatalytic degradation of a triphenylmethane dye (gentian violet), in aqueous suspensions.* Dyes and Pigments, 2003. **56**(1): p. 37-49.

15.   Akpan, U. and B. Hameed, *Parameters affecting the photocatalytic degradation of dyes using TiO₂ based photocatalysts: A review.* J. Hazard. Mater. , 2009. **170**(2): p. 520-529.

16.   Huang, M., *et al.*, *Photocatalytic discolorization of methyl orange solution by Pt modified TiO₂ loaded on natural zeolite.* Dyes and Pigments, 2008. **77**(2): p. 327-334.

17.   Herrmann, J.M., *Heterogeneous photocatalysis: Fundamentals and applications to the removal of various types of aqueous pollutants.* Catal. Today, 1999. **53**(1): p. 115-129.

18.   Anpo, M., T.-H. Kim, and M. Matsuoka, *The design of Ti-, V-, Cr-oxide single-site catalysts within zeolite frameworks and their photocatalytic reactivity for the decomposition of undesirable molecules—The role of their excited states and reaction mechanisms.* Catalysis Today, 2009. **142**(3): p. 114-124.

19.   Hashimoto, K., H. Irie, and A. Fujishima, *TiO₂ photocatalysis: A historical overview and future prospects.* Japanese Journal of Applied Physics Part 1 Regular Papers Short Notes and Review Papers, 2005. **44**(12): p. 8269.

20.   Paz, Y., *Application of TiO₂ photocatalysis for air treatment: Patents' overview.* Appl. Catal., B: Environmental, 2010. **99**(3): p. 448-460.

21.   McCullagh, C., *et al.*, *The application of TiO₂ photocatalysis for disinfection of water contaminated with pathogenic micro-organisms: A review.* Research on Chemical Intermediates, 2007. **33**(3): p. 359-375.

22.   Carp, O., C.L. Huisman, and A. Reller, *Photoinduced reactivity of titanium dioxide.* Progress in solid state chemistry, 2004. **32**(1): p. 33-177.

23.   Fujishima, A., T.N. Rao, and D.A. Tryk, *Titanium dioxide photocatalysis.* J. Photochem. Photobiol., C: Photochemistry Reviews, 2000. **1**(1): p. 1-21.

24.   Herrmann, J.-M., *Fundamentals and misconceptions in photocatalysis.* Journal of Photochemistry and Photobiology A: Chemistry, 2010. **216**(2): p. 85-93.

25.   Zaleska, A., *Doped-TiO₂: a review.* Recent Patents on Engineering, 2008. **2**(3): p. 157-164.

26.   Yin, W.-J., *et al.*, *Band structure engineering of semiconductors for enhanced photoelectrochemical water splitting: The case of TiO₂.* Physical Review B, 2010. **82**(4): p. 045106.

27.   Yu, H., H. Irie, and K. Hashimoto, *Conduction band energy level control of titanium dioxide: Toward an efficient visible-light-sensitive photocatalyst.* J. Am. Chem. Soc. , 2010. **132**(20): p. 6898-6899.

28. Zou, Z., H. Arakawa, and J. Ye, *Substitution effect of Ta^{5+} by Nb^{5+} on photocatalytic, photophysical, and structural properties of BiTa$_{1-x}$Nb$_x$O$_4$ (0≦ x≦ 1.0).* J. Mater. Res. , 2002. **17**(06): p. 1446-1454.

29. Tong, H., *et al.*, *Nano-photocatalytic materials: Possibilities and challenges.* Advanced Materials, 2012.

30. Chen, X. and C. Burda, *The electronic origin of the visible-light absorption properties of C-, N-and S-doped TiO$_2$ nanomaterials.* J. Am. Chem. Soc. , 2008. **130**(15): p. 5018-5019.

31. Kőrösi, L., *et al.*, *Structural properties and photocatalytic behaviour of phosphate-modified nanocrystalline titania films.* Applied Catalysis B: Environmental, 2007. **77**(1): p. 175-183.

32. Sheng, Y., *et al.*, *Preparation of N-doped TiO$_2$ visible photocatalyst under low temperature via sol-gel process.* Chinese Journal of Inorganic Chemistry, 2008. **24**(1): p. 78.

33. Chen, X. and C. Burda, *The electronic origin of the visible-light absorption properties of C-, N-and S-doped TiO$_2$ nanomaterials.* Journal of the American Chemical Society, 2008. **130**(15): p. 5018-5019.

34. Dvoranova, D., *et al.*, *Investigations of metal-doped titanium dioxide photocatalysts.* Applied Catalysis B: Environmental, 2002. **37**(2): p. 91-105.

35. Nisar, J., *et al.*, *Mo-and N-doped BiNbO$_4$ for photocatalysis applications.* Appl. Phys. Lett. , 2011. **99**(5): p. 051909-051909-3.

36. Oshikiri, M., *et al.*, *Electronic structures of promising photocatalysts InMO (M= V, Nb, Ta) and BiVO for water decomposition in the visible wavelength region.* The Journal of chemical physics, 2002. **117**: p. 7313.

37. Ye, J. and Z. Zou, *Visible light sensitive photocatalysts In$_{1-x}$M$_x$TaO$_4$ (M= 3d transition-metal) and their activity controlling factors.* Journal of Physics and Chemistry of Solids, 2005. **66**(2): p. 266-273.

38. Zhang, H., *et al.*, *Electronic structure and water splitting under visible light irradiation of BiTa$_{1-x}$Cu$_x$O$_4$ (x=0.00–0.04) photocatalysts.* International Journal of Hydrogen Energy, 2009. **34**(9): p. 3631-3638.

39. Ding, K., *et al.*, *Comparative density functional theory study on the electronic and optical properties of BiMO$_4$ (M= V, Nb, Ta).* Journal of Materials Chemistry A, 2014.

40. Li, G.-L. and Z. Yin, *Theoretical insight into the electronic, optical and photocatalytic properties of InMO$_4$ (M= V, Nb, Ta) photocatalysts.* Physical Chemistry Chemical Physics, 2011. **13**(7): p. 2824-2833.

41. Ye, J., *et al.*, *Correlation of crystal and electronic structures with photophysical properties of water splitting photocatalysts InMO4 (M=V^{5+}, Nb^{5+}, Ta^{5+}).* J. Photochem. Photobiol., C: Chemistry, 2002. **148**(1): p. 79-83.

42. Luan, J., N. Guo, and B. Chen, *Hydrogen production with Ga$_2$BiSbO$_7$, Fe$_2$BiSbO$_7$ and Gd$_2$BiSbO$_7$ as photocatalysts under visible light irradiation.* International journal of hydrogen energy, 2014. **39**(3): p. 1228-1236.

43. Luan, J., *et al.*, *Structural and photocatalytic properties of novel Bi$_2$GaVO$_7$.* Materials chemistry and physics, 2007. **104**(1): p. 119-124.

44. Zou, Z., J. Ye, and H. Arakawa, *Preparation, structural and optical properties of a new class of compounds, Bi$_2$MNbO$_7$ (M= Al, Ga, In).* Mater. Sci. Eng., B, 2001. **79**(1): p. 83-85.

45. Wang, J., Z. Zou, and J. Ye, *Surface modification and photocatalytic activity of distorted pyrochlore-type Bi$_2$M (M= In, Ga and Fe) TaO$_7$ photocatalysts.* Journal of Physics and Chemistry of Solids, 2005. **66**(2): p. 349-355.

46. Ropero-Vega, J., *et al.*, *Photophysical and photocatalytic properties of Bi$_2$MNbO$_7$ (M= Al, In, Ga, Fe) thin films prepared by dip-coating.* Mater. Sci. Eng., B, 2010. **174**(1): p. 196-199.

47. Torres-Martinez, L.M., *et al.*, *Bi$_2$MTaO$_7$ (M= Al, Fe, Ga, In) photocatalyst for organic compounds degradation under UV and visible light.* WSeAS Trans environ dev, 2010. **6**: p. 286-295.

48. Zou, Z., J. Ye, and H. Arakawa, *Photocatalytic properties and electronic structure of a novel series of solid photocatalysts, Bi$_2$RNbO$_7$ (R= Y, Rare Earth).* Topics in catalysis, 2003. **22**(1-2): p. 107-110.

49. Zou, Z., J. Ye, and H. Arakawa, *Role of R in Bi$_2$RNbO$_7$ (R= Y, rare earth): Effect on band structure and photocatalytic properties.* The Journal of Physical Chemistry B, 2002. **106**(3): p. 517-520.

50. Li, Y., *et al.*, *Electronic structure and photocatalytic water splitting of lanthanum-doped Bi$_2$AlNbO$_7$.* Materials research bulletin, 2009. **44**(4): p. 741-746.

51. Li, Y., *et al.*, *Electronic structure and photocatalytic properties of ABi$_2$Ta$_2$O$_9$ (A= Ca, Sr, Ba).* Journal of Solid State Chemistry, 2008. **181**(10): p. 2653-2659.

52. Kako, T. and J. Ye, *Photocatalytic decomposition of acetaldehyde over rubidium bismuth niobates under visible light irradiation.* Materials transactions, 2005. **46**(12): p. 2694.

53. Muktha, B., *et al.*, *Synthesis, structure, and photocatalysis in a new structural variant of the aurivillius phase: LiBi$_4$M$_3$O$_{14}$ (M= Nb, Ta).* The Journal of Physical Chemistry B, 2005. **109**(23): p. 11442-11449.

54.   Muktha, B., *et al.*, *Synthesis, structure, and photocatalysis in a new structural variant of the aurivillius phase: LiBi$_4$M$_3$O$_{14}$ (M= Nb, Ta).* The Journal of Physical Chemistry B, 2005. **109**(23): p. 11442-11449.

55.   Harrison, N., *An introduction to density functional theory.* Nato Science Series Sub Series III Computer and Systems Sciences, 2003. **187**: p. 45-70.

56.   Stampfl, C., *et al.*, *Electronic structure and physical properties of early transition metal mononitrides: Density-functional theory LDA, GGA, and screened-exchange LDA FLAPW calculations.* Physical Review B, 2001. **63**(15): p. 155106.

57.   Seidl, A., *et al.*, *Generalized Kohn-Sham schemes and the band-gap problem.* Physical Review B, 1996. **53**(7): p. 3764.

58.   Hohenberg, P. and W. Kohn, *Inhomogeneous electron gas.* Physical review, 1964. **136**(3B): p. B864.

59.   Calaminici, P., *et al.*, *Density functional theory optimized basis sets for gradient corrected functionals: 3d transition metal systems.* Journal of Chemical Physics, 2007. **126**(4): p. 44108-44300.

60.   Gangopadhyay, S., *Density Functional Theory Study of Molecules and Crystals Containing D and F Metals.* 2011, University of Central Florida Orlando, Florida.

CHAPTER 3

SELECTION OF THE PARENT COMPOUND: $Bi_{1.5}ZnNb_{1.5}O_7$ (BZN), ITS SYNTHESIS, OPTICAL ABSORPTION, PHOTOCATALYTIC PROPERTIES AND ELECTRONIC BAND STRUCTURES

3.1   FOREWORD OF THE CHAPTER

In order to develop and design new kinds of visible-light-active photocatalytic materials derived from wide band gap semiconductors, it was necessary to select a parent material and to understand its crystal and electronic band structures. Thus, it was necessary to identify a suitable complex metal oxide, which could be synthesised in a highly pure form and whose crystal structure can preferably incorporate a wide range of metal substitutions without modifying the crystal structure.

After reviewing the literature, cubic $Bi_{1.5}ZnNb_{1.5}O_7$ (BZN), a compound from the Bi_2O_3-ZnO-Nb_2O_5 system has been selected in this research as a parent compound. Cubic BZN is by far the most extensively studied among the pyrochlores and can be synthesised with high purity. The CIF structural file can be obtained from the ICSD database. The literature shows evidence that a wide range of metal dopants have been incorporated into the crystal structure of BZN for improving its dielectric properties. This indicates that the system can be tailored using suitable substituents to make new materials. The literature also indicates that Bi-based compounds are considered good materials for further electronic band structure modification and photocatalytic applications. Their VB energy levels are composed of hybridised Bi $6s$ with O $2p$ orbitals, which may allow for further hybridization with d-orbitals from transition metal substitutions.

Specifically, the cubic BZN crystal structure consists mainly of Bi and Nb cations at the *A* and *B* sites, respectively. Zn co-exists in the structure, by substituting each Bi and Nb cation in a 1:3 ratio in the *A* and *B* sites, respectively, resulting in $(Bi_{1.5}Zn_{0.5})(Zn_{0.5}Nb_{1.5})O_7$. Recent literature has also reported that co-doping semiconductors with more than one element simultaneously to reduce their band

gaps is more effective than mono-doping into a single site of the crystal structure of the host materials. This is a condition already fulfilled by BZN, which makes it an ideal choice for this research.

This chapter includes two journal articles that either have been published or accepted for publication. The first research paper discusses the importance of preparing phase pure, chemically homogeneous BZN catalyst materials. This paper also characterises its optical and surface properties, and tests its photocatalytic application for the decolourisation of organic azo-dye in aqueous solution.

The second research paper presents a systematic analysis of the electronic structure of BZN using DFT calculations and compares it with the experimentally determined band gap from optical absorption measurements to establish a reference. All results of the first attempts to calculate the electronic band structure based on the structural assumption of random solid solution provided by CIF file resulted in the absence of a band gap. This raises the question of whether this is a DFT calculation problem or whether the structural assumption is incorrect. To resolve this issue, alternative approaches have been explored, particularly investigation of the occupancy of cation substitutions at specific sites of the structure. This latter assumption introduces new periodicities, which result in slight structural distortions. These crystal structure distortions and corresponding band gap determinations from the DFT calculations are discussed in this chapter.

STATEMENT OF CONTRIBUTION OF CO-AUTHORS

The authors listed below have certified that:

1. They meet the criteria for authorship in that they have participated in the conception, execution, or interpretation, of at least that part of the publication in their field of expertise;
2. They take public responsibility for their part of the publication, except for the responsible author who accepts overall responsibility for the publication;
3. There are no other authors of the publication according to these criteria;
4. Potential conflicts of interest have been disclosed to (a) granting bodies, (b) the editor or publisher of journals or other publications, and (c) the head of the responsible academic unit; and
5. They agree to the use of the publication in the student's thesis and its publication on the QUT e-Prints database consistent with any limitations set by publisher requirements.

In the case of this paper:

Sol-gel Synthesis and Characterization of Cubic Bismuth Zinc Niobium Oxide

Nanopowders

Contributor	Statement of contribution
Ganchimeg Perenlei (PhD candidate)	Conducted all computational and experimental data collection and analysis, and manuscript writing.
Wayde N. Martens (Principal supervisor)	Assisted with experimental analysis and manuscript development.
Peter C. Talbot (Associate supervisor)	Assisted with computational analysis and manuscript development.

Principal Supervisor Confirmation

I have sighted e-mail or other correspondence from all Co-authors confirming and certifying authorship.

Wayde Martens		4/11/15
Name	Signature	Date

3.2   ARTICLE 1: ''SOL-GEL SYNTHESIS AND CHARACTERIZATION OF CUBIC BISMUTH ZINC NIOBIUM OXIDE NANOPOWDERS''

Ganchimeg Perenlei,[1] Peter C. Talbot[1,2] and Wayde N. Martens[1]

[1]*School of Chemical, Physics and Mechanical Engineering, Science and Engineering Faculty,* [2]*Institute for Future Environments, Queensland University of Technology, Brisbane, QLD 4000, Australia*

ABSTRACT

Bismuth zinc niobium oxide (BZN) was successfully synthesized by a diol-based sol-gel reaction utilizing metal acetate and alkoxide precursors. Thermal analysis of a liquid suspension of precursors suggests that the majority of organic precursors decompose at temperatures up to 150 °C, and organic free powders form above 350 °C. The experimental results indicate that a homogeneous gel is obtained at about 200 °C and then converts to a mixture of intermediate oxides at 350 - 400 °C. Finally, single-phased BZN powders are obtained between 500 and 900 °C. The degree of chemical homogeneity as determined by X-ray diffraction (XRD) and Energy Dispersive X-ray Spectroscopy (EDS) mapping is consistent throughout the samples. Elemental analysis indicates that the atomic ratio of metals closely matches a $Bi_{1.5}ZnNb_{1.5}O_7$ composition. Crystallite sizes of the BZN powders calculated from the Scherrer equation are about 33 - 98 nm for the samples prepared at 500 - 700 °C, respectively. The particle and crystallite sizes increase with increased sintering temperature. The estimated band gap of the BZN nanopowders from optical analysis is about 2.60 - 2.75 eV at 500 - 600 °C. The observed phase formations and measured results in this study were compared with those of previous reports.

INTRODUCTION

Bismuth oxide-based pyrochlore materials are of interest for decoupling capacitors, wireless communications, and low-fired high-frequency filter applications due to their dielectric properties. For these applications, the material is required to have a low sintering temperature and chemical compatibility with the metal electrodes such as silver or copper during co-firing. The dielectric properties of pyrochlore materials strongly depend on the chemical composition and sintering conditions [1].

One of the main representatives of bismuth oxide-based pyrochlore compounds is bismuth zinc niobium oxide, Bi_2O_3-ZnO-Nb_2O_5 (BZN). There are two basic phases in the BZN system: cubic structure $Bi_{1.5}ZnNb_{1.5}O_7$ (α phase) and monoclinic structure $Bi_2Zn_{2/3}Nb_{4/3}O_7$ (β phase). Several studies have reported synthesis of various forms of cubic BZN compounds using a variety of synthetic techniques [2–4]. Conventional solid state reaction is the most commonly employed synthesis strategy to prepare both thin film and bulk crystal BZN materials [5, 6]. This technique does not require expensive starting materials and the synthesis process is relatively simple which includes repeated mixing and heating. The main shortcoming of this procedure is that it requires high sintering temperatures (above 950 °C) for an extended period of time which leads to a formation of heterogeneous multiphase particles with large crystal sizes due to the lack of stoichiometric control [7].

In order to overcome this problem, a number of methods have been used to lower the sintering temperature of the BZN. Firing aids such as CuO and SiO_2-B_2O_3 have been used in the BZN powders synthesis process, which have lowered the sintering temperature to 900 and 800 °C, respectively [8, 9]. However, it has been reported that the additives may influence the properties of the final products [10]. Other synthetic techniques, generally called wet chemical, involve the reaction of precursor solutions to prepare the BZN compounds (below 800 °C). Depending on the precursor solutions and solvents, this technique is referred to as a metallo-organic deposition route or aqueous solution-gel route [11-14]. The final powders are found to be phase pure and homogeneous with smaller particle and crystallite sizes compared to those obtained by solid state reaction, as expected for lower crystallization and sintering temperatures.

The purpose of this research was to prepare chemically homogeneous, phase pure cubic BZN powders with small size at low sintering temperature. To this end, a diol-based sol-gel reaction from an alkoxide route has been successfully employed. During the synthesis process, thermal decomposition studies were carried out to determine the approximate temperature when the phase formation occurred. Crystal structure, elemental homogeneity, and crystallite sizes of the powder samples prepared at different temperatures were thoroughly studied utilizing various techniques. The band gap values of the powders were estimated from the optical absorption data to examine its photocatalytic capabilities.

EXPERIMENTAL SECTION

Materials

All starting materials used in this experiment were of analytical grade ($\geq$ 99.9%), purchased from Aldrich (Australia), and used according to the required stoichiometric ratio to prepare cubic BZN structure. Our synthesis process was adapted from the method reported by Singh *et al.,* [12]. Firstly, bismuth acetate $(Bi(CH_3COO)_3)$ was added to a mixture of organic solvents consisting of 1,3-propanediol $(CH_2(CH_2OH)_2)$ and dried glacial acetic acid $(C_2H_4O_2)$, which was stirred at 60 °C. Subsequently, zinc acetate dihydrate $(Zn(CH_3COO)_2 \bullet 2H_2O)$ was added to the mixture and completely dissolved at 100 °C. Niobium ethoxide $(Nb(OC_2H_5)_5)$ was then added dropwise to the mixture to prevent precipitation due to its high reactivity. The mixture was continuously stirred at 60 °C overnight. The final product obtained was a yellowish-white, translucent solution, and referred to as a liquid suspension.

The synthesis was conducted in an argon glovebox due to the moisture sensitivity of alkoxide reagent. The pH of the mixture was adjusted to 6.0 - 6.5 with 1:1 ratio of organic solvents in order to achieve homogeneous polymeric gels. In subsequent experiments, the liquid suspension was slowly heated at a rate of 2 °C min^{-1} and thermally treated at 350 °C for 1h in a box furnace. The sample was subdivided before further heating at 5 °C min^{-1} to enable the subdivided samples to be annealed at different temperatures in the range of 400 - 900 °C for 1h.

Characterization

A small amount of the liquid suspension was placed on an open platinum crucible and heated from room temperature to 1000 °C in air. A TA Instruments Q500 Thermogravimetric Analysis (TGA) was used for this experiment and a heating rate of 5 °C min^{-1} was adopted. Infrared Emission Spectroscopy (IES) analysis was carried out on a Nicolet Nexus FTS-60A FTIR spectrometer modified via replacement of the infrared source with an emission cell. A small amount of sample was placed on the top of a platinum nail surface in a nitrogen-purged cell during heating. Temperature control of • ±2 °C at the operating temperature of the samples was achieved by using a Eurotherm Model 808 proportional temperature controller attached to the thermocouple.

Techniques such as X-ray diffraction (XRD) and backscattered scanning electron microscopy (SEM) combined with Energy-dispersive X-ray spectroscopy (EDS) were used for phase determination and elemental analysis of the powder samples. XRD patterns were collected in Bragg-Brentano geometry using a Philips PANalytical X'Pert PROX-Ray Diffractometer. The incident X-rays were produced from a PW3373/00 Co X-ray tube operating at 40 kV and 40 mA, providing Kα1 wavelength of 1.7903 Å. Diffraction patterns were collected from 5.0 - 90 °2θ with either 0.01 or 0.02 step size, on a spun stage. A LaB$_6$ standard powder was also used as a size/strain standard to calibrate instrumental broadening of diffraction peaks.

Secondary electron and backscattered electron images of the surface of powder samples were captured by a Zeiss Sigma FE-SEM and EDS, operating at 20 kV. All samples were coated with gold before analysis to minimize excessive electron buildup. Elemental ratios of the samples were analysed by Inductively Coupled Plasma with Optical Emission Spectrometers (ICP-OES) analysis. A Perkin Elmer Optima 8300 DV Inductively Coupled Plasma Optical Emission Spectrometer was used for this experiment. To dissolve the samples in acid, a known amount of lithium borate was mixed with powders and fused in platinum crucibles. The fusion products were then dissolved in a mixture of 5 % of nitric acid and 0.5 % hydrofluoric acid. Ultraviolet and Visible (UV-Vis) was used for light absorption analysis from which the band gaps of the samples were calculated. Spectra were recorded on a UV-Vis-NIR Cary 5000 Stheno spectrometer in the 200 to 800 nm region.

RESULTS AND DISCUSSION

Thermal Decomposition

Thermal analysis of a liquid suspension was started from room temperature and completed at 1000 °C. Figure 3-1 shows the dTG/TG analysis results. A large exothermic dTG peak was obtained at 80 and 145 °C, which corresponds to about 83 % of the total mass loss. This large mass loss was due to the evaporation of water and residual organic solvents contained within the precursor solution. The thermal decomposition study revealed that two small dTG peaks were observed at about 250 and 330 °C. This slow and constant mass decay consisted of about 4 % mass loss. The dTG/TG curves show that the main decomposition of the organic precursors occurred just before 150 °C and continuously occurred until 330 °C.
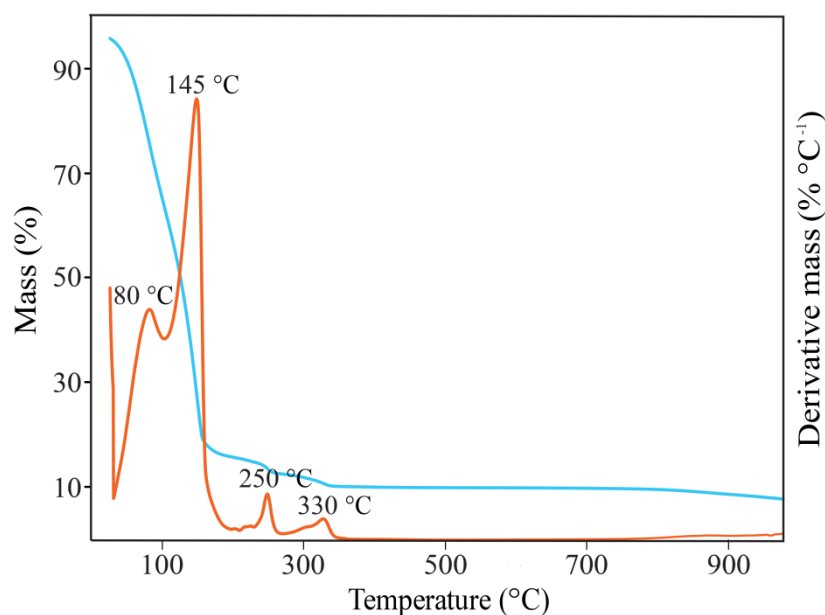
Figure 3-1: TG/dTG curves of the liquid suspension.

This result was quite similar to Wang's reported experimental work [11]. However, there was a weak exothermic peak obtained at about 545 °C, which was not observed in this experimental result. Other authors' works on thermal decomposition of the BZN powders showed that there were significant weight losses observed above 500 °C [13, 14]. From this experiment result, no other significant mass loss was observed from the TG curve as the temperature was increased up to 1000 °C, indicating limited or no volatility of bismuth or other metals. This result suggested that the majority of the organic precursors decomposed before the gel sample formed at about 200 °C, and continued until 350 °C, which resulted in the formation of organic free metal oxide powders.

Infrared Emission Spectroscopy

TGA analysis on the gel sample was further confirmed by IES analysis. Figure 3-2 shows that the sample consisted of residual organic compounds which were completely lost before the dried powder formed at 350 °C. In the IES spectra, the C–C and C–O stretches were observed between 1000 cm^{-1} and 1300 cm^{-1}. Two peaks were also found at 2700 cm^{-1} and 2800 cm^{-1} which were due to either –O–CH_3 or –O–CH_2–O– groups. Moreover, –CH_2 and –CH_3 bands were clearly observed in the spectra at 2850 - 2950 cm^{-1} and 1450 - 1475 cm^{-1}, respectively. These were due to $CH_2(CH_2OH)_2$ and CH_3COOH species in the precursor solution.

As expected, when the sample was heated to 200 - 250 °C, the above mentioned bands were observed in the spectrum but significantly declined in intensity at 300 °C. However, the spectra were relatively featureless after the sample was heated above 350 °C, presumably due to the formation of the metal oxides. Such metal oxides were expected to show features in their vibrational spectrum below the 500 cm^{-1} limit

of the instrument. The IES result suggested that the organic groups from the precursors, as well as water from the reaction, completely evaporated from the liquid suspension as temperature was increased. Thus, organic free metal oxide powders formed from 350 °C onwards.
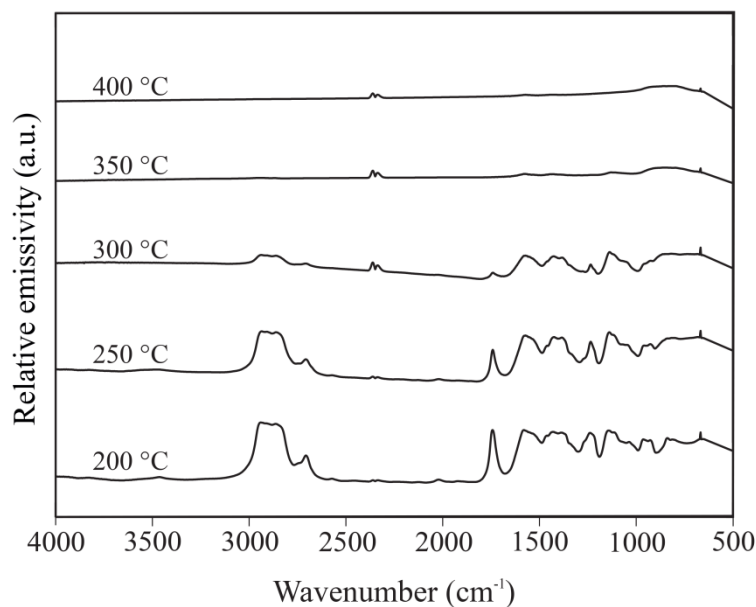
Figure 3-2: IES spectra of the liquid suspension heated from 200 to 400 °C.

Surface Morphology

The backscattered SEM micrograph and EDS mapping images of the powder samples prepared at 400 °C are shown in Figure 3-3. It can be seen from the SEM micrographs that the particles of the powders had sizes ranging from 0.5 to 3 μm. The SEM backscattering image in Figure 3-3(a) also shows some uneven elemental distribution in the sample indicating some phase separation. Elemental analysis on several areas confirmed that the bismuth and niobium atoms were not completely uniformly distributed. The EDS mapping image in Figure 3-3(b) also confirmed this

observation. The distribution of bismuth, niobium and oxygen atoms were even throughout the sample. However, zinc atoms predominated in some areas creating small pockets of impurities. This indicated that the sample contained two or more phases; one mainly consisting of bismuth and niobium atoms, and another which was rich in zinc.

(a)
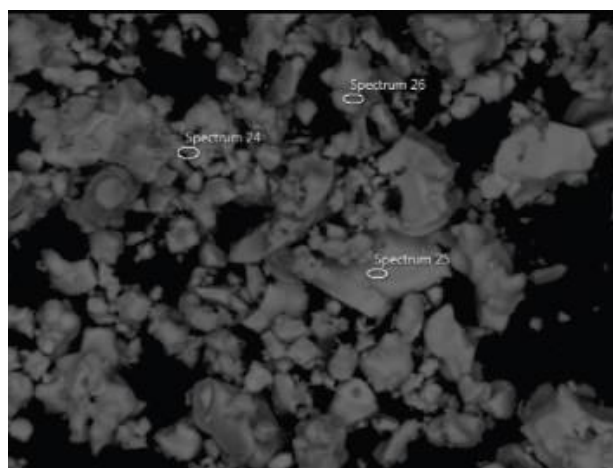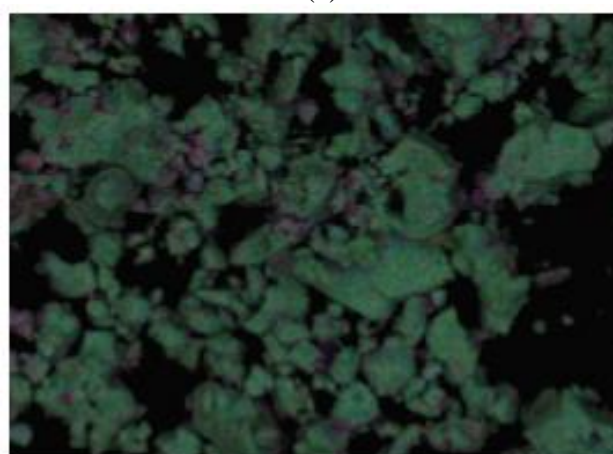
10 μm

(b)

Figure 3-3: Backscattered SEM (a) and EDS mapping (b) images of the powder sample prepared at 400 °C (Bi: blue, Nb: green and Zn: purple).

Figure 3-4 shows SEM micrographs and elemental mapping of the BZN powder samples prepared at 900 °C. It can be seen in Figure 3-4(a) that much bigger microcrystalline particles were present in this sample when compared to particles obtained at lower temperature. Elemental distribution of each metal atom on the surface of the particles looked relatively homogeneous. However, the color differences in the EDS mapping in Figure 3-4(b) clearly showed the presence of small amounts of impurities. These impurities were maybe due to excess of unreacted metals such as zinc or bismuth that were rejected from the BZN particles.

(a)

10 μm
(b)
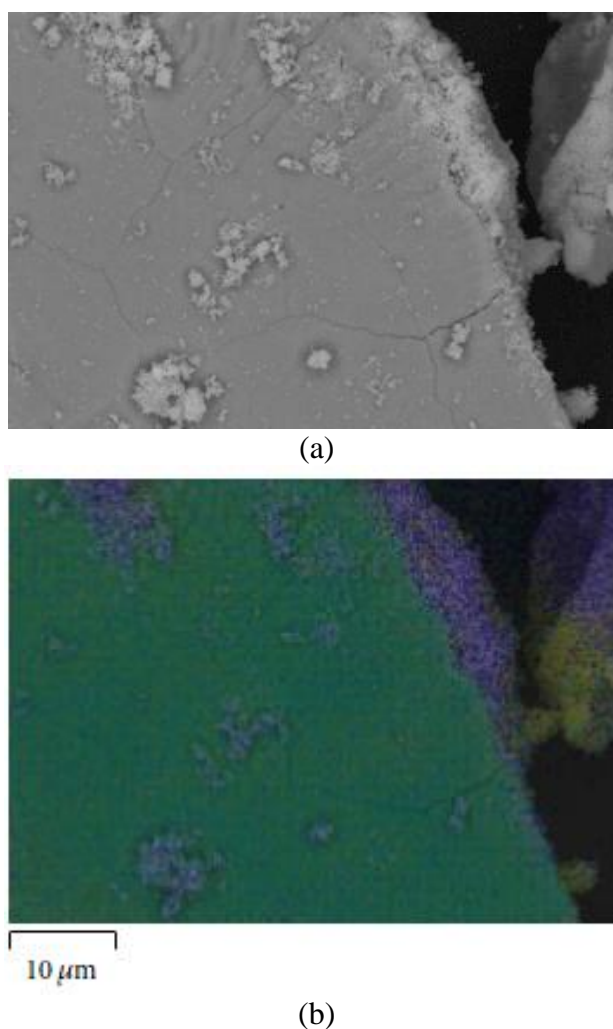
Figure 3-4: Backscattered SEM (a) and EDS mapping (b) images of the BZN powders prepared at 900 °C (Bi: purple, Nb: light blue, and Zn: yellow).

Phase Determination

XRD patterns of the powder samples prepared between 350 and 900 °C are shown in Figure 3-5. The XRD pattern obtained from the sample prepared at 350 °C indicated that the sample contained large amounts of an amorphous phase in addition to a crystalline phase. The obtained pattern matched closely that of orthorhombic bismuth niobium oxide, $Bi_{7.84}Nb_{0.16}O_{12.16}$. The XRD pattern was unchanged when the sample was reheated at 400 °C. This suggested that two binary oxides were formed during low temperature sintering processes. ICP-OES analysis was carried out on the sample and gave as a result: $Bi_{7.84}Nb_{1.61}O_{14.78}$. The difference between the ICP-OES and the XRD pattern suggested that the amorphous phase might be niobium zinc oxide, $Nb_{1.45}ZnO_{2.62}$.
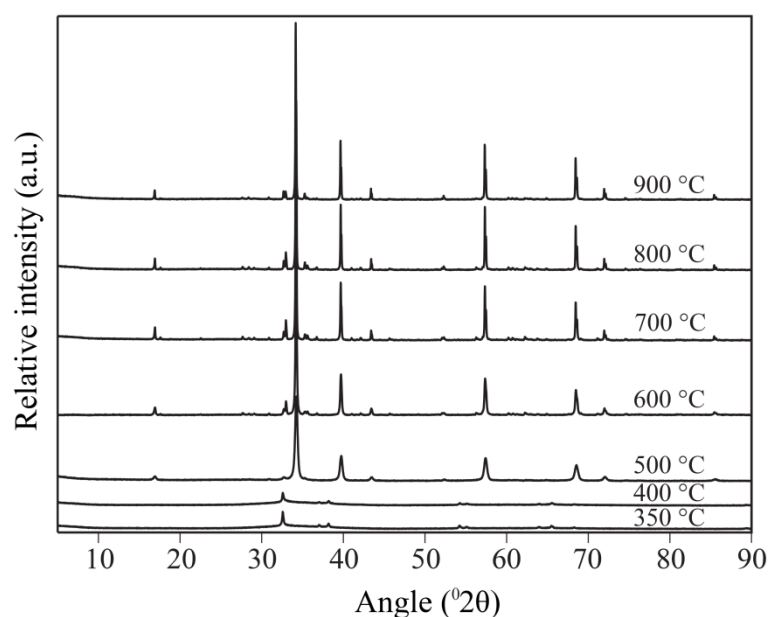
Figure 3-5: XRD patterns of the powder samples at various temperatures

Phase transformation occurred as the sintering temperature was increased. Low temperature intermediate oxides directly converted to the singe-phased crystals from 500 °C onwards. This phase was identified as cubic BZN compound (JCPDS PDF, 00-054-0971). The elemental analysis of the powder sample was carried out by ICP-OES and the result suggested that the atomic ratio was closely matched with cubic $Bi_{1.5}ZnNb_{1.5}O_7$ composition. The observed phase transformation from intermediate oxides to the single phased BZN in this study is slightly different from those of other works [11–14]. The cubic BZN powders formed at 450 °C straight from the precursor gels, and then fully crystallized at 550 - 600 °C [11–14]. In another work, a small amount of residual amorphous phase was obtained besides BZN [14]. Other reports suggested that the cubic BZN phase was obtained at about 500 °C [11, 13]; however, there was a small amount of Bi_2O_3 also present. This was because Bi_2O_3 phase was first formed at 400 °C in those studies.

Nonetheless, the crystals of the BZN powder samples obtained in this study between 500 and 700 °C were phase pure with broad peak widths, indicating small and/or disordered crystallites. The crystallite sizes of the powders were calculated from the Scherrer equation using selected diffraction peaks. The calculated sizes of the powders were 33, 72 and 98 nm for 500, 600 and 700 °C, respectively. This result was similar with reported values of 30 - 90 nm at 450 - 700 °C [11]. However, it was relatively larger than that obtained by another group reporting 13 - 36 nm at 500 - 700 °C [14].

Similarly, the XRD patterns of the powders prepared at higher temperatures, 800 - 900 °C, were also identified as cubic BZN compound. However, small amounts of impurities were found to co-exist with the main BZN phase. Other research has suggested that the low temperature BZN phase might have a composition of $Bi_{1.5}Zn_{0.5}Nb_{1.5}O_{6.8}$ which undergoes a peritectoid decomposition at about 700 °C to high temperature phases of $Bi_{1.5}ZnNb_{1.5}O_7$ and $BiNbO_4$ [15]. In this study, however, the small impurity observed at high temperatures corresponds to ZnO [16]. With increasing temperature, the peak widths significantly narrowed, indicating the formation of larger crystals.

Optical Absorption

The UV-Vis spectra of the powder samples heated at different temperatures of 350 - 600 °C are shown in Figure 3-6. The band gaps of each sample can be estimated from the optical reflectance data to evaluate the direct transition between the valence band and the conduction band. Approximate band gaps of 2.25 - 2.29 eV were estimated form the absorbance spectra of mixed intermediate oxides obtained at 350 - 400 °C. The optical band gap values estimated from extrapolation to zero of absorption versus photon energy plot, and those increased when the sample was prepared at higher temperatures.
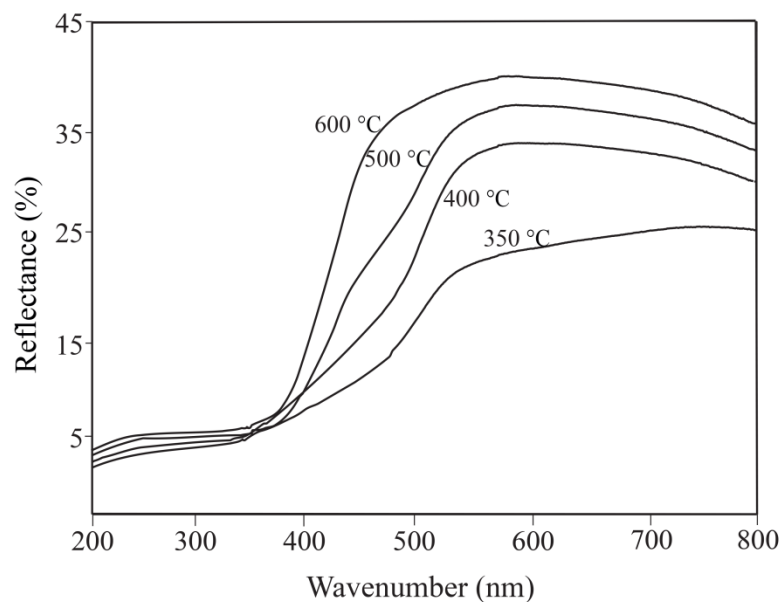
Figure 3-6: UV-Vis spectra of the powder samples at various temperatures.

The optical band gaps of the single-phased BZN powders formed at 500 and 600 °C were 2.60 and 2.75eV, respectively. This result was slightly larger than the reported value by Zanetti *et al.,* (3.0 - 3.1 eV at 500 - 700 °C) [13]. The optical analysis result showed that the band gaps of the samples widened when the powders were prepared at high temperatures of above 600 °C. Such wide band gap values might be caused by the effect of bigger crystallite size due to the high sintering temperature. This study also suggests that the phase pure BZN powders have an optical absorption at wavelengths of 450 nm, indicating that this nanostructured material can be responsive only to the UV/Vis light region.

CONCLUSIONS

A diol-based sol-gel synthesis method was successfully employed for the preparation of phase pure cubic BZN nanopowders. Thermal analysis results showed that most decomposition in the precursors occurred up to 150 °C, and it was completed before 350 °C. The results also indicated that organic free powders were obtained at 350 - 400 °C. Low temperature intermediate oxides were examined by elemental analysis and found to be a mixture of bismuth niobium oxide and niobium zinc oxide. These oxides then directly transformed to the single-phased BZN with increasing temperature. This finding was contrary to that of sol-gel methods in the literature, where a different phase mixture was obtained at low temperature. However, our result was similar to that reported for a solid state method, where the mixture of phases before BZN formation was comparable to ours. Measured crystallite sizes and band gaps of the BZN powders obtained from this study are in close agreement with the reported values. The optical study suggested that the BZN compound may be photoactive in the UV/Vis light region.

REFERENCES

1. Hu, Y. and C.L. Huang, *Structural characterization of Bi–Zn–Nb–O cubic pyrochlores.* Ceram. Int. , 2004. **30**(8): p. 2241-2246.

2. Singh, J. and S. Krupanidhi, *Probing disorder in cubic pyrochlore Bi$_{1.5}$ZnNb$_{1.5}$O$_7$ (BZN) thin films.* Solid State Commun., 2010. **150**(45): p. 2257-2261.

3. Liu, W. and H. Wang, *Sintering and dielectric properties of Bi$_{1.5}$ZnNb$_{1.5}$O$_7$ cubic pyrochlore ceramics via high-energy milling technology.* J. Electroceram. , 2011: p. 1-6.

4. Wang, X*., et al.*, *Effect of KOH concentration on the hydrothermal synthesis of Bi$_{1.5}$ZnNb$_{1.5}$O$_7$ nanopowder.* Electronic Components and Materials, 2009. **4**: p. 004.

5. Kamba, S*., et al.*, *Anomalous broad dielectric relaxation in Bi$_{1.5}$ZnNb$_{1.5}$O$_7$ pyrochlore.* Phys. Rev. B, 2002. **66**(5): p. 054106.

6. Wu, M.C*., et al.*, *Comparison of microwave dielectric behavior between Bi$_{1.5}$Zn$_{0.92}$Nb$_{1.5}$O$_{6.92}$ and Bi$_{1.5}$ZnNb$_{1.5}$O$_7$.* J. Am. Ceram. Soc. , 2006. **26**(10): p. 1889-1893.

7. Nino, J.C*., et al.*, *Transmission electron microscopy investigation of Bi$_2$O$_3$–ZnO–Nb$_2$O$_5$ pyrochlore and related phases.* Mater. Lett. , 2002. **57**(2): p. 414-419.

8. Hong, W*., et al.*, *Effect of SiO$_2$ and B$_2$O$_3$ on structure and dielectric properties of Bi$_2$O$_3$-ZnO-Nb$_2$O$_5$ based ceramics.* Ferroelectr., 1999. **229**(1): p. 285-290.

9. Wu, M.C*., et al.*, *Silver cofirable Bi$_{1.5}$Zn$_{0.92}$Nb$_{1.5}$O$_{6.92}$ microwave ceramics containing CuO-based dopants.* Mater. Chem. Phys. , 2006. **100**(2): p. 391-394.

10. Su, W.F. and S.C. Lin, *Interfacial behaviour between Bi$_{1.5}$ZnNb$_{1.5}$O$_7$x0.02V$_2$O$_5$ and Ag.* J. Eur. Ceram. Soc., 2003. **23**(14): p. 2593-2596.

11. Wang, H*., et al.*, *Bismuth zinc niobate (Bi$_{1.5}$ZnNb$_{1.5}$O$_7$) ceramics derived from metallo-organic decomposition precursor solution.* Solid State Commun., 2004. **132**(7): p. 481-486.

12. Singh, S*., et al.*, *Fabrication and characterization of crystalline cubic bismuth zinc niobate pyrochlore (Bi$_{1.5}$ZnNb$_{1.5}$O$_7$) nanoparticles derived by sol-gel.* Adv. Sci. Lett, 2009. **2**(3): p. 356-359.

13.   Zanetti, S.*, et al.*, *A chemical route for the synthesis of cubic bismuth zinc niobate pyrochlore nanopowders.* J. Solid State Chem. , 2004. **177**(12): p. 4546-4551.

14.   Weihong, L.*, et al.*, *Bi$_{1.5}$ZnNb$_{1.5}$O$_7$ cubic pyrochlore ceramics prepared by aqueous solution–gel method.* J. Sol-Gel Sci. Technol., 2009. **52**(1): p. 153-157.

15.   Thayer, R.*, et al.*, *Medium permittivity bismuth zinc niobate thin film capacitors.* J. Appl. Phys. , 2003. **94**(3): p. 1941-1947.

16.   Nino, J.C.*, et al.*, *Phase formation and reactions in the Bi$_2$O$_3$-ZnO-Nb$_2$O$_5$-Ag pyrochlore system.* J. Mater. Res. , 2001. **16**(5): p. 1460-1464.

STATEMENT OF CONTRIBUTION OF CO-AUTHORS

The authors listed below have certified that:

1. They meet the criteria for authorship in that they have participated in the conception, execution, or interpretation, of at least that part of the publication in their field of expertise;
2. They take public responsibility for their part of the publication, except for the responsible author who accepts overall responsibility for the publication;
3. There are no other authors of the publication according to these criteria;
4. Potential conflicts of interest have been disclosed to (a) granting bodies, (b) the editor or publisher of journals or other publications, and (c) the head of the responsible academic unit; and
5. They agree to the use of the publication in the student's thesis and its publication on the QUT e-Prints database consistent with any limitations set by publisher requirements.

In the case of this paper:

Electronic Structure Studies and Photocatalytic Properties of $Bi_{1.5}ZnNb_{1.5}O_7$

Contributor	Statement of contribution
Ganchimeg Perenlei (PhD candidate)	Conducted all computational and experimental data collection and analysis, and manuscript writing.
Wayde N. Martens (Principal supervisor)	Assisted with experimental analysis and manuscript development.
Peter C. Talbot (Associate supervisor)	Assisted with computational analysis and manuscript development.
Jose A. Alarco (Associate supervisor)	Assisted with computational analysis and manuscript development.

Principal Supervisor Confirmation

I have sighted e-mail or other correspondence from all Co-authors confirming and certifying authorship.

Wayde Martens   4/11/15
_____
Name   Signature   Date

3.3 ARTICLE 2: "ELECTRONIC STRUCTURE STUDIES AND PHOTOCATALYTIC PROPERTIES OF $Bi_{1.5}ZnNb_{1.5}O_7$"

Ganchimeg Perenlei,[1] Jose A. Alarco,[1,2] Peter C. Talbot[1,2] and Wayde N. Martens[1]

[1]*School of Chemical, Physics and Mechanical Engineering, Science and Engineering Faculty,* [2]*Institute for Future Environments, Queensland University of Technology, Brisbane, QLD 4000, Australia*

ABSTRACT

The photocatalytic ability of cubic $Bi_{1.5}ZnNb_{1.5}O_7$ (BZN) pyrochlore for the decolorization of an acid orange 7 (AO7) azo dye in aqueous solution under ultraviolet (UV) irradiation has been investigated for the first time. BZN catalyst powders prepared using low temperature sol-gel and higher temperature solid-state methods have been evaluated and their reaction rates have been compared. The experimental band gap energy has been estimated from the optical absorption edge and has been used as reference for theoretical calculations. The electronic band structure of BZN has been investigated using first-principles density functional theory (DFT) calculations for random, completely and partially ordered solid solutions of Zn cations in both the *A* and *B* sites of the pyrochlore structure. The nature of the orbitals in the valence band (VB) and the conduction band (CB) has been identified and the theoretical band gap energy has been discussed in terms of the DFT model approximations.

INTRODUCTION

The textile industry is one of the biggest consumers of synthetic dyes which comprise a large number of chemicals, mostly organic compounds [1]. Synthetic dyes can be classified into several groups based on their chromophoric groups in the structure. Azo-dyes, commonly used as colourants, consist of one or more azo (-N=N-) bonds coupling with several aromatic groups in the structure and account for 60 - 70 % of all dyestuffs in the textile industry [2]. High concentration of dye residues in textile effluents has become a major source of water pollution. Treatment of dye wastewater is challenging, because it contains not only dyestuffs residues, but also various additives such as acidic and alkaline contaminants, pigments, heavy metals and other organic pollutants [3]. Related research has recently focused on removing dyes from dye-containing effluents or decolorizing them through liquid fermentation [4].

Wastewater treatment through heterogeneous photocatalysis using semiconductor materials has received enormous attention as a cutting edge, energy efficient technology since the last decade. The main reason is that photocatalysis by itself, or in combination with other water treatment technologies, can provide simultaneous decomposition of a wide range of pollutants at a low energy cost [5]. A variety of semiconductor materials with increasing degree of complexity in composition have been investigated for the photocatalytic degradation of organic pollutants in aqueous media. Bi-based multi-metal oxides, such as $BiMO_4$ (M=V, Nb, Ta) [6-8], Bi_2MO_6 (M=Mo, W) [9, 10], BiOX (X=Cl, Br, I) [11] and $Bi_2Ti_2O_7$ [12], have been considered as promising catalysts.

Photocatalysts containing mixed atoms or solid solutions in the crystal structure have also shown significant improvements in photocatalytic activity as compared with that of their simpler oxide end members; for example, $BiNb_xTa_{1-x}O_4$ and $Bi_2Mo_xW_{1-x}O_6$ photocatalysts ($0 \leq x \leq 1$) have performed better than $BiNbO_4/BiTaO_4$ [13] and Bi_2MoO_6/Bi_2WoO_6 [14], respectively. Another pyrochlore type of materials with mixed atoms, such as Bi_2MNbO_7 (M=Al, Ga, In, Fe) [15, 16] and Bi_2MTaO_7 (M=Al, Ga, In, Fe) [17, 18], have also been studied for photocatalytic removal of organic dye pollutants from water. These compounds have an ideal pyrochlore structure with $A_2B_2O_7$ general composition and generally exhibit diverse physical properties, which are useful for a wide range of applications [19, 20]. These examples contain *p*-block M^{3+} metals (except for Fe) along with NbO_4 or TaO_4 networks. Many of the aforementioned investigations have been experimentally driven and have not been matched with a corresponding level of complexity in electronic band structure calculations.

Recently, another set of Bi_2O_3-based complex pyrochlore compounds containing M^{2+} metals, such as, $Bi_{1.5}ZnTa_{1.5}O_7$ [21], $Bi_{1.5}ZnSb_{1.5}O_7$ [22] and $Bi_{1.5}MNb_{1.5}O_7$ (M=Zn, Cu, Ni, Mn, Mg) [23, 24], have received enormous attention for various non-photocatalytic applications. Cubic $Bi_{1.5}ZnNb_{1.5}O_7$ (BZN) with space group symmetry of *Fd-3m* (number 227) is one of these ideal pyrochlore structures that may enable a wider range of metal substitutions targeted to specific properties of interest [25-30]. The crystal structure of cubic BZN is one of the most widely investigated throughout the literature using X-ray and neutron diffraction techniques [31-33], therefore, it can be considered as a good reference for additional research investigations. The BZN structure can be described in general as *$A_2O' \cdot B_2O_6$* and specifically as $(Bi_{1.5}Zn_{0.5})(Nb_{1.5}Zn_{0.5})O_7$ [34]. The *A* site mainly contains Bi cations, while the *B* site

contains Nb cations. It is believed that Zn cations are equally divided between the two sites, with up to 25 % of the Bi and Nb cations each being randomly substituted by Zn, respectively [32, 35], however, there are some controversies about the percentage of Zn occupancy in the *A* site. Both experimental and theoretical studies have focused on finding the optimal *A*/*B* combinations for particular applications [32, 33]. Nevertheless, the need for a clearer correlation between the crystallographic structure and DFT calculated electronic band structures for this type of compounds is extant.

In this work, the photocatalytic ability of the cubic BZN compound has been investigated for the degradation of an azo-dye solution for the first time. To further understand the photocatalytic properties of the material, the optical properties have been characterized by light absorption edge measurements and the effect of Zn 3*d*-orbitals on the electronic band structure has been systematically investigated by DFT calculations. Particular focus has been paid on the assumptions concerning the substitutions and the effects of these on the size and nature of the band gaps.

EXPERIMENTAL SECTION

Material Preparation

A commercial dye, acid orange 7 (AO7), has been selected as a representative of organic azo-dye pollutants and has been purchased from Aldrich (Australia). An aqueous solution of AO7 with concentration of 20 mg L^{-1} has been prepared for the photocatalytic dye decolorization reactions. The BZN compounds used as the catalyst in the experiments have been prepared by two different methods, a conventional solid-state reaction and a sol-gel technique. The synthesis of the cubic BZN powders at various temperatures by the sol-gel method has been described in detail in a previous report [36]. In the case of the solid-state method, the BZN powders have been prepared from high purity (99.9 %) bismuth oxide (Bi_2O_3), niobium oxide (Nb_2O_5) and zinc oxide (ZnO), which have also been purchased from Aldrich (Australia). The solid-state synthesis includes repeated mixing and heating processes, and the final product has been obtained at 1000 °C after heating for 5 h in air.

Material Characterization

The crystal structures of the BZN powders have been analyzed by X-ray diffraction (XRD) using a Philips PANalytical X'Pert PRO X-Ray Diffractometer for phase identification. Surface morphologies of the compounds have been analysed using a JEOL 7100F scanning electron microscope (SEM) coupled with energy-dispersive X-ray spectroscopy (EDS). The samples have coated with gold particles before the analysis to avoid charging at 20 kV. Specific surface areas of the powders have been

measured by N_2 adsorption/desorption isotherms by the Brunauer-Emmett-Teller (BET) method using a Micromeritics TriStar II 3020.

Optical analysis has been carried out to estimate the experimental band gaps of the BZN materials from absorption edges of UV-Vis diffuse reflectance spectra using a UV-Vis-NIR Cary 5000 Stheno spectrometer. The spectra have been recorded in the region of 200 - 800 nm wavelengths. These measurements have been complemented by mid-infrared (mid-IR) spectroscopy using the Perkin-Elmer 1600 series Fourier transform infrared spectroscopy (FTIR). The IR spectra have been recorded in the region of 650 - 4000 cm^{-1} wavenumber.

Photocatalysis

The photocatalytic ability of the BZN materials has been evaluated by the decolorization of an AO7 solution under UV irradiation. The AO7 degradation process has been monitored by recording its maximum absorption peak (λ_{max}) at a wavelength of *ca.* 485 nm, in the visible light region. The light source used in this experiment is a 15 W NEC blacklight FL15BL (*ca.* 365 nm wavelength). The photocatalytic reaction has been performed by adding 0.1 g of BZN powders into 10 mL of AO7 solution in a 30 ml glass vessel, which is then irradiated with UV light. The suspension has been stirred in the dark for 10 min using a magnetic stirrer, before switching on the UV light to start the reaction. After each experiment, the concentration of the dye solution has been determined by measuring its light absorption using a UV-Vis Cary 50 spectrometer.

THEORETICAL CALCULATIONS

Electronic Structure Calculations

The energy band structure and density of states (DOS) of BZN have been calculated using Density Functional Theory (DFT), as implemented in the Cambridge Serial Total Energy Package (CASTEP) of Materials Studio 8.0. All structures have been geometry optimized first. Various calculation setups have been investigated using functionals for the Local Density Approximation (LDA) or the Generalized Gradient Approximation (GGA), cut-off energy values from 300 to 1000 eV, k-grids from 0.03 to 0.07 A^{-1}, and metal and non-metal choices. A range of convergence tolerances including ultrafine and fine setups, and various assumptions on spin polarization in the calculations have also been investigated, particularly when the standard setup has resulted in difficulty achieving convergence and when the converged results have indicated that no band gap is present. However, in most typical calculations, the GGA with Perdew-Burke-Ernzerhof (PBE) functional with norm-conserving pseudopotentials has been adopted along with k-grid of 0.03 A^{-1} giving a 6×6×6 k-point mesh, plane wave basis set cut-off of 830 eV, 100 empty orbitals, non-metal, non-spin and ultra-fine convergence tolerance setups.

Bi$_{1.5}$ZnNb$_{1.5}$O$_7$ Structure

The crystal structures of BZN used in DFT calculations have been taken and/or adapted from *Crystallographic Information File* (CIF) from the Inorganic Crystal Structure Database (ICSD). The starting cubic BZN structure (JCPDS PDF, 04-016-3002) has lattice parameter *a*=10.5615 (Å) and contains fractionally occupied cations at the Bi (*A*) and Nb (*B*) sites with ratios of Bi/Zn=78.125:21.875 and Nb/Zn=75:25, respectively [32]. With fractional occupancy, the structure represents a random solid solution as illustrated in Figure 3-7(a). Atoms are displayed using a ball and stick style and rules for color mixing are used to represent sites with fractional occupancy. Mixed cations of Bi/Zn and Nb/Zn are therefore orange (yellow+red) and purple (blue+red) balls, respectively, and pure O anions are green balls.
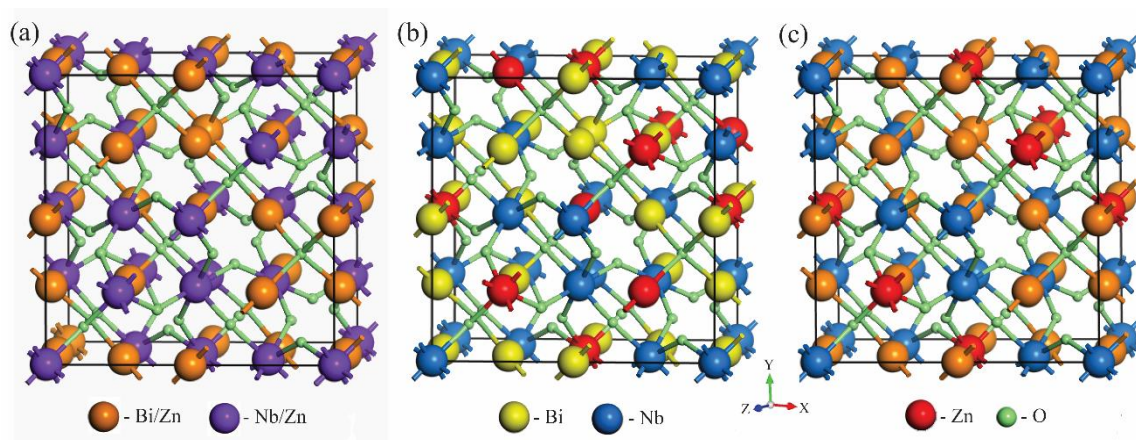
Figure 3-7: BZN structures assuming: (a) random, (b) ordered and (c) partially ordered solid solutions. Bi, Nb, Zn and O atoms are yellow, blue, red and green balls, respectively. Rules for color mixing are used to represent sites with fractional occupancy, therefore, Bi/Zn and Nb/Zn sites become orange (yellow+red) and purple (blue+red), respectively.

Another approach for Zn cation substitution at specific sites of the BZN structure has also been investigated by DFT calculations. In this case, the fractional occupancy is removed and a quarter (25 %) of Bi and a quarter (25 %) of Nb cations at specific sites are replaced by Zn cations. This approach incorporates new periodicities for the Zn substitutions and can be considered as an ordered solid solution. It is an approach that has previously been used in the literature to investigate the stability of potential specific substitutions by looking at the enthalpy [34, 37]; however, no report has been made of the effects of these site substitution choices on the electronic band structure and/or the band gaps. There is a large variety of possible choices for substituted Zn cations. The four main different substitution arrangements discussed in the above mentioned stability study [37] have been investigated in our work. An example structure, which has shown the most representative and consistent results with experiments, is displayed in Figure 3-7(b). Pure Bi and pure Nb are now yellow and blue, respectively, while substituted Zn atoms are red balls.

BZN structures containing a combination of both random and ordered Zn cations substitutions have also been investigated using DFT calculations and are referred to as partially ordered solid solutions. In these cases, the Zn substitution at either the *A* or the *B* sites is randomly substituted while the other is ordered or vice versa. Figure 3-7(c) shows the partially ordered BZN structure, where Zn cation substitutions are random at the *A* site, whereas ordered at the *B* site, respectively. As described above mixed cations of Bi/Zn are orange, pure Nb cations are blue, pure O anions are green and substituted Zn cations at the *B* site are red balls, respectively.

RESULTS AND DISCUSSION

Phase Identification

The XRD patterns of the BZN powders synthesized at 550 and 1000 °C by the sol-gel and the solid-state techniques, respectively, are shown in Figure 3-8. The main crystal peaks in the patterns are indexed to $Bi_{1.5}ZnNb_{1.5}O_7$ (JCPDS PDF, 04-016-3002) in the ICSD database, which indicates that the cubic BZN compounds are obtained at both sintering temperatures. The reduced crystal peak widths for materials prepared with increased sintering temperature confirm an increasing degree of crystallinity as determined using the Scherrer equation.
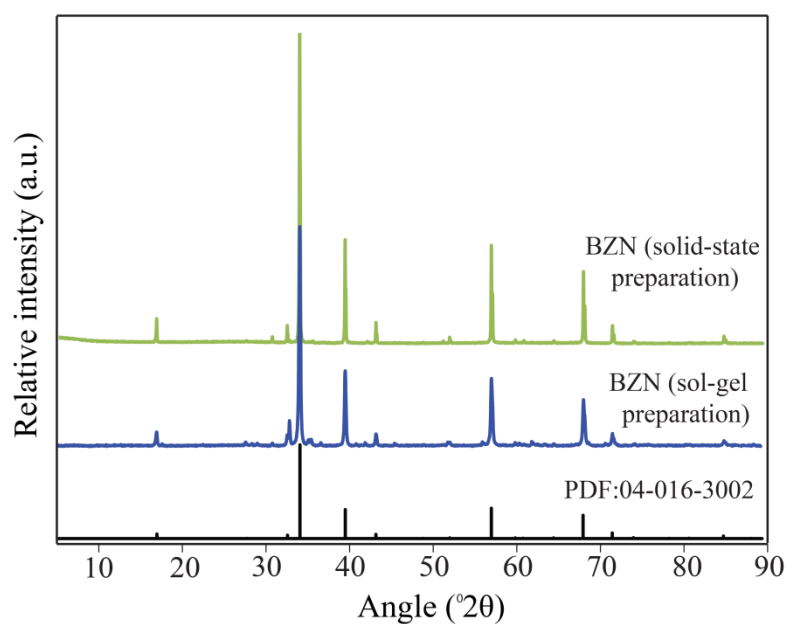
Figure 3-8: XRD patterns of the BZN powders prepared at 550 °C by the sol-gel and at 1000 °C by the solid stated methods (the bottom pattern is the PDF card number for the cubic BZN)

Surface Morphology

The SEM micrographs of the BZN powders prepared at 550 and 1000 °C by the sol-gel and solid-state reaction methods, respectively, are shown in Figure 3-9. The surface morphology of the powders suggests that the low temperature sol-gel method provides relatively fine and uniform microstructure with grain size of about 0.5 μm as seen in Figure 3-9(a).
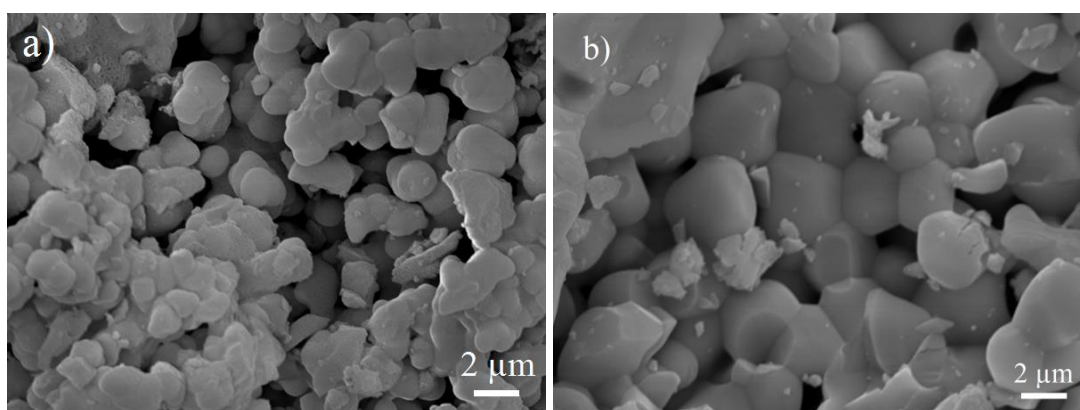
Figure 3-9: Surface morphology of the BZN prepared at (a) 550 °C by the sol-gel and (b) 1000 °C by the solid state methods

Conversely, the SEM microstructure in Figure 3-9(b) shows less homogeneous particles with grain sizes varying from about 1 μm and above. A small amount of Bi-rich particles by EDS analysis are also observed on the grain boundaries of materials prepared by the solid-state method. This is likely an indication of formation of the residual impurities or of incomplete homogeneity achieved by mechanical mixing of the different metal oxides. Measured BET surface areas have been consistent with the grain size determinations.

Optical Absorption Analysis

The optical absorption curves of the BZN powders prepared by the two different methods are displayed in Figure 4. Although the grain sizes vary with the processing temperature, their optical band gaps appear very similar. The band gap values estimated from the UV-Vis spectra are about 2.75 and 2.90 eV at 550 and 1000°C, respectively.
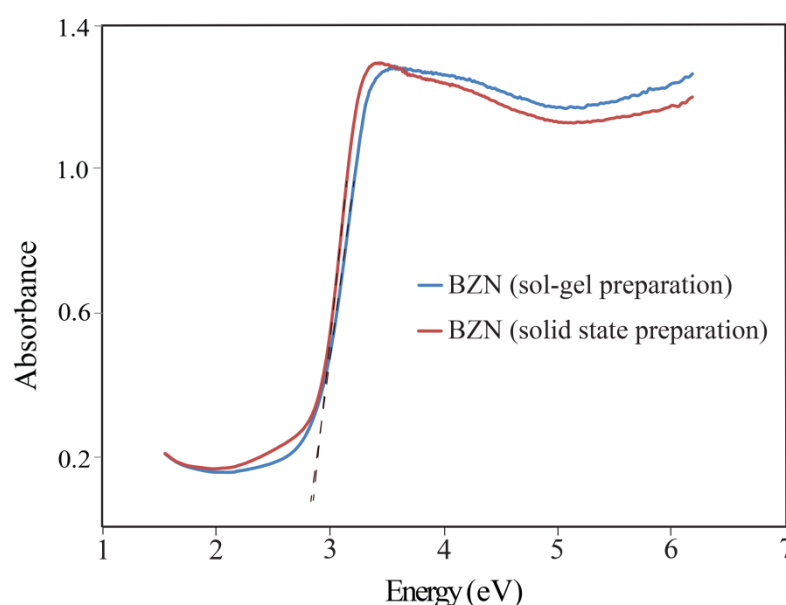
Figure 3-10: Absorption edge of the BZN powders prepared at 550 °C by the sol-gel and 1000 °C by the solid state methods

The optical measurement of the BZN powders has also been extended to higher wavelength regions using mid-IR spectroscopy to examine for possible lower energy absorption features. A possible small absorption edge could be seen at 900 - 1300 cm^{-1} (0.11 - 0.16 eV), however, it is not very conclusive whether this is the result of electronic transitions within levels in the band structure or not. The experimental band gap values suggest that the BZN powders may have an ability to utilize energy

wavelengths of *ca.* 430 nm and below, that is, that the compound might be responsive to UV irradiation.

Photocatalytic Dye Decolorization

The changes in the concentration of the AO7 dye solution under UV irradiation for 120 min in the presence and absence of catalysts are shown in Figure 3-11. It is apparent from the time-dependent graphs of the dye degradation that no clear sign of dye degradation has been observed in the absence of any catalyst under UV irradiation. However, a slight decrease of concentration of the dye solution (3 - 4 %) has been observed after 120 min of experiment duration. This decrease is due to the slow photolysis of this catalyst under these conditions and represents a baseline for no catalyst.

In the presence of the BZN powders, the degradation of the dye solution is noticeably increased under UV irradiation; however, the photocatalytic activity of the BZN samples varies depending on the catalyst preparation methods. When the BZN catalyst prepared by the solid-state method at 1000 °C is used in the reaction, the observed decolorization of the dye solution is considerably lower than that of the sol-gel BZN catalyst. Only about 18 % of the dye solution has been degraded in the 120 min of experiment duration. This might be due to the larger particle size/smaller surface area of the powders synthesized at relative high temperature or the presence of phase impurities in the material interfering with the performance. Although, this method is less recommended for the preparation of homogeneous catalyst materials, it is still informative to examine it for comparison, as this is the most commonly employed synthetic method for the preparation of cubic BZN in the literature.
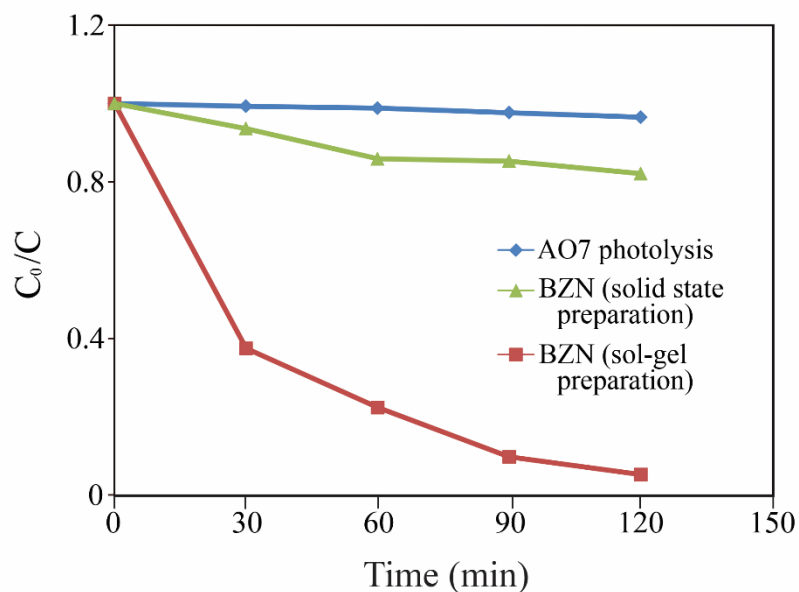
Figure 3-11: The changes in concentration of the AO7 dye solution under UV

irradiation with and without the BZN catalysts

On the other hand, the low temperature (550 °C) BZN catalyst prepared by the sol-gel method has shown significant activity for the photodegradation of the dye solution under UV irradiation. In fact, more than 50 % of the dye concentration has been reduced within the first 30 min, further decolorization of approximately 95 - 96 % of the dye has been reached within 120 min and, shortly after, complete removal is achieved. This result indicates that the BZN compound is photoactive under UV light with wavelength of *ca.* 365 nm. Therefore, the faster photocatalytic degradation of the azo-dye in aqueous media is achieved with assistance of the BZN catalyst photoexcited by UV irradiation.

Figure 3-12 shows the kinetics of the photocatalytic decolorization of the AO7 dye solution in the presence of the BZN catalysts on a logarithmic scale. The plots of dye concentration versus experimental duration show that the reaction rates can be described by a pseudo-first order kinetic model with formula, *ln(C$_0$/C)=kt*, where *C$_0$* is the initial concentration and *C* is the concentration at time, *t*. The photocatalytic dye degradation rate using the BZN powders prepared by the solid state method has shown considerably slower kinetics than that obtained using the BZN powders prepared by the sol-gel method. The calculated apparent rate constants are 0.024 and 0.002 min^{-1} for the powders prepared at 550 °C by the sol-gel and at 1000 °C by the solid state methods, respectively. These different reaction rates suggest that the reaction rate is determined by a corresponding different number of active sites on the surface of the BZN powders for the different particle sizes and surface areas.
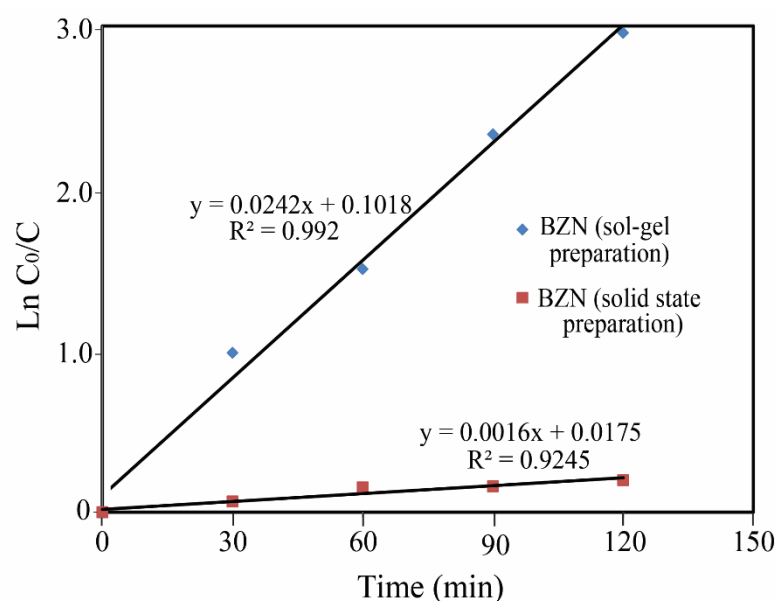
Figure 3-12: Reaction kinetics for the BZN catalysts prepared by different synthetic methods

Additional experiments on the dye decolorization reaction have been carried out using the BZN catalyst synthesized at different temperatures to further examine the influence of processing temperature on the surface area and consequently the reaction rate. Catalyst powders prepared by the sol-gel method have been heated in air at various temperatures in the range 500 - 900 °C for 5 h, for this comparison. A new set of photocatalytic reactions, using the same initial concentration of dye solution and amount of catalyst, have been run under UV irradiation for 60 min with these powders. The surface areas of the BZN powders and the percentage of decomposed AO7 dye concentration detected at $\lambda_{max} = 485$ nm after 1 h through the catalytic reaction are listed in Table 3-1. It can be clearly seen from the table that the photocatalytic activity of the BZN powders is highest at the lowest sintering temperature of 500 °C, and that it constantly declines with increasing temperature.

Table 3-1: Surface area and dye decomposition dependence on the heating temperature of the BZN catalyst (as percentage), after 1 h of photocatalytic reaction

Temperature (°C)	Grain size (µm)	Surface area ($m^2\ g^{-1}$)	Dye decomposition percentage (%)
500	less than 0.5	25.28	79.30
550	about 0.5	14.41	77.67
600	0.7 - 0.8	11.89	66.97
700	less than 1	2.29	34.51
800	about 1	0.36	20.22
900	above 1	0.34	14.15
1000	1 - 3	0.30	14.00

This result is similar to a previous report in the literature, where Bi_2FeNbO_7 catalysts prepared at the lowest temperature of 400 °C by sol-gel have shown much better performance than the higher temperature catalysts for methylene blue dye degradation [15]. Note that the surface area and the degraded concentrations of the dye using the BZN powders prepared at 1000 °C by the solid state method show similar results to those obtained for the sol-gel prepared BZN powders heated to 800 and 900 °C.

Some other parameters that might affect the overall dye degradation reaction such as concentration of catalyst, initial concentration of dye solution and usage of different lamp have also been briefly studied. It has been found that the photocatalytic reaction rate is influenced by both the catalyst dosage and the initial concentration of the dye solution. However, increasing the catalyst amount to speed up the dye removal process reaches a point where an excess amount of catalyst in the solution begins to block the efficient absorption of photons.

Moreover, the stability of the BZN catalysts has been examined by their repeated usage in photocatalytic dye degradation reactions under the same experimental conditions. For such tests, the BZN powders from an initial experiment have been centrifuged, cleaned and dried before re-applying them in subsequent experiments. It has been determined that the BZN catalyst can be reused at least 3 times repeatedly for the photocatalytic reaction without changing its performance. The XRD patterns of the catalyst have also been collected after the reactions and found to be unchanged. Experiments in the dark have also shown that there is no change in the dye concentration, which is an indication of limited or no surface absorption onto the BZN catalyst.

Electronic Structure Calculation

As mentioned earlier, the electronic band structures and the DOSs for random, ordered and partially ordered solid solutions have been investigated using DFT calculations. Among the ordered solid solutions, various combinations have been studied, but the specific arrangement shown in Figure 4-1(b) has been selected as providing the most representative results.

BZN random solid solution

All attempts to calculate the electronic band structure of the BZN with fractional occupancy and no spin have resulted in metallic-like materials without band gaps near or from the Fermi level. These results have been consistent for all different settings (k-grid, cut-off energy, etc.) used in the calculations when the calculation is spin unpolarized for both cubic and primitive BZN structures. Since this has not reflected the experimentally observed optical results, spin polarized calculations have also been explored in the DFT studies. Figure 3-13 shows the energy band diagram and DOS obtained for the random solid solution of the cubic structure assuming spin is equal 2 and using ultrafine convergence criteria (energy = 5.0×10^{-6} eV atoms^{-1}, force = 0.01 eV Å^{-1}, stress = 0.02 GPa and displacement = 5.0×10^{-4} Å) with cut-off energy of 830 eV.
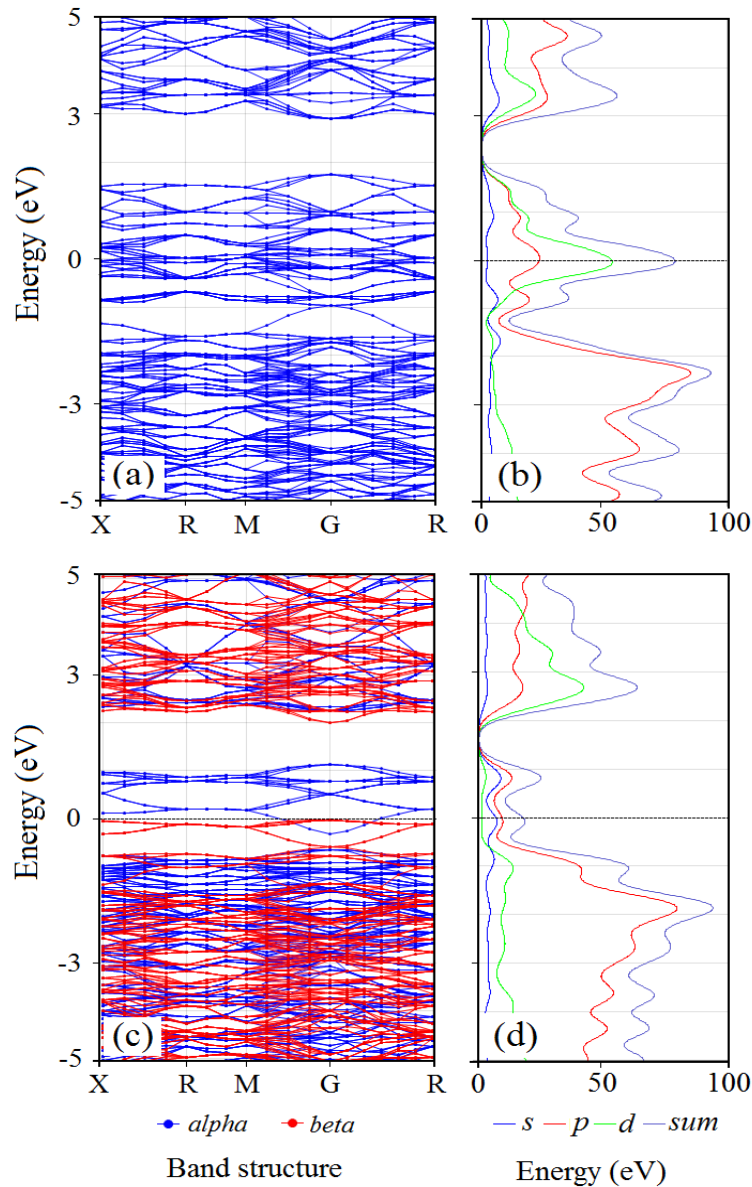
Figure 3-13: The band structures and DOSs for the cubic BZN random solid solution structure for (a and b) spin unpolarized and (c and d) spin polarized calculations

A band gap clearly develops slightly (~ 1 eV) above the Fermi level (defined at 0 eV), however, the states in the vicinity of the Fermi level appear to be localized impurity bands, above dense states in the VB (~ -1 eV), while a dense CB begins at about 2 eV, as can be seen in Figure 3-13(a). Direct band gaps of about 2.7 and 2.9 eV between the dense VB and CB regions have been estimated for the alpha and beta spins, respectively, at the G point in reciprocal space. The nature of the localized

bands as impurity bands seems further confirmed by the fact that the calculation assigns the Fermi energy at -0.95 eV to the result, indicating that the middle point between a fully occupied continuous VB and the top of the localized impurity bands has been taken as the Fermi level. This suggests that some optical absorption may be seen between the continuous VB bands and the impurity bands, but that the main optical absorption edge will take place between the continuous VB and the continuous excited CB which is separated by about 2.7 - 2.9 eV.

The DOS curves for BZN random solid solutions are shown in Figure 3-13(b and d). A relatively dense band around the Fermi level in the electronic band structure with unpolarised spins, which consists mainly of *d* and *p* states in Figure 3-13(b), becomes significantly less dense when spin polarization is applied in the calculations. Here, the presence of impurity bands observed in the electronic band structure in Figure 3-13(d) is nevertheless due to the presence of Zn cations in the structure, indirectly if not directly.

BZN ordered solid solution

Since the random solid solution has not given very good match to optical absorption results, apart from some spin polarized cases, the substitution of Zn cations at specific positions in the *A* and *B* sites of the BZN structure has also been investigated by DFT calculations with and without spin polarization. Similar to the studies of random solid solutions, calculations for ordered solid solution have also compared (or attempted to) primitive and symmetry options. For the spin polarized case, only primitive structures choices have resulted in completed calculations.

Calculations that have attempted to retain the structural symmetry have led to convergence difficulties, presumably due to the large number of atoms and complexity of the structure. The primitive choice typically ends up into a triclinic structure, while the symmetry choice forms an orthorhombic structure after their respective geometry optimizations. To achieve convergence, criteria have been customized to less demanding values than the usual default values (also, than those which have been used for random solid solutions). Final convergence has been generally obtained with customized tolerance setups using combinations for energy = 5.0×10^{-5} eV atoms^{-1}, force = 0.03 eV Å^{-1}, stress = 0.02 GPa and displacement = 5.0×10^{-3} Å, respectively, with k-grid of 0.07 A^{-1}, which gives a k-point mesh of $2 \times 2 \times 2$ and cut-off energy of 750 eV.

Figure 3-14 shows the energy band diagram and DOS contributed by all the different atoms in the modified BZN ordered solid solution with C-centered orthorhombic structure. Note that there are also localized states between dense regions of VB and CB states. The energy band diagram shown in Figure 3-14(a) is the most representative result of the ordered solid solutions investigated with a spin unpolarized choice. The energy band structure of BZN ordered solid solution with a spin-polarized choice is nearly identical to that of the spin unpolarized cases. It is also the most consistent with the experimental gap and the results obtained for the spin polarized choices for the BZN random solid solution, if we assume that the optical absorption is mainly due to transitions between the dense groups of states with a separation of about 2.25 eV at the G point in reciprocal space.
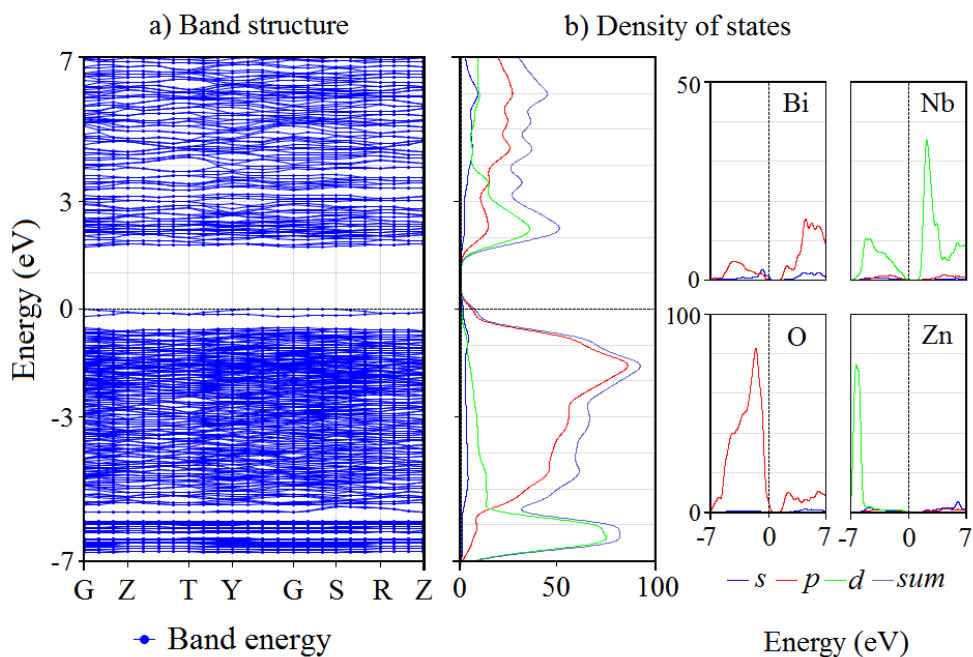
Figure 3-14: The band structure and DOS for the C-centered orthorhombic

BZN ordered solid solution

Figure 3-14(b) displays the total and partial DOS for the selected BZN ordered solid

solution. The VB mainly consists of O $2p$ states, whereas the CB consists mainly of

Nb $4d$, O $2p$ and Bi $6p$ states. A small amount of Bi $6s$ states are also found on the

top of O $2p$ VB states, which helps raise the level of VB slightly. With respect to the

contribution of Zn to the electronic band structure, a pronounced peak of $3d$ states is

obtained between -5.5 and -7.0 eV. This energy level is several eVs below the Fermi

level and it may therefore only contribute indirectly to the determination of the size

of the band gap.

BZN partially ordered solid solution

The partially ordered solid solution produced optimized results combining some of the desirable features of the separate random and ordered solid solution results, such as less distortion with retention of the orthorhombic and cubic structure after geometry optimization, ability to use more demanding convergence criteria and presence of an electronic band gap, all of these simultaneously. Convergence has been reached using fine convergence criteria (energy = 1.0×10^{-5} eV atoms^{-1}, force = 0.03 eV Å^{-1}, stress = 0.05 GPa and displacement = 1.0×10^{-3} Å), respectively, with k-grid of 0.03 A^{-1}, which gives a k-point mesh of $4 \times 4 \times 4$ and cut-off energy of 750 eV.

Figure 3-15 illustrates the energy band diagram and total and partial DOS for the BZN partially ordered solid solution, where the *A* site is random, while the *B* site is ordered. A band gap of about 2.2 eV (between dense groups of states) has been obtained at the G point in reciprocal space for the orthorhombic BZN structure, which is the same as the band gap obtained from the ordered BZN solid solution calculations, however, the localized levels have been shifted to slightly higher energy inside this gap. This result is still lower than the experimentally estimated band gap values of about 2.7 - 2.8 eV. A similar difference between calculated and experimental values, has been determined for pure $BiNbO_4$, where the calculated band gap is about 2.3 eV for the orthorhombic structure, whereas the estimated experimental band gap for powders prepared by the sol-gel method is about 2.7 eV.
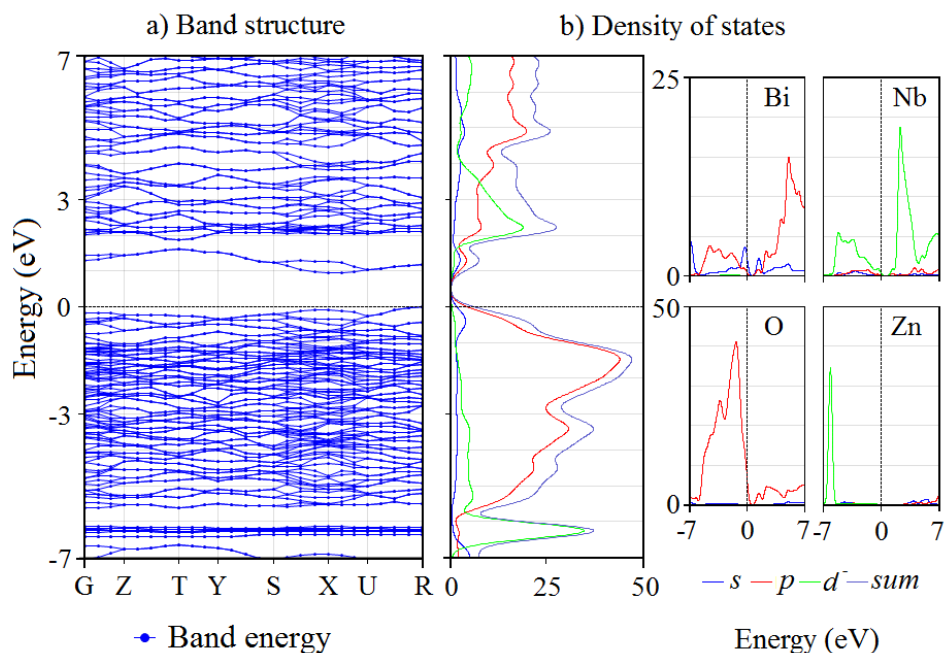
Figure 3-15: The band structure and DOS for the orthorhombic BZN partially

ordered solid solution

The localized impurity bands seem to arise from Zn *s* orbitals in the mixed Bi/Zn cations positions of the random solid solution. Such impurity bands may act as traps for photogenerated electrons during the photocatalytic reaction. The energy band structure of BZN partially ordered solid solution with a spin polarized choice is nearly identical to that of the spin unpolarized cases.

Conversely, while retaining the cubic structure, when the Zn substitutions on the *A* and the *B* sites are ordered and random, respectively, no band gap appears which is similar to the calculated results from the random solid solution structure (unpolarized case). Nb *d* orbitals are driven downwards in energy by the involvement of Zn cations in the *B* site of the BZN structure as Nb/Zn mixed cations. This energy downshift of Nb *d* orbitals diminishes when spin polarization is introduced in the DFT calculations.

Summary of calculated results

Table 3-2 summarizes the DFT calculation results for BZN random, completely and partially ordered solid solutions. The obtained final enthalpy of formation of -58427.17 eV for the ordered BZN solid solution is generally lower than the enthalpy of formations of -56362.37 eV for the random solid solution. Such a result is often taken as an indication of favourable formation; however, the final structure obtained is slightly distorted from the initial (experimental) cubic structure, as can be seen in Table 3-2.

Geometry optimization of the BZN random solid solution produces a contraction of the lattice parameters (a=10.48 Å), while the opposite takes place for the ordered solid solution (a=10.86 Å) as compared to the initial cubic structure (a=10.56 Å), when the GGA function is in use. In the case for the LDA function in the calculations, slight decreases in the lattice parameters and the band gap values are observed for all structures. While the random solid solution maintains the cubic structure after geometry optimization, all ordered solid solutions produce small distortions of the initial structure often to orthorhombic structure. The partially ordered solid solution where the Zn substitution in the *A* and *B* sites are ordered and random, respectively, gives a cubic final structure after the geometry optimization, however, it does not show a band gap, indicating that order of the Zn substitutions in the Nb sites is key to the observation of a gap.

Table 3-2: Comparison of parameters obtained with DFT-GGA calculations for

BZN random, ordered and partially ordered solid solutions

BZN solid solution[a]	Calculated symmetry	Spin pola-rization	Lattice length (Å)	Lattice angles (°)	CASTEP formation energy (eV)	CASTEP normalized energy (kJ/mol)	Band gap (eV)
Random	Cubic	No spin	10.48	90	-56362.37	-156.56	no gap
	Cubic	Spin=2	10.44	90	-56371.45	-156.58	2.7; 2.9
	Primitive[b]	No spin	7.41	60	-14090.59	-156.56	no gap
	Primitive	Spin=2	7.41	60	-14096.12	-156.62	2.9
Ordered	C-centered[c] orthorhombic	No spin	10.86 10.86 10.71	90 90 89.49	-58427.17	-162.29	2.2
	Triclinic	No spin	10.87 10.74 10.85	90.03 90.79 89.93	-58427.27	-162.29	2.2
	Triclinic	Spin=2	10.87 10.74 10.84	89.99 90.82 90.00	-58427.31	-162.29	2.2
Partially ordered (*B* site)	Ortho-rhombic	No spin	7.614 7.52 10.82	90	-29253.78	-162.52	2.2
	Ortho-rhombic	Spin=2	7.614 7.52 10.76	90	-29253.79	-162.52	2.2
Partially ordered (*A* site)[d]	Cubic	No spin	10.58	90	-56278.65	-156.32	no gap

[a]The input structure is adapted from the cubic BZN cif (*a*=10.56 Å);

[b]The input structure converted to primitive has lattice parameter 7.46 Å with 60° angles;

[c]The CASTEP program labels the result structure as C-centered orthorhombic even though there is a small deviation from 90° in one of the angles;

[d] Spin polarization in this case resulted in job failure during calculations.

For random solid solutions, only spin polarized calculations have resulted in a band gap, while all the other choices display no band gaps. For the selected BZN ordered solid solutions, only the primitive structure has given completed calculations for polarized spin. For non-spin polarized calculations, both symmetry and primitive structures produce band gaps and band structures with very small difference.

The absence of a band gap in the electronic structure of BZN random solid solutions, while some gaps can be encountered when ordered and partially ordered solid solutions in the *B*-site are investigated, strongly suggests that the real BZN structure is not randomly substituted. The assumption of a random solid solution may be effective in structural determinations through the use of thermal ellipsoid factors, which average the exact atomic positions in the structure. However, DFT calculations indicate that to observe a band gap additional periodicities, not present in the random solid solution, may be required. Spin polarization may be introducing some additional periodicity in the random solid solution. Ordered and partially ordered solid solutions do introduce new periodicities and they could be present as domains with various orientations, so as to produce an overall cubic like diffraction pattern. Therefore, the electronic band structures when some ordered solid solution is considered are, in general, more consistent with the optical absorption results. This observation includes the possible presence of impurity bands, which may also account for some of the optical and photocatalytic effects.

CONCLUSIONS

The photocatalytic properties of cubic BZN have been investigated for the first time. The BZN has been found to be UV light responsive, however, the photocatalytic activity of BZN is inferior to that of pure $BiNbO_4$. Although the assumption of a random solid solution of Zn may give a reasonable explanation for the X-ray and neutron diffraction properties of cubic BZN structure, DFT calculations indicate that to obtain band gaps in the electronic band structure, some degree of partial order in the substitution is required. This order results in band gaps that are more consistent with experimental optical absorption results and may be favoured by enthalpy of formation arguments. Calculations also indicate the presence of impurity bands, which may be responsible for a small absorption edge in the mid-IR and for enhanced recombination and trapping of photogenerated electron - hole pairs compared to pure $BiNbO_4$. Although the results indicate that substituted Zn does not produce enhancement of the photocatalytic properties, a methodology has been established which can be systematically used for the investigation of additional $3d$-transition metal substitutions.

REFERENCES

1. Gurr, E., *Synthetic dyes in biology, medicine and chemistry*. 2012: Elsevier.

2. Vieira, H., N. Martins, and F.F. Vale, *AQUACHIP-A DNA Chip for the detection of several microorganisms in water samples–Design and preliminary results.* Book of Abstracts of MicroBiotec09: p. 177.

3. Wang, Z., et al., *Textile dyeing wastewater treatment.* 2011: INTECH Open Access Publisher.

4. Banat, I.M., et al., *Microbial decolorization of textile-dyecontaining effluents: a review.* Bioresource technology, 1996. **58**(3): p. 217-227.

5. Gaya, U.I. and A.H. Abdullah, *Heterogeneous photocatalytic degradation of organic contaminants over titanium dioxide: a review of fundamentals, progress and problems.* Journal of Photochemistry and Photobiology C: Photochemistry Reviews, 2008. **9**(1): p. 1-12.

6. Dunkle, S.S. and K.S. Suslick, *Photodegradation of BiNbO$_4$ powder during photocatalytic reactions.* J. Phys. Chem. C, 2009. **113**(24): p. 10341-10345.

7. Shi, R., et al., *Visible-light photocatalytic degradation of BiTaO$_4$ photocatalyst and mechanism of photocorrosion suppression.* J. Phys. Chem. C, 2010. **114**(14): p. 6472-6477.

8. Yin, W., et al., *CTAB-assisted synthesis of monoclinic BiVO$_4$ photocatalyst and its highly efficient degradation of organic dye under visible-light irradiation.* Journal of hazardous materials, 2010. **173**(1): p. 194-199.

9. Fu, H., et al., *Visible-light-induced degradation of rhodamine B by nanosized Bi$_2$WO$_6$.* The Journal of physical chemistry B, 2005. **109**(47): p. 22432-22439.

10. Zhao, X., et al., *Photodegradation of dye pollutants catalyzed by γ-Bi$_2$MoO$_6$ nanoplate under visible light irradiation.* Applied Surface Science, 2009. **255**(18): p. 8036-8040.

11. An, H., et al., *Photocatalytic properties of BiOX (X= Cl, Br, and I).* Rare Metals, 2008. **27**(3): p. 243-250.

12. Yao, W.F., et al., *Photocatalytic property of bismuth titanate Bi$_2$Ti$_2$O$_7$.* Appl. Catal., A: General, 2004. **259**(1): p. 29-33.

13. Zou, Z., H. Arakawa, and J. Ye, *Substitution effect of Ta^{5+} by Nb^{5+} on photocatalytic, photophysical, and structural properties of BiTa$_{1-x}$Nb$_x$O$_4$ (0$\leqq$ x$\leqq$1.0).* J. Mater. Res. , 2002. **17**(06): p. 1446-1454.

14. Zhang, L., Y. Man, and Y. Zhu, *Effects of Mo replacement on the structure and visible-light-induced photocatalytic performances of Bi_2WO_6 photocatalyst.* Acs Catalysis, 2011. **1**(8): p. 841-848.

15. Garza-Tovar, L.L., *et al.*, *Photocatalytic degradation of methylene blue on Bi_2MNbO_7 (M= Al, Fe, In, Sm) sol–gel catalysts.* J. Mol. Catal. A: Chem. A: chemical, 2006. **247**(1): p. 283-290.

16. Ropero-Vega, J., *et al.*, *Photophysical and photocatalytic properties of Bi_2MNbO_7 (M= Al, In, Ga, Fe) thin films prepared by dip-coating.* Mater. Sci. Eng., B, 2010. **174**(1): p. 196-199.

17. Torres-Martinez, L.M., *et al. Photocatalytic performance of pyrochlore-type structure compounds, Bi_2MTaO_7 (M= Al, Ga, Fe or In), on alizarin red S degradation.* in *Proceedings of the 2nd WSEAS International Conference on Nanotechnology, World Scientific and Engineering Academy and Society (WSEAS), UK*. 2010.

18. Torres-Martinez, L.M., *et al.*, *Bi_2MTaO_7 (M= Al, Fe, Ga, In) photocatalyst for organic compounds degradation under UV and visible light.* WSeAS Trans environ dev, 2010. **6**: p. 286-295.

19. Pontonnier, L., *et al.*, *Relationships between structural and electric properties of pure and mixed protonic conductors.* Solid state ionics, 1990. **37**(4): p. 307-316.

20. Van Dijk, M., *et al.*, *Defect structures and migration mechanisms in oxide pyrochlores.* Solid State Ionics, 1985. **17**(2): p. 159-167.

21. Sirotinkin, V. and A. Bush, *Preparation and dielectric properties of $Bi_{1.5}MNb_{1.5}O_7$ (M= Cu, Mg, Mn, Ni, Zn) pyrochlore oxides.* Inorganic materials, 2003. **39**(9): p. 974-977.

22. Jiang, S., *et al.*, *Dielectric properties and tunability of cubic pyrochlore $Bi_{1.5}MgNb_{1.5}O_7$ thin films.* Applied Physics Letters, 2009. **94**(16): p. 162908-162908-3.

23. Shen, B., L. Kang, and X. Yao, *Dielectric properties of Bi_2O_3-ZnO-Ta_2O_5 ceramics sintered by microwave.* J. Electroceram. , 2008. **21**(1-4): p. 448-451.

24. Kayed, T. and A. Mergen, *Electrical properties of $Bi_{1.5}ZnSb_{1.5}O_7$ pyrochlore ceramics.* Crystal Research and Technology, 2003. **38**(12): p. 1077-1081.

25. Valant, M. and P. Davies, *Synthesis and dielectric properties of pyrochlore solid solutions in the Bi_2O_3-ZnO-Nb_2O_5-TiO_2 system.* J. Mater. Sci., 1999. **34**(22): p. 5437-5442.

26. Qasrawi, A., B.H. Kmail, and A. Mergen, *Synthesis and characterization of $Bi_{1.5}Zn_{0.92}Nb_{1.5-x}Sn_xO_{6.92-x/2}$ pyrochlore ceramics.* Ceram. Int. , 2012.

27. Qasrawi, A. and A. Mergen, *Structural, electrical and dielectric properties of $Bi_{1.5}Zn_{0.92}Nb_{1.5-x}Ta_xO_{6.92}$ pyrochlore ceramics.* Ceram. Int. , 2012. **38**(1): p. 581-587.

28. Mergen, A., *et al.*, *Fabrication and characterisation of Cr and Co doped $Bi_{1.5}Zn_{0.92}Nb_{1.5}O_{6.92}$ pyrochlores.* J. Am. Ceram. Soc. , 2011. **31**(14): p. 2633-2639.

29. Mergen, A., *et al.*, *Dielectric properties of Sm, Nd and Fe doped $Bi_{1.5}Zn_{0.92}Nb_{1.5}O_{6.92}$ pyrochlores.* Ceram. Int. , 2011. **37**(1): p. 37-42.

30. Du, H., X. Yao, and H. Wang, *Dielectric properties of pyrochlore $Bi_{1.5}Zn_{0.5}Nb_{0.5}M_{1.5}O_7$ (M=Ti, Sn, Zr, and Ce) dielectrics.* Appl. Phys. Lett. , 2006. **88**(21): p. 212901-212901-3.

31. Cann, D.P., C.A. Randall, and T.R. Shrout, *Investigation of the dielectric properties of bismuth pyrochlores.* Solid State Commun., 1996. **100**(7): p. 529-534.

32. Levin, I., *et al.*, *Structural study of an unusual cubic pyrochlore $Bi_{1.5}Zn_{0.92}Nb_{1.5}O_{6.92}$.* J. Solid State Chem. , 2002. **168**(1): p. 69-75.

33. Hong, W., D. Huiling, and Y. Xi, *Structural study of Bi_2O_3–ZnO–Nb_2O_5 based pyrochlores.* Mater. Sci. Eng., B, 2003. **99**(1): p. 20-24.

34. Withers, R., *et al.*, *Local crystal chemistry, induced strain and short range order in the cubic pyrochlore $(Bi_{1.5-\alpha}Zn_{0.5-\beta})(Zn_{0.5-\gamma}Nb_{1.5-\delta})O_{(7-1.5\alpha-\beta-\gamma-2.5\delta)}$ (BZN).* Journal of Solid state chemistry, 2004. **177**(1): p. 231-244.

35. Kamba, S., *et al.*, *Anomalous broad dielectric relaxation in $Bi_{1.5}ZnNb_{1.5}O_7$ pyrochlore.* Phys. Rev. B, 2002. **66**(5): p. 054106.

36. Perenlei, G., P.C. Talbot, and W.N. Martens, *Sol-gel synthesis and characterization of cubic bismuth zinc niobium oxide nanopowders.* Journal of Nanomaterials, 2014. **2014**.

37. Hinojosa, B.B., *Atomic structure effects on bulk and surface properties of mixed metal oxides from first principles simulations*. 2010, University of Florida.

CHAPTER   4

SUBSTITUTION OF Nb CATIONS BY Ta CATIONS ON THE *B* SITE OF THE CRYSTAL STRUCTURE OF THE BZN PARENT COMPOUND: $Bi_{1.5}ZnTa_{1.5}O_7$ (BZT)

4.1   FOREWORD OF THE CHAPTER

This chapter contains one journal paper that has been under revision for publication. This chapter/paper presents the results for an initial substitution to the parent BZN compound of chapter 3, where Nb is completely replaced by Ta, the element below Nb in the same column in the periodic table. Similar aspects to those investigated for BZN in chapter 3 have, in general, been investigated for $Bi_{1.5}ZnTa_{1.5}O_7$ (BZT). These aspects include sample preparation, characterisation of the optical properties, testing of the photocatalytic ability and DFT calculations of the electronic band structure. However, based on the optimised results for BZN prepared by sol-gel in the previous chapter, sol-gel is the only synthesis method used to prepare BZT in this chapter. Instead, more attention has been paid to the phase evolution as a function of temperature to determine the lowest sintering temperature required to prepare phase pure, fine-grained BZT materials, since the BZN compound has been prepared using sol-gel synthesis for the first time.

This chapter will also present the DFT calculations for the electronic band structures of BZT made under similar assumptions made for BZN, that is, for random, ordered and partially ordered solid solutions. In the BZT case, however, the computationally calculated band gap and the value estimated from the measured optical absorption spectra match remarkably well. In addition, we have found that less distorted cubic structures are obtained after geometry optimization during DFT calculations for substitutions at specific sites.

STATEMENT OF CONTRIBUTION OF CO-AUTHORS

The authors listed below have certified that:

1. They meet the criteria for authorship in that they have participated in the conception, execution, or interpretation, of at least that part of the publication in their field of expertise;
2. They take public responsibility for their part of the publication, except for the responsible author who accepts overall responsibility for the publication;
3. There are no other authors of the publication according to these criteria;
4. Potential conflicts of interest have been disclosed to (a) granting bodies, (b) the editor or publisher of journals or other publications, and (c) the head of the responsible academic unit; and
5. They agree to the use of the publication in the student's thesis and its publication on the QUT e-Prints database consistent with any limitations set by publisher requirements.

In the case of this paper:

Synthesis, Characterization and Electronic Structure Studies of Cubic Bi$_{1.5}$ZnTa$_{1.5}$O$_7$ for Photocatalytic Applications

Contributor	Statement of contribution
Ganchimeg Perenlei (PhD candidate)	Conducted all computational and experimental data collection and analysis, and manuscript writing.
Wayde N. Martens (Principal supervisor)	Assisted with experimental analysis and manuscript development.
Peter C. Talbot (Associate supervisor)	Assisted with computational analysis and manuscript development.
Jose A. Alarco (Associate supervisor)	Assisted with computational analysis and manuscript development.

Principal Supervisor Confirmation

I have sighted e-mail or other correspondence from all Co-authors confirming and certifying authorship.

Wayde Martens   4/11/15

_____

Name   Signature   Date

4.2   ARTICLE 3: "SYNTHESIS, CHARACTERIZATION AND ELECTRONIC STRUCTURE STUDIES OF CUBIC Bi$_{1.5}$ZnTa$_{1.5}$O$_7$ FOR PHOTOCATALYTIC APPLICATIONS"

Ganchimeg Perenlei,[1] Jose A. Alarco,[1,2] Peter C. Talbot[1,2] and

Wayde N. Martens[1]

[1]*School of Chemical, Physics and Mechanical Engineering, Science and Engineering Faculty,* [2]*Institute for Future Environments, Queensland University of Technology, Brisbane, QLD 4000, Australia*

ABSTRACT

Bi$_{1.5}$ZnTa$_{1.5}$O$_7$ (BZT) has been synthesized using an alkoxide based sol-gel reaction route. The evolution of the phases produced from the alkoxide precursors, and their properties have been characterized as function of temperature using a combination of thermogravimetric analysis (TGA) coupled with mass spectrometry (MS), infrared emission spectrometry (IES), X-ray diffraction (XRD), Ultraviolet and visible (UV-Vis) spectroscopy, Raman spectroscopy and N$_2$ adsorption/desorption isotherms. The lowest sintering temperature (600 °C) to obtain phase pure BZT powders with high surface area (14.5 m^2 g^{-1}) has been determined from the thermal decomposition and phase analyses. The photocatalytic activity of the BZT powders have been tested for the decolorization of organic azo-dye and found to be photoactive under UV irradiation. The electronic band structure of the BZT has been investigated using density functional theory (DFT) calculations to determine the band gap energy (3.12 eV) and to compare it with experimental band gap (3.02 eV at 800 °C) from optical absorption measurements. An excellent match is obtained for an assumption of Zn cation substitutions at specifically ordered sites in the BZT structure.

INTRODUCTION

Mixed metal pyrochlore oxides containing TiO_6, NbO_6 or TaO_6 octahedral units are a new class of photocatalysts [1-3]. The Bi-based pyrochlores, such as $Bi_2Ti_2O_7$, Bi_2MNbO_7 (M=Al, Fe, In, Sm) and Bi_2MTaO_7 (M=Al, Ga, In, Fe), have received significant attention in photocatalytic research [3-5]. Recently, another type of Bi-based pyrochlore Cu-doped $Bi_{1.5}ZnTa_{1.5}O_7$ prepared by conventional powder processing method in thick-film form, has also been examined for photocatalytic water splitting [6].

$3d$-transition metals have commonly been used as dopants for wide band gap photocatalysts, in order to narrow their band gaps [7, 8]. Several of these attempts have aimed at developing visible-light sensitive photocatalysts out of the initial UV-light responsive semiconductors. For instance, metal ions, such as Ni^{2+} and Cu^{2+}, have been doped into $InTaO_4$ and $BiTaO_4$ semiconductors, respectively [9, 10].

It has been hypothesized that the band gap value could be narrowed by raising the top of the valence bands due to the higher occupied M $3d$ orbitals of the dopants than O $2p$ orbitals [11]. However, many of the above mentioned investigations have often been experimentally driven and have not been matched with a corresponding level of detailed electronic band structure calculations. For example, there are limited reports in the literature about the effect of M^{2+} d-block transition metal dopants, such as Zn^{2+}, Cu^{2+}, Ni^{2+} or Co^{2+}, on the energy band structure of the pyrochlore materials.

We have recently investigated the properties and photocatalytic activity of BZN materials both experimentally and theoretically using density functional theory (DFT) calculations [12]. Conditions for good match between theoretical calculations and experimental results have been identified. In this paper, the phase evolution of BZT prepared by sol-gel synthesis has been characterized to determine the optimum temperature for phase pure formations and for optimized physical properties. The photocatalytic ability of the BZT powders has been tested for the decolorization of azo-dye aqueous solution under UV irradiation. Optical properties have been characterized by optical absorption spectroscopy and estimated experimental band gaps have been used as reference for comparison with calculations of the electronic band structure using DFT.

EXPERIMENTAL SECTION

Materials

Bismuth acetate (Bi(CH$_3$COO)$_3$), tantalum ethoxide (Ta(OC$_2$H$_5$)$_5$) and zinc acetate dihydrate (Zn(CH$_3$COO)$_2$•2H$_2$O) have been selected as sources of Bi, Ta and Zn, respectively. Solvents, such as 1,3-propanediol (CH$_2$(CH$_2$OH)$_2$) and acetic acid (C$_2$H$_4$O$_2$), have been used as complexing agents during synthesis. All these chemicals are of analytical grade ($\geq$ 99.9 %) and have been purchased from Aldrich (Australia). These starting materials have been used according to the required stoichiometric ratio to prepare cubic BZT with Bi$_{1.5}$ZnTa$_{1.5}$O$_7$ composition. The details of synthesis process have been described in our previous publication [13].

Characterization

Thermal analyses have been carried out on a viscous gel sample, which had been previously prepared at 200 °C from the liquid suspension of precursors, using thermogravimetric analysis (TGA) coupled with mass spectrometry (MS) and infrared emission spectrometry (IES). The results have been used to determine the lowest temperature to form organic free powders. X-ray diffraction (XRD), Ultraviolet-visible (UV-Vis) spectroscopy, Raman spectroscopy and N$_2$ adsorption/desorption isotherms have been employed to characterize further the powder samples prepared at various temperatures.

Photocatalytic Reaction

The photocatalytic ability of the BZT powders for the decolorization of azo-dye aqueous solution has been tested using UV light irradiation. A starting 20 ppm solution of Acid orange 7 (AO7), dispersed with 0.1 g of powders, has been used in the reaction. The diminishing concentration of the AO7 dye has been monitored by UV-Vis spectroscopy, recording its maximum absorption peak (λ_{max}) at a wavelength of *ca.* 485 nm, in the visible light region. The light source used in this experiment is a 15 W NEC blacklight FL15BL (wavelength of *ca.* 365 nm).

THEORETICAL CALCULATIONS

Bi$_{1.5}$ZnTa$_{1.5}$O$_7$ Structure

The crystal structures of BZT used in DFT calculations have been taken or adapted from the *Crystallographic Information File* (CIF) of the Inorganic Crystal Structure Database (ICSD) for BZT. Cubic BZT from the CIF file (JCPDS PDF, 04-013-6484) has a lattice parameter *a*=10.54 (Å) and contains fractionally occupied cations with ratios of Bi/Zn=75:25 and Ta/Zn=75:25 in the *A* and *B* sites, respectively. This random, fractionally occupied, solid solution structure has also been modified to completely or partially ordered solid solutions, by making all or some of the Zn substitutions at specific sites of the structure, respectively.
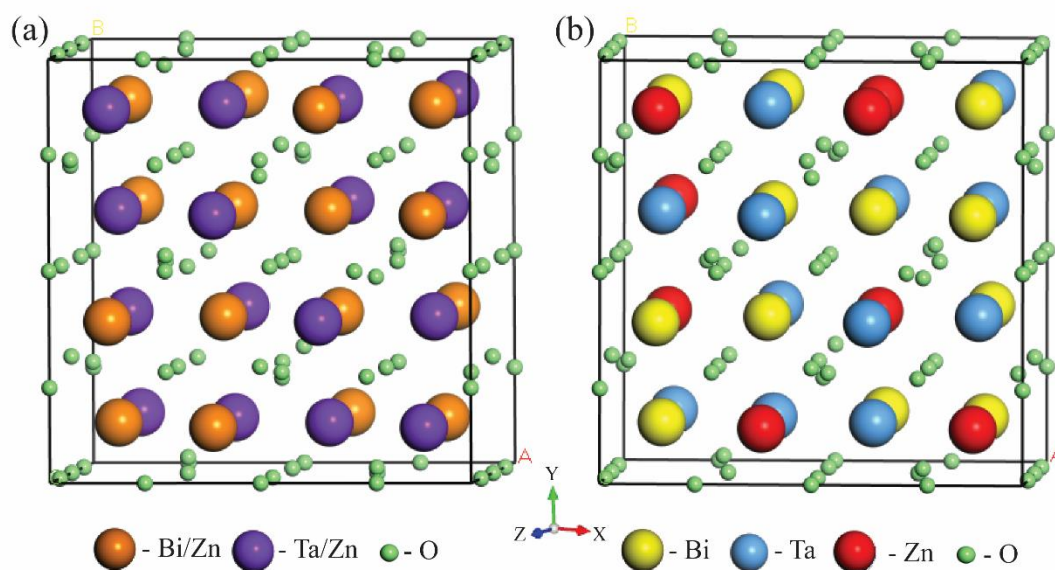

Figure 4-1: BZT structures assuming: (a) random and (b) ordered solid solutions (pure Bi, Ta, Zn and O atoms are yellow, blue, red and green balls, while Bi/Zn and Ta/Zn mixed cations are orange and purple balls, respectively)

Figure 4-1(a) shows a schematic of the random solid solution. Atoms are displayed using a ball and stick style, where mixed cations of Bi/Zn and Ta/Zn are orange and purple balls, respectively, and pure O anions are green balls. An example of the BZT ordered (completely) solid solution is displayed in Figure 4-1(b). This example results in the most representative and consistent calculations with experimental results. In the case for ordered solid solution, yellow, blue and green balls are pure Bi, pure Ta cations and pure O anions, while red balls are substituted Zn cations at the *A* and *B* sites, respectively. In the case for partially ordered BZT solid solution structures, the Zn substitution at either the *A* or the *B* sites is randomly substituted, while the other site is ordered, or vice versa.

Electronic Structure Calculations

The energy band structure and density of states (DOS) of the BZT compound have been calculated using DFT, as implemented in the Cambridge Serial Total Energy Package (CASTEP) of Materials Studio 8.0. In all calculations, the structures have been geometry and cell optimized. Both the local density approximation (LDA) with Ceperley and Alder exchange correlation functional parametrized by Perdew and Zunger (CP) and the generalized gradient approximation (GGA) with Perdew-Burke-Ernzerhof (PBE) functionals with norm-conserving pseudopotentials have been used along with setups non-metal, non-spin and 100 empty orbitals. For random solid solutions, the ultra-fine convergence tolerance setup has been used with k-grid of 0.03 A^{-1}, which gives k-point mesh of 6×6×6 and plane wave basis set cut-off of 830 eV.

In the case of ordered solid solutions, for the calculations to achieve convergence, default criteria have been customized to less demanding values than used for the random solid solution calculations. Final convergence has been achieved with customized tolerance setups for energy = 5.0×10^{-5} eV atoms^{-1}, force = 0.03 eV Å^{-1}, stress = 0.02 GPa and displacement = 5.0×10^{-3} Å, respectively, with k-grid of 0.07 A^{-1}, which gives a k-point mesh of $2 \times 2 \times 2$ and plane wave basis set cut-off energy of 750 eV. Moreover, for the partially ordered solid solutions, fine convergence default setups for energy = 1.0×10^{-5} eV atoms^{-1}, force = 0.03 eV Å^{-1}, stress = 0.05 GPa and displacement = 1.0×10^{-3} Å, respectively, with k-grid of 0.03 A^{-1}, which gives a k-point mesh of $4 \times 4 \times 4$ and cut-off energy of 750 eV have been successfully used in the calculation.

RESULTS AND DISCUSSION

TGA Analysis

The thermogravimetric (TG) and differential thermogravimetric (DTG) curves of the gel sample are shown as dash and solid lines in Figure 4-2, respectively. TGA analysis shows that the decomposition of the gel sample can be divided into three main mass loss events, which correspond to the peaks observed at 85 - 145, 265 and 345 °C in the DTG curve and to 80, 5 and 3 % of the total mass loss, respectively. With further increases in heating temperature up to 800 °C, no significant additional mass loss has been observed, which may be an indication of no volatility of metallic Bi or any other metals.
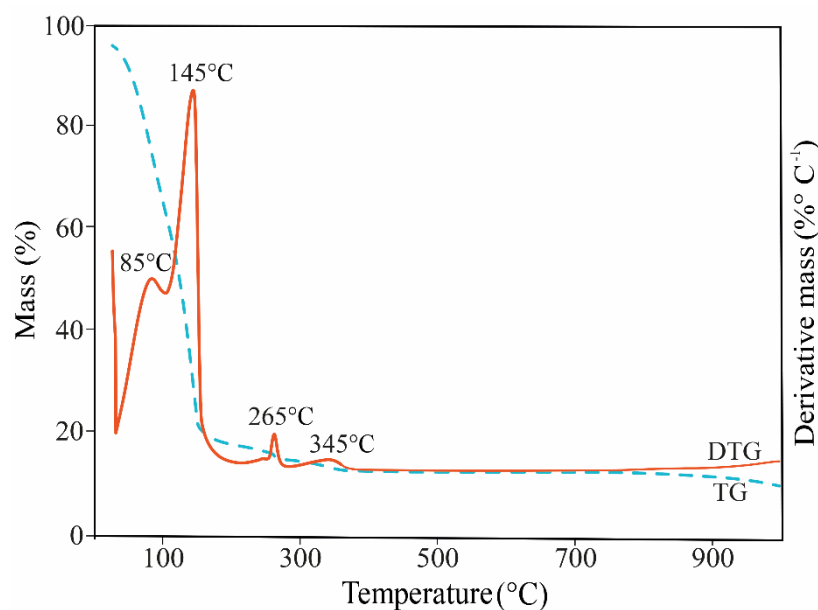

Figure 4-2: TG/DTG curves of the gel sample that heated from 25 to 1000 °C

IES Analysis

The IES spectra collected in the range of 650 - 4000 cm^{-1} from the gel sample while heating from 200 to 350 °C on the platinum nail surface used in the IES experiments are shown in Figure 4-3. Absorption peaks have appeared at various wavenumbers for the sample heated at 200 °C. These peak intensities have noticeably decreased with increasing temperature up to 300 °C, and most of these peaks have then disappeared from 350 °C onwards.
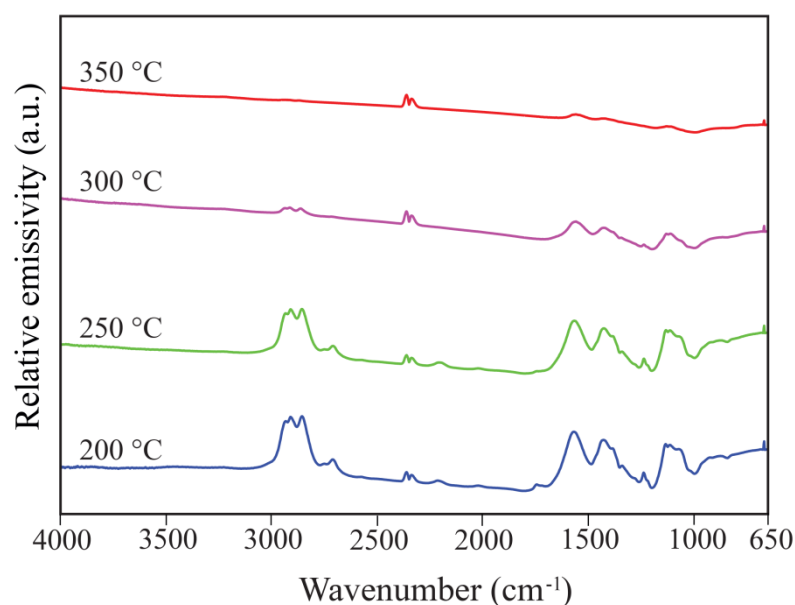
Figure 4-3: IES spectra of the gel sample heated at various temperatures

Bands between 2700 and 2800 cm^{-1} and 1450 - 1475 cm^{-1} are due to saturated –C–H stretching and deformations found in the form of –CH$_2$ and –CH$_3$, respectively. The peaks obtained at 2700 - 2800 cm^{-1} are due to either –O–CH$_3$ or –O–CH$_2$–O– groups, while a small peak at 3200 - 3550 cm^{-1} may correspond to –OH groups. A single sharp peak associated with saturated ester or carboxylic acid –CO–O bonds at about 1735 - 1750 cm^{-1} has also been observed in the spectra. Moreover, broad peaks of –C–C, –C–O and –C=C stretches are also found in the regions around 1000, 1300 and

1640 cm^{-1}, respectively. CO_2 peaks appear at 2350 cm^{-1} at all temperatures due to the experiment being carried out in ambient air. This result indicates that the organic compounds in the precursors have completely decomposed before the powders form at 350 °C, which is in agreement with the TGA results.

MS Analysis

The detected ion currents of evolved gasses from the thermal decomposition of the gel sample are well matched with the evolution of water and fragmentation of organic compounds at particular decomposition temperatures. The water dehydration has occurred at several different event temperatures in the form of O (*m/z=16*), OH (*m/z=17*) and H_2O (*m/z=18*) as shown in Figure 4-4(a). The vaporization of large amount of water takes place at about 100 °C and it is probably the result of dehydration of zinc acetate dihydrate or reaction between organic solvents during the synthesis process [14]. Small amount of higher temperature water dehydrations at 270, 355 and 500 °C have also been observed in the MS curves.

Figure 4-4(b) illustrates the sharp peaks obtained in the ion current curves at 100 °C, which may be assigned to CH_3 (*m/z=15*)*, CH_3CO (*m/z=43*), COOH (*m/z=45*) and CH_3COOH (*m/z=60*). These peaks could be the result of a vaporization of an excess of organic solvents in the gel sample, such as acetic acid, propanediol or other organics. Additional organic decompositions are observed at 270 and 335 °C, which may correspond to the elimination of remaining organic radical groups polymerized with the metals and subsequently allowing the crystallization of organic free -Bi-O-Zn-O-Ta- metal oxide mixture.
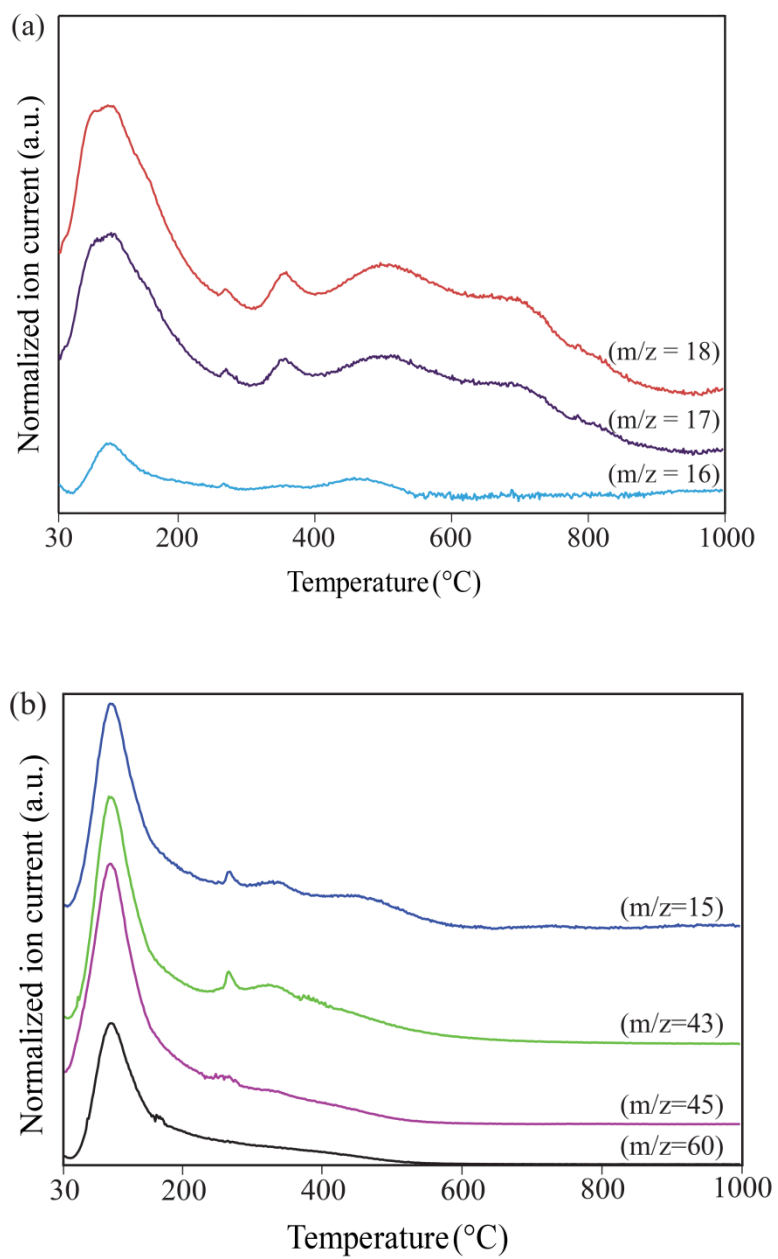
Figure 4-4: Ion currents in the MS curves a) water and b) organics

SEM Analysis

Figure 4-5 shows the backscattered SEM images of the gel and powder samples prepared at different temperatures. The uniformity of the contrast indicates that the elemental distribution of the microparticles is relatively homogeneous.
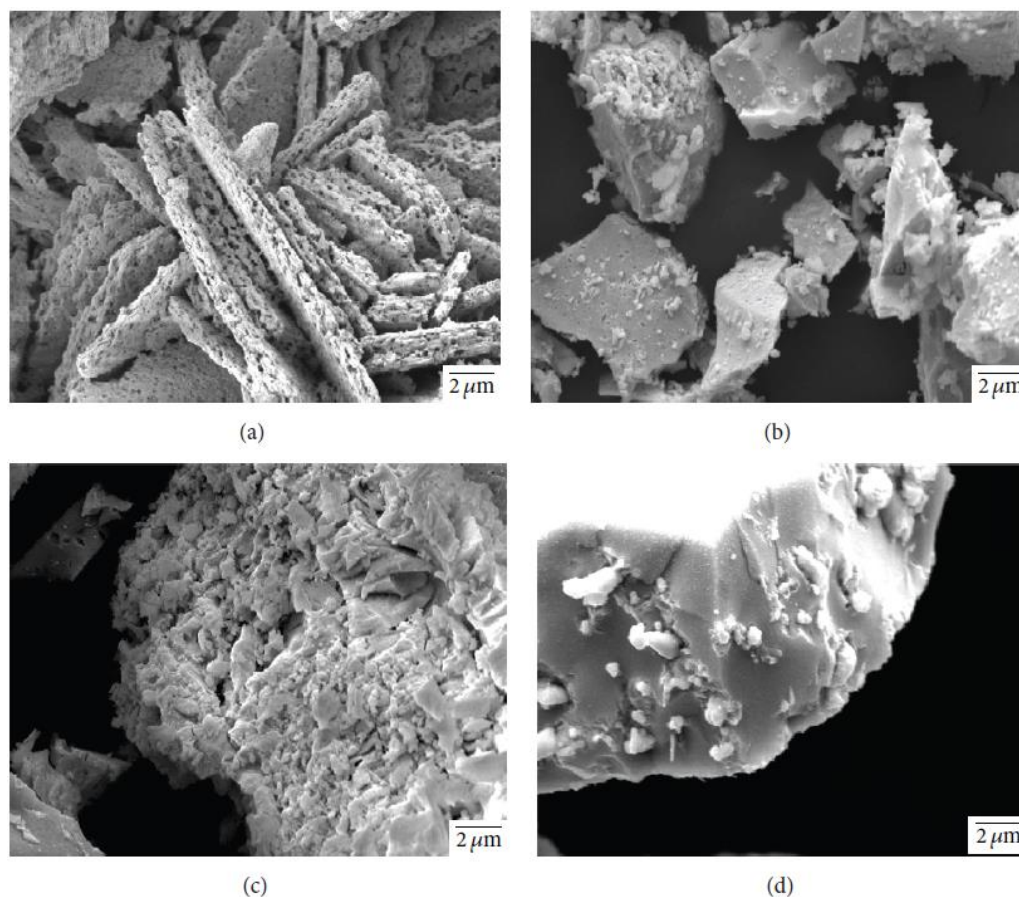
Figure 4-5. SEM images of samples prepared at a) 200 °C, b) 400 °C, c) 600 °C and d) 800 °C (all images have same scale of 2 μm)

The SEM micrograph in the Figure 4-5(a) illustrates the long-sheet like porous gel sample that consists of small clusters with a thickness of 500 - 700 nm. Figure 5-5(b and c) show the SEM micrographs of powder samples prepared at 400 and 600 °C, which consist of particles of 0.5 and 20 μm sizes, respectively. At higher temperatures, grain growth is observed and the powders develop a dense

microstructure with large clusters in the form of > 5 μm thick plates, exceeding 30 μm diameters when the sample is heated at 800 °C as shown in Figure 4-5(d).

XRD Analysis

X-ray diffraction has been employed to identify the crystalline phases at various sintering temperatures. Diffraction patterns of thermally treated powders prepared at 400 - 800 °C are shown in Figure 4-6. The compounds obtained at the lower temperatures of 400 and 500 °C are believed to be a mixture of intermediate phases. The main peaks are corresponded to $Bi_{7.84}Ta_{1.61}O_{14.78}$ in the database. With an increase of sintering temperature, however, single phase BZT crystals are obtained at 600 °C onwards. All the main peaks can be matched to those of cubic $Bi_{1.5}ZnTa_{1.5}O_7$ (JCPDS PDF, 04-013-6484). The peak widths become narrow with increasing temperature, indicating higher crystallinity. BZT crystallite sizes calculated from the Scherrer equation are 32 - 48 nm at 600 - 800 °C, respectively.
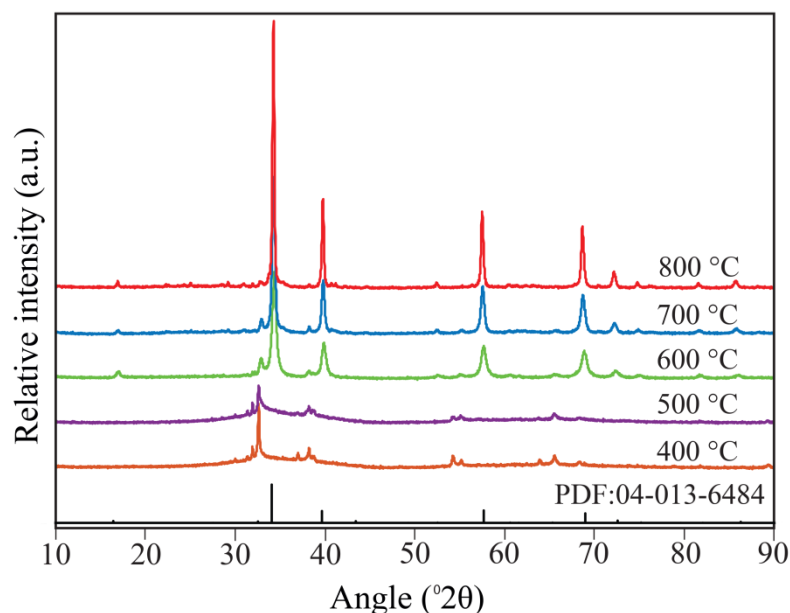

Figure 4-6: XRD patterns of powder samples prepared at various temperatures

(the bottom pattern is the cubic BZT with PDF card number)

XPS analysis has been carried out on the powder sample sintered at 800 °C. The surface composition of the BZT has been calculated based on atomic ratio of each metal in the compound. The peak areas of Bi 4f (at 159 and 165 eV), Zn 2p (at 1021.68 eV) and Ta 4f (at 26.5 and 27.5 eV) have been measured, and quantification of the peaks gives the atomic ratio of Bi:Zn:Ta to be approximately 1.6: 1: 1.7 on the surface of the BZT pyrochlores. The XPS results have also confirmed that the oxidation states of each cation are Bi^{3+}, Zn^{2+} and Ta^{5+}, respectively, at that temperature.

Raman Spectroscopy Analysis

Raman spectrometry in the wavenumber range of 100 - 1000 cm^{-1} has confirmed the XRD results for the phase formations at various temperatures. Figure 4-7(a) presents Raman spectra collected on a gel sample prepared at 200 °C and on powder samples heated at 400 and 500 °C, respectively. The changes in relative peak heights and positions show the occurrence of a phase transformation. Two intense and narrow peaks at 186 and 316 cm^{-1} and three small shoulder peaks at 466, 635 and 787 cm^{-1} are found on the Raman spectra from the powders prepared at 500 °C. These peaks are probably due to the intermediate oxides identified using XRD analysis.

Raman spectra of the powder samples sintered at 600 - 800 °C are displayed in Figure 4-7(b). The peaks obtained at 285, 445, 557, 615 and 745 cm^{-1} at all temperatures that consist of broad bands and shoulders are closely matched with those published for BZT in the literature [15]. However, the peaks found at 135, 150 and 235 cm^{-1} are not reported in previous work; the spectra were collected between 250 and 1000 cm^{-1} only. With increasing temperature from 600 to 800 °C, the peak

positions remain unchanged; yet, the features become more pronounced, which is probably due to larger sized grains and particles formed at higher temperature.
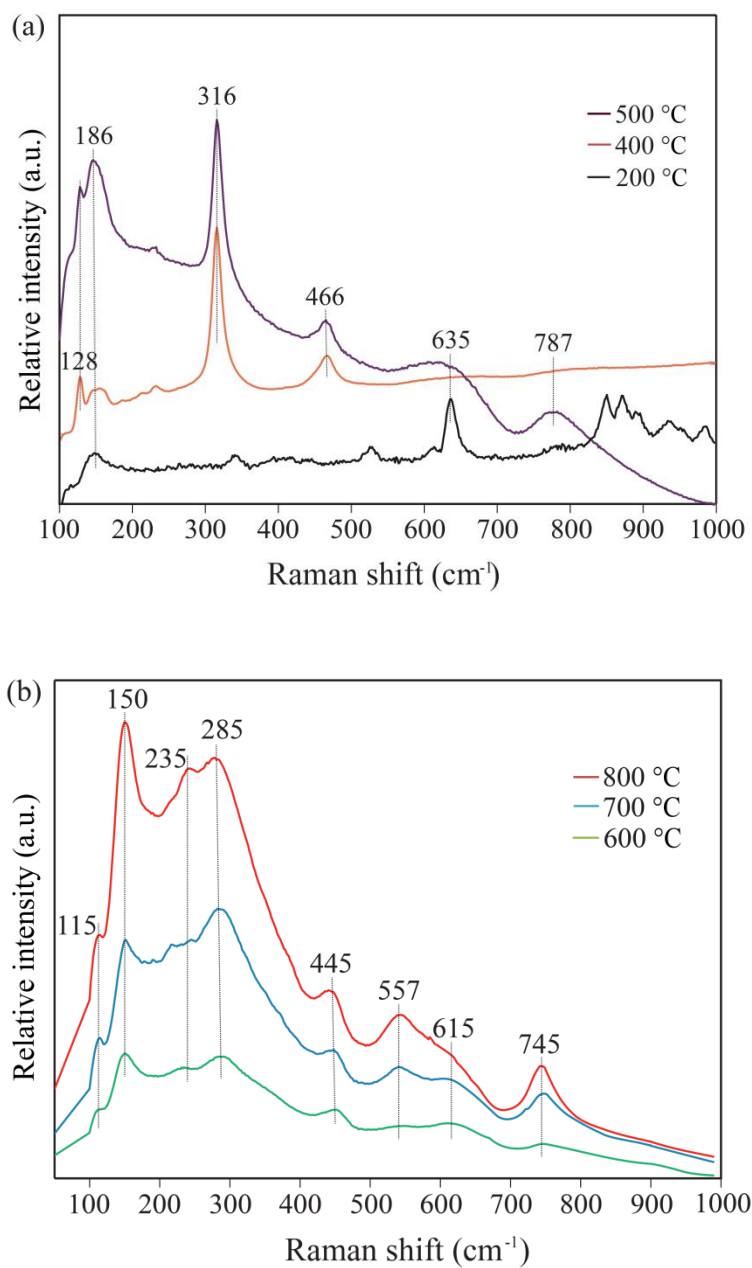
Figure 4-7: Raman spectra of samples prepared at various temperatures

UV-Vis Spectroscopy Analysis

Figure 4-8 displays the optical absorption edges of BZT powders prepared at various temperatures. The absorption curves at 400 and 500 °C clearly show that samples consist of a mixture of different phases. However, at higher sintering temperature, single phase BZT powders show optical absorptions at wavelengths about 410 - 450 nm in the UV light region. The estimated optical band gaps of cubic BZT compounds obtained at 600, 700 and 800 °C are about 2.75, 2.95 and 3.02 eV, respectively, which is comparable to previously reported values of 2.5 - 3.2 eV in the literature [15].
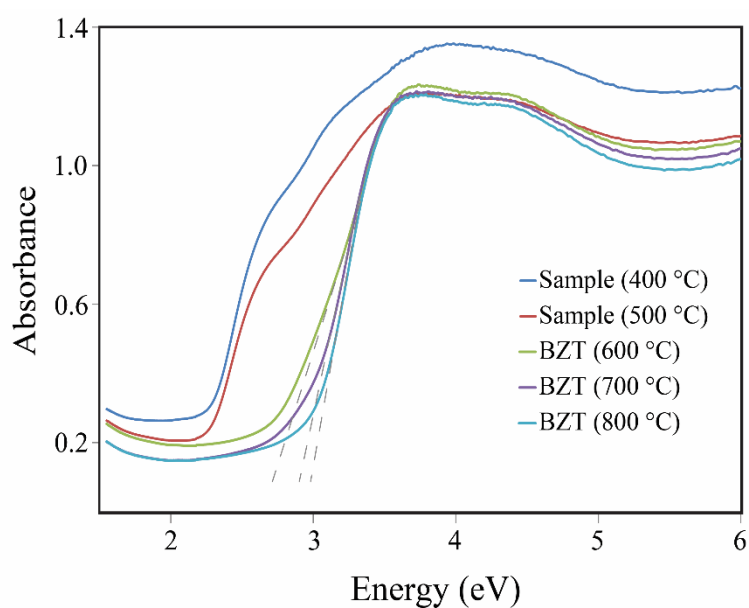
Figure 4-8: UV-Vis spectra of powder samples prepared at various temperatures

Photocatalytic Dye Decolorization

The photocatalytic activity of the BZT compound has been evaluated for the decolorization of AO7 (λ_{max} = 485 nm) solution under UV irradiation for 60 min. Figure 4-9 shows the changes in the dye concentration in the presence of BZT powders prepared at 600 - 800 °C. The results indicate that BZT is photoactive under UV light with wavelength of *ca.* 365 nm and that the photocatalytic degradation of the azo-dye in aqueous media is achieved with assistance of the BZT catalyst, photoexcited by UV irradiation. As expected, the low temperature catalyst at 600 °C has shown better performance than higher temperature catalysts, which correlates with its higher surface area (14.5 m^2 g^{-1}) when compared to that of BZT powders prepared at 800 °C (0.47 m^2 g^{-1}). These results are similar to our previous photocatalysis results using BZN powders [16].
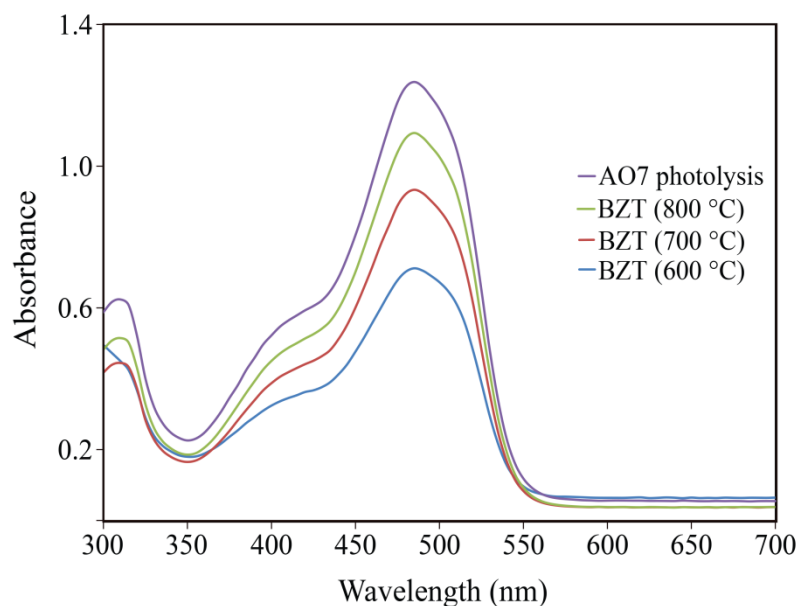
Figure 4-9. AO7 dye absorption curves (λ_{max} = 485 nm) after photocatalytic degradation for 60 min under UV irradiation in the presence of the BZT catalysts prepared at various temperatures

Electronic Structure Calculation

All attempts to calculate the electronic band structure of the BZT with complete fractional occupancy have resulted in metallic-like materials without band gaps near or from the Fermi level. The lattice parameter of this calculated cubic structure is a=10.22 Å. These results have been consistent for all different settings (k-grid, cut-off energy, spin-polarized and unpolarised, etc.) for both cubic and primitive structures used in the calculations.

The calculated results obtained from the DOS for BZT random solid solution have revealed that the bands near the Fermi level contain mainly d and a small amount of p orbitals. Supplementary calculations with gradual amounts of Zn substituted in the structures have shown that these bands arise mainly from Ta $5d$ orbitals that are driven downwards in energy by the involvement of Zn cations in the B site of the BZT structure. Fractional occupancy of Zn in the A sites does not show such a marked effect. Since this has not reflected the experimentally observed optical results, completely and partially BZT ordered solid solutions have also been explored in the DFT studies.

The electronic structure and DOS calculations for the BZT ordered solid solution are shown in Figure 4-10. After the calculations, the cubic structure (a=10.54 Å) has been slightly contracted and converted to rhombohedral structure with lattice parameter a=10.42 Å and angles of 90.13°, which clearly represents a very small distortion from the input cubic structure. The obtained final enthalpy of formation of -58449.02 eV for the BZT ordered solid solution is generally lower than the enthalpy of formation of -55972.85 eV for the cubic BZT random solid solution, which is generally taken as an indication of favourable formation. Figure 4-10(a) shows a

band gap, which is calculated as 3.12 eV between the dense VB and CB bands, which compares very well with experimentally estimated band gaps of 2.75 - 3.02 eV for optical absorption measurements.

Figure 4-10(b) shows the total and partial DOS for overall BZT and individual atoms, respectively. The VB bands mainly consist of O 2*p*, Bi 6*s*, Bi 6*p* and Ta 5*d* states, whereas the CB bands consist mainly of Ta 5*d*, Bi 6*p* and O 2*p* states. With respect to the contribution of Zn to the energy band structure, a pronounced peak of 3*d* states is obtained between -5.5 and -7.0 eV. This energy level is several eVs below the Fermi level and it may therefore only contribute indirectly to the determination of the size of the band gap.
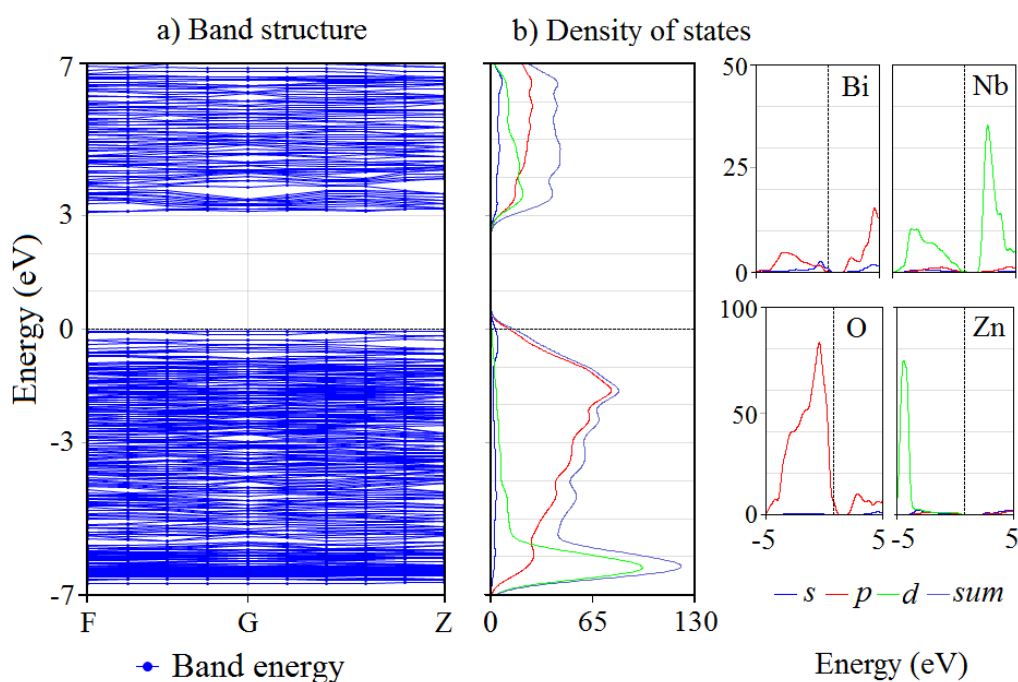
Figure 4-10: The band structure and DOS for the BZT ordered solid solution structure

The partially ordered solid solution, in the *A* and *B* sites, produced calculated band structures that more closely matched the experimental results. The lattice parameter of this calculated cubic structure is a=10.44 Å and the band gap is 1.86 eV. In addition to the continuous bands, the calculation for the partial solid solution also appears to show a few localized bands inside the band gap. These bands seems to be impurity bands, which are due to Zn *s* orbitals in both VB and CB levels as a result of mixed Bi/Zn cations in the random solid solution. Such impurity bands may act as traps for photogenerated electrons or holes during the photocatalytic reaction. The dense groups of states at the VB and the CB above the localized bands are separated by about 3.5 eV, which corresponds to the optical absorption edge. This value is slightly higher than the experimentally determined absorption edge and the value obtained for the completely ordered solid solution calculations.

In contrast, when Zn is randomly substituted in the *A* and ordered in the *B* sites, the electronic band structure calculation results show no band gap, which is similar to the calculated results from the random solid solution (for the unpolarized case). In this case, Ta *d* orbitals are driven downwards in energy by the involvement of Zn cations in the *B* site of the BZT structure as Ta/Zn mixed random cations.

CONCLUSIONS

Single-phased cubic BZT has been successfully synthesized using an alkoxide based sol-gel reaction route. The lowest temperature required for phase purity and maximum surface area has been determined to be around 600 °C through the characterization of the phase evolution from the alkoxide precursors as function of temperature. The BZT has been found to be UV light responsive, as determined from the photocatalytic degradation of azo dye in aqueous solution. Band gaps of 2.75 - 3.02 eV have been estimated from optical absorption measurements and have been used as reference for detailed DFT investigations of the electronic band structure, assuming both random and ordered solid solutions. Random solid solutions, which correspond to CIF files generated from refinements of XRD patterns, have resulted in complete absence of electronic band gaps. This is the case whether unpolarised or polarized spins are assumed. To obtain an electronic band gap, ordered solid solutions have been required. A selected ordered solution has resulted in a calculated band gap of 3.12 eV, which appears clean, without impurity bands and matches very well the experimentally estimated band gaps. It should be noted that this choice of substitution results in reduction of the symmetry to rhombohedral after geometry optimization. By choosing a partially ordered solid solution, a slightly larger band gap can be obtained while retaining the cubic symmetry after geometry optimization.

REFERENCES

1.   Zou, Z., J. Ye, and H. Arakawa, *Structural properties of InNbO$_4$ and InTaO$_4$: Correlation with photocatalytic and photophysical properties.* Chem. Phys. Lett. , 2000. **332**(3): p. 271-277.

2.   Muktha, B., *et al.*, *Crystal structures and photocatalysis of the triclinic polymorphs of BiNbO$_4$ and BiTaO$_4$.* J. Solid State Chem. , 2006. **179**(12): p. 3919-3925.

3.   Yao, W.F., *et al.*, *Photocatalytic property of bismuth titanate Bi$_2$Ti$_2$O$_7$.* Appl. Catal., A: General, 2004. **259**(1): p. 29-33.

4.   Torres-Martinez, L.M., *et al.*, *Bi$_2$MTaO$_7$ (M= Al, Fe, Ga, In) photocatalyst for organic compounds degradation under UV and visible light.* WSeAS Trans environ dev, 2010. **6**: p. 286-295.

5.   Garza-Tovar, L.L., *et al.*, *Photocatalytic degradation of methylene blue on Bi$_2$MNbO$_7$ (M= Al, Fe, In, Sm) sol–gel catalysts.* J. Mol. Catal. A: Chem. A: chemical, 2006. **247**(1): p. 283-290.

6.   Sun, J., *et al.*, *A novel Bi$_{1.5}$Zn$_{1-x}$Cu$_x$Ta$_{1.5}$O$_7$ photocatalyst: water splitting properties under visible light and its electronic structures.* international journal of hydrogen energy, 2012. **37**(17): p. 12960-12966.

7.   Hameed, A., M. Gondal, and Z. Yamani, *Effect of transition metal doping on photocatalytic activity of WO$_3$ for water splitting under laser illumination: role of 3d-orbitals.* Catalysis Communications, 2004. **5**(11): p. 715-719.

8.   Zou, Z., *et al.*, *Effect of 3d transition-metal (M) doping in In$_{1-x}$M$_x$TaO$_4$ photocatalysts on water splitting under visible light irradiation.* Studies in Surface Science and Catalysis, 2003. **145**: p. 165-168.

9.   Zou, Z., J. Ye, and H. Arakawa, *Effect of Ni substitution on the structure and photocatalytic activity of InTaO$_4$ under visible light irradiation.* Journal of materials research, 2002. **17**(06): p. 1419-1424.

10.   Zhang, H., *et al.*, *Electronic structure and water splitting under visible light irradiation of BiTa$_{1-x}$Cu$_x$O$_4$ (x=0.00–0.04) photocatalysts.* International Journal of Hydrogen Energy, 2009. **34**(9): p. 3631-3638.

11.   Tong, H., *et al.*, *Nano-photocatalytic materials: Possibilities and challenges.* Advanced Materials, 2012.

12.   Stampfl, C., *et al.*, *Electronic structure and physical properties of early transition metal mononitrides: Density-functional theory LDA, GGA, and screened-exchange LDA FLAPW calculations.* Physical Review B, 2001. **63**(15): p. 155106.

13.   Perenlei, G., P.C. Talbot, and W.N. Martens, *Sol-gel synthesis and characterization of cubic bismuth zinc niobium oxide nanopowders.* Journal of Nanomaterials, 2014. **2014**.

14.   Ghule, A.V., *et al*., *In situ thermo-TOF-SIMS study of thermal decomposition of zinc acetate dihydrate.* J. Mass Spectrom. , 2004. **39**(10): p. 1202-1208.

15.   Zanetti, S.M., M.G.S. Pereira, and M.C.A. Nono, *Soft-chemical derived Bi_2O_3-ZnO-Ta_2O_5 nanopowder and ceramics.* J. Eur. Ceram. Soc., 2007. **27**(13-15): p. 3647–3650.

16.   Perenlei, G., *et al*., *Electronic structure studies and photocatalytic properties of cubic $Bi_{1.5}ZnNb_{1.5}O_7$.* International Journal of Photoenergy, 2015. **2015**(575376): p. 1-11.

CHAPTER 5

EFFECTS OF SUBSTITUTION OF ADDITIONAL TRANSITION METALS INTO THE PARENT STRUCTURE FOR DESIGNING NARROW BAND GAP PHOTOCATALYSTS

5.1   FOREWORD OF THE CHAPTER

In this chapter, the effects of substitution of additional transition metals into the electronic band structures of the parent compounds have been systematically investigated using DFT calculations. Theoretical results are compared to experimentally determined band gaps from optical absorption measurements. The objective has been to further confirm the trends and correlations identified with the previously selected materials and to focus more on establishing the observation as a more general tool for the engineering and optimisation of the electronic band gaps and structures. BZN and BZT have been kept as the reference parent compounds in these investigations.

This chapter includes two draft research papers that have been prepared for submission to scientific journals. The first paper shows the effect that replacing Cd (with larger atomic radius) for Zn cations has on the electronic structure. The second paper discusses the effect of a wide range of metal substitutions in both *A* and *B* sites of the BZN and BZT compounds to identify a more general trend. In this latter case, the Zn cations on both sites have been substituted by other transition metals with similar ionic radii but fewer electrons. During the investigation, Nb cations on the *B* site of the BZN crystal structure have also been replaced by V or Ta cations.

Similar solid solution approaches developed in the previous research papers, namely chapters 3 and 4, have been applied to the electronic structure investigations in this chapter. Previous work in chapter 3 has shown that the optical absorption edges of the materials are not very sensitive to the synthesis technique or sintering temperature. Therefore, all compounds investigated in this chapter have been

prepared using a solid-state method, due to its simplicity, without attempting to optimise the surface properties.

5.2 ARTICLE 4: "SYNTHESIS, OPTICAL AND ELECTRONIC PROPERTIES OF $Bi_{1.5}CdM_{1.5}O_7$ (M = Nb, Ta)"

Ganchimeg Perenlei,[1] Jose A. Alarco,[1,2] Peter C. Talbot[1,2] and Wayde N. Martens[1]

[1]*School of Chemical, Physics and Mechanical Engineering, Science and Engineering Faculty,* [2]*Institute for Future Environments, Queensland University of Technology, Brisbane, QLD 4000, Australia*

ABSTRACT

$Bi_{1.5}CdM_{1.5}O_7$ (M = Nb, Ta) compounds have been synthesized by conventional solid-state reactions and their crystal structures have been characterized by powder X-ray diffraction. The optical band gaps have been measured in the UV region using UV-Vis absorption spectroscopy. First principles calculations of the electronic structures and density of states have been applied for the structures assuming ordered and partially ordered BCdM (M = Nb, Ta) solid solutions. Calculated band gaps are in good agreement with experimentally estimated band gap values. The obtained theoretical and experimental results from BCdN and BCdT structures have also been compared with those from BZM (M = Nb, Ta) solid solutions. Cd 4*d* and Zn 3*d*-orbitals introduce only minimal differences in the band gap values for the respective BCdM and BZM (M = Nb, Ta) compounds.

INTRODUCTION

Heterogeneous photocatalysis has great potential to assist with environmental pollution reduction. The technology has been used for water purification processes including degradation of organic pollutants, removal of heavy metal pollutants and disinfection of microorganisms from wastewater [1-5].

Various types of compounds have been prepared by different methods for development of new effective photocatalytic materials (mostly titania-based) [6-10]. These materials must be active under visible light irradiation to become sustainable in practical applications. However, most of the materials do not meet this requirement. This has driven researchers to search for different types of semiconductor materials that can utilize photons in the visible light regions.

Bismuth oxide (Bi_2O_3)-based photocatalysts, particularly in the Bi_2O_3-Nb_2O_5 and Bi_2O_3-Ta_2O_5 systems, have not been extensively investigated, despite Bi being a potential candidate for valence band (VB) control through Bi $6s$ and O $2p$ hybrid orbitals [11]. The most investigated photocatalysts closely related to the above-mentioned systems are $Bi_2MM'O_7$ (M = Al, Ga, In, Fe, Y, rare earth; M' = Nb, Ta), $MBi_2M'_2O_9$ (M=Ca, Sr, Ba, Pb; M' = Nb, Ta) or $BiTa_{1-x}Nb_xO_4$ ($0 \leq x \leq 1$) [12-17].

In addition, for most photocatalysts, loading of transition metals as co-catalysts is often necessary to achieve activities in applications such as water splitting [14]. The influence of transition metals on the crystal and electronic band structures is of interest in order to understand the photocatalytic properties of the materials. Thus, it is interesting to examine the optical properties and electronic band structures of $Bi_{1.5}MM'_{1.5}O_7$ (M = Zn, Cd, Cu, Ni, Co; M' = Nb, Ta), which accommodate a wide

range of transition metals substitutions without significant changes in the crystal structures. Such insight and understanding may then help to tailor substitutions into wide-band gap semiconductors in order to design new, more efficient photocatalysts, which are sensitive to visible light, by inducing appropriate narrowing of the band gap.

In this paper, $Bi_{1.5}CdM_{1.5}O_7$ (M = Nb, Ta) compounds with pyrochlore structures have been prepared and their optical properties and electronic band structures have been systematically investigated using a combination of optical absorption measurements and density functional theory (DFT) calculations.

EXPERIMENTAL SECTION

Material Preparation

All starting materials used in the experiments are of analytical grade ($\geq$ 99.9%), purchased from Aldrich (Australia), and used according to the required stoichiometric ratio to prepare $Bi_{1.5}CdM_{1.5}O_7$ (M = Nb, Ta). Bismuth oxide (Bi_2O_3), niobium oxide (Nb_2O_5), tantalum oxide (Ta_2O_5) and cadmium nitrate tetrahydrate ($Cd(NO_3)_2 \cdot 4H_2O$) have been used as starting reagents to prepare bismuth cadmium niobium and tantalum oxides (BCdN and BCdT). A solid-state technique has been employed for the preparation of samples at 1000 °C for 5 h.

Material Characterization

The crystal structures of the synthesized powders have been characterized by X-ray diffraction (XRD). The diffraction patterns have been collected in Bragg-Brentano geometry in the range 5.0 - 90 °2θ on a spun stage using a Philips PANalytical X'Pert PRO X-Ray Diffractometer. The incident X-rays have been generated from a PW3373/00 Co X-ray tube operating at 40 kV and 40 mA, providing Kα1 wavelength of 1.7903 Å. The optical absorption spectra have been recorded in the wavelength regions of 200 - 800 nm by Ultraviolet-Visible (UV-Vis) spectroscopy using a UV-Vis-NIR Cary 5000 Stheno spectrometer.

THEORETICAL CALCULATIONS

Electronic band structure and density of states (DOS) calculations have been carried out using DFT, as implemented in the Cambridge Serial Total Energy Package (CASTEP) of Materials Studio 8.0. All structures have been optimized for geometry and cell parameters. The generalized gradient approximation with Perdew-Burke-Ernzerhof (GGA-PBE) functional and norm-conserving pseudopotentials has been adopted along with 100 empty orbitals, non-metal, non-spin and customized convergence tolerance setups as mentioned in our previous reports [18, 19].

The *Crystallographic Information File* (CIF) for the BZT structure (JCPDS PDF, 04-013-6484) from the Inorganic Crystal Structure Database (ICSD) has been used as the initial structure for all DFT calculations, after appropriate substitutions. The starting structure contains fractionally occupied cations with ratios of Bi/Zn=75:25 and Ta/Zn=75:25 in the *A* and *B* sites, respectively. This fractionally occupied BZT solid solution structure has been further modified to obtain ordered or partially ordered solid solution structures as described in our previous report [18, 19].

Although, the CIF for the BZN structure is available in the ICSD, the above BZT structure has been used as an initial structure in this work, including for BZN, in order to have a consistent set for comparison. Furthermore, the CIF for BZN (JCPDS PDF, 04-016-3002) actually represents the $Bi_{1.5}Zn_{0.92}Nb_{1.5}O_{6.92}$ composition, rather than $Bi_{1.5}ZnM_{1.5}O_7$. The CIFs for $Bi_{1.5}CdM_{1.5}O_7$ (M = Nb, Ta) have not been found in the ICSD; thus, appropriate replacement of Zn cations by Cd cations has been carried out in the BZT ordered and partially ordered solid solution structures.

RESULTS AND DISCUSSION

Experimental Results

XRD patterns obtained from BCdN and BCdT powders are shown in Figure 5-1. XRD patterns of BZN and BZT compounds, which have been reported in our previous work [18, 19], are also shown for comparison, since CIF for BCdN and BCdT are not in the ICSD.
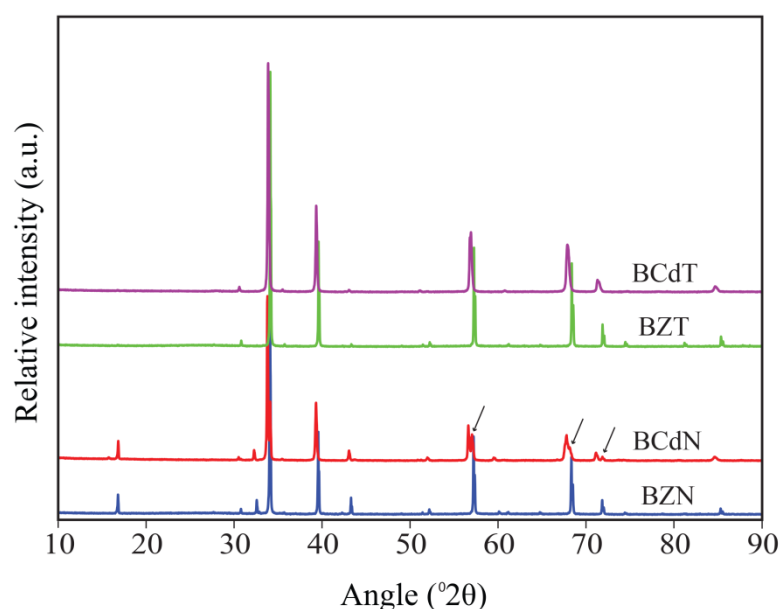
Figure 5-1: XRD patterns of $Bi_{1.5}MM'_{1.5}O_7$ (M = Zn, Cd; M' = Nb, Ta) powders

(Arrows emphasize splitting of peaks)

The graphs show that the main peaks of the BCdN and BCdT patterns are very close to those of BZN and BZT, respectively. Only slight shifts in the peak positions to the lower angles have been observed when compared to those of BZN and BZT patterns, respectively. This indicates that the crystal structures of BCdN and BCdT are closely related to those of BZN and BZT, respectively, thus they could also correspond to cubic structures. However, peaks at higher angles in BCdT and BZN patterns show

broadening and splitting (shown by arrows), respectively which are indications of slightly distorted cubic structures, probably rhombohedral or orthorhombic structures. Such structural distortion may also be present in XRD patterns of BZN or BZT as slight peak shoulders, difficult to differentiate from potential Kα1 or Kα2 multiple peaks; however, it can be clearly seen when the Cd cation with larger ionic radius than the Zn cation is incorporated in the crystal structures.

The optical absorption curves of the BCdN and BCdT powders are displayed in Figure 5-2, together with those of BZN and BZT powders for comparison. Although, replacement of Ta for Nb substitution induces a blue shift (lower energy), the optical absorptions are obtained at wavelengths about 350 - 400 nm in the UV light region and are similar for corresponding Zn $3d$ and Cd $4d$ compounds. The band gap values estimated from the UV-Vis diffuse spectra are about 2.85 and 3.05 eV for the BCdN and BCdT compounds, respectively.
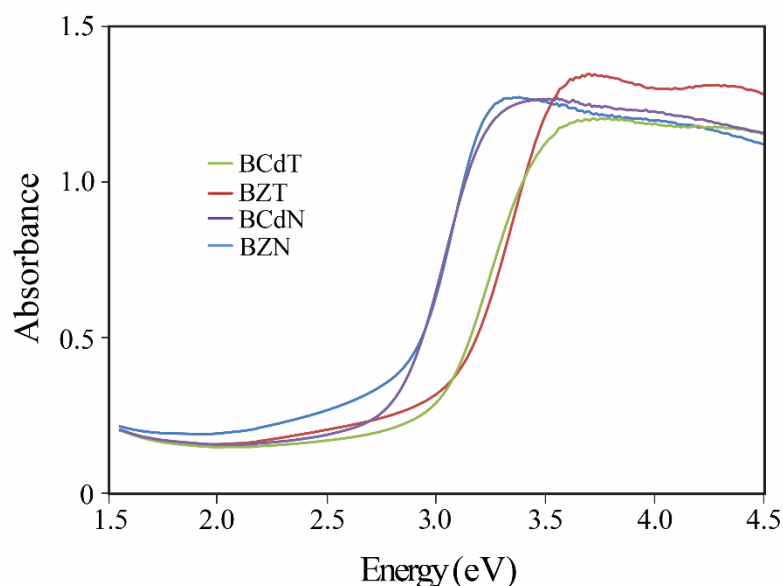
Figure 5-2: Optical absorption edges of $Bi_{1.5}MM'_{1.5}O_7$ (M = Zn, Cd; M' = Nb, Ta) powders

Electronic Structure Calculations

The band structures for the BCdT compound treated as random, ordered and partially ordered solid solutions are shown in Figure 5-3(a, b and c), respectively. When the structures are assumed to be random solid solutions, with fractional occupation of the substituted metal atom positions, as prescribed in the available CIF from the ICSD, the calculated electronic bands do not display any gaps as shown in Figure 5-3(a). This situation changes when the substitutions are assumed to occur at preferential, specific sites in the structures as ordered or partially ordered solid solutions, respectively. This is consistent with previously reported and discussed results for BZN and BZT compounds [18, 19].
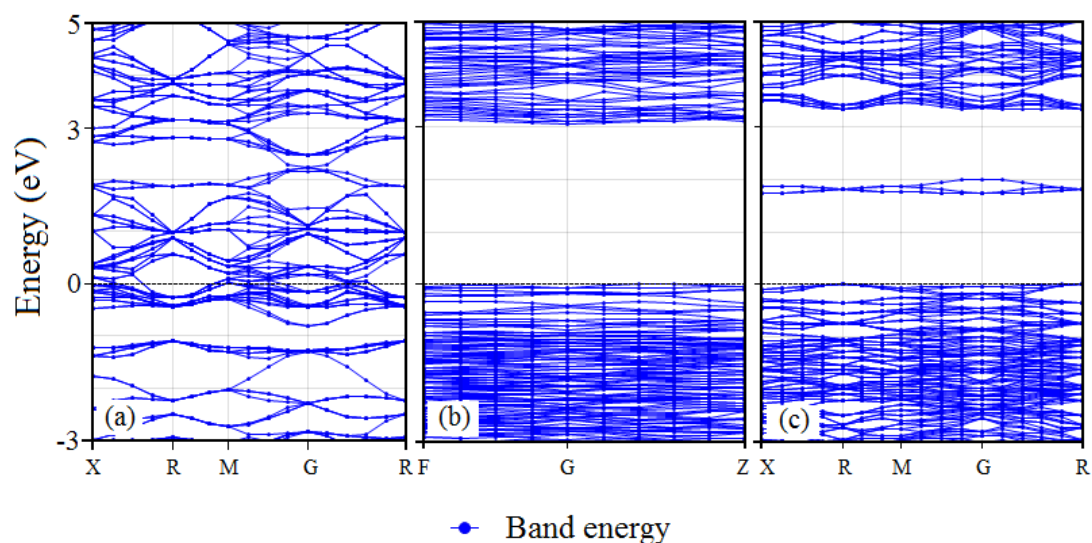
Figure 5-3: The band structures for BCdT (a) random (b) ordered and (c) partially ordered solid solutions

Figure 5-3(b and c) display the electronic band structures for the BCdT ordered and partially ordered solid solution structures. It can be seen that the modified structures provide clear gaps between the VB and CB. The calculated band gap value for the ordered structure is 3.06 eV, which is in excellent agreement with the experimentally

estimated band gap value of 3.05 eV. However, a few localized impurity bands, can also be observed in the forbidden gap of the BCdT partially ordered solid solution as shown in Figure 5-3(c). These localized bands are probably split from the main CB bands and downshifted to the lower energy level by the effect of fractional occupancy of mixed Bi/Cd cations in the *A* site of the structure.

The partial DOS curves for BCdT partially ordered solid solution, contributed by individual atoms, in Figure 5-4 shows that these localized bands are the mixture of Ta *5d* and O *2p* orbitals. Therefore, the DFT calculated band gap values are very consistent for both ordered (~ 3.07 eV) and partially ordered (~ 3.07 eV) BCdT solid solutions and with the experimental optical band gap (~ 3.05 eV). With respect to the contribution of Cd to the electronic band structure, a pronounced peak of *4d* states is obtained at about -8.0 eV, which does not participate directly in the definition of the band gap energy; however, it may exert an indirect influence.
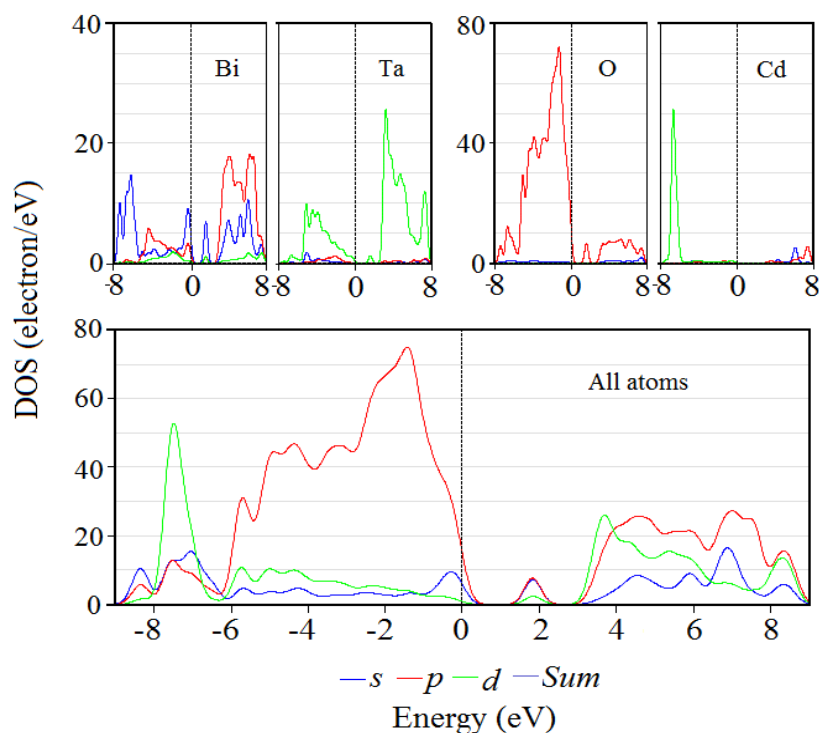

Figure 5-4: The DOS for BCdT partially ordered solid solutions

Table 5-1 (ordered solid solutions) and Table 5-2 (partially ordered solid solutions) summarize the comparison between both theoretically calculated and experimentally estimated band gap values for all above-mentioned compounds. After geometry optimization, the final structures for the ordered solid solutions obtained are slightly distorted cubic, where rhombohedral structures have been formed. However, the final structures for the partially ordered solid solutions are found to remain cubic. Lattice parameters for the ordered solid solutions are slightly smaller than the other structures, while enthalpy obtained from the ordered solid solutions are slightly lower than the partially ordered solid solution structures for both Zn and Cd compounds.

Table 5-1: Comparison of theoretical and experimental band gap results for

$Bi_{1.5}MM'_{1.5}O_7$ (M = Zn, Cd; M' = Nb, Ta) ordered solid solutions

Structure*	Lattice parameter (Å)	Lattice angle (Å)	Enthalpy (eV)	DFT band gap (eV)	Experimental band gap (eV)
BZT	10.42	90.12	-58449.02	3.12	3.08
BZN	10.76	90.11	-58427.47	1.76	2.85
BCdT	10.52	90.24	-57570.16	3.06	3.05
BCdN	10.86	90.33	-57590.19	1.73	2.85

* Rhombohedral (slightly distorted from the input cubic structure) are obtained.

Table 5-2: Comparison of theoretical and experimental band gap results for

$Bi_{1.5}MM'_{1.5}O_7$ (M = Zn, Cd; M' = Nb, Ta) partially ordered solid solutions

Structure*	Lattice parameter (Å)	Lattice angle (Å)	Enthalpy (eV)	DFT band gap (eV)	Experimental band gap (eV)
BZT	10.44	90.00	-58228.60	3.23 (3.50)	3.08
BZN	10.82	90.00	-58209.30	2.02 (2.25)	2.85
BCdT	10.53	90.00	-57381.29	3.07 (3.34)	3.05
BCdN	10.89	90.00	-57363.54	1.82 (2.00)	2.85

*Cubic are obtained after calculations.

Substituting Ta (0.68 Å) for Nb (0.69 Å) cations in the *B* site of the crystal structure results in smaller band gap values, while maintaining the general features for the band structure. This result is due to a small downshift of the CB levels from the slight differences between energy levels of Nb 4*d* in NbO_6 and Ta 5*d* in TaO_6 coordination environments, respectively. This band gap size reduction, when Ta is replaced for Nb, can be seen in both Cd and Zn metal cases. The DFT calculated and the UV-Vis estimated band gaps are in good agreement for Ta 5*d* containing BCdT and BZT compounds. However, the calculated band gaps are smaller than the experimentally estimated band gaps for the BCdN and BZN structures. Differences in enthalpy appear to indicate that Zn containing compounds are more stable than Cd containing compounds.

When comparing the effects of different transition metal substitutions on the band gaps, the Cd 4*d*-orbitals and Zn 3*d*-orbitals induce only minor differences in both the experimental and theoretical band gap values. Zn and Cd have different ionic radii, 0.74 Å and 0.95 Å, respectively, which seems to account for the different DFT calculated lattice parameters in Table 5-1 and Table 5-2; however, this has not been sufficient to introduce more significant band gap changes. A similar trend has been reported in electronic band gap investigations of $Bi_2MNb_2O_7$ (M = Al, Ga, In) structures [20], which also belong to the same column or group of elements in the periodic table.

CONCLUSIONS

BCdM (M = Nb, Ta) powders with the pyrochlore structure have been successfully synthesized using solid-state reaction and characterized by powder diffraction technique. XRD patterns of BCdM (M = Nb, Ta) show peak broadening and splitting consistent with indications of small distortions from cubic structures. Existence of such distortions has been suggested by our previous DFT analyses of this family of compounds, in order to obtain electronic band gaps, which otherwise do not exist. Such crystal structure distortion may be further investigated using other techniques, such as transmission electron microscopy (TEM) or neutron and synchrotron XRD. The optical absorption properties for BCdM (M = Nb, Ta) powders have been measured and their band gap values have been compared with theoretical electronic energy bands, calculated using DFT assuming ordered and partially ordered solid solutions for the Cd substitution. Both theoretical and experimental band gap values for BCdT compound match well; however, the calculated band gap for BCdN is slightly smaller than the estimated result from absorption measurements. This difference in the results for BCdM (M = Nb, Ta) is similar to that observed for BZM (M = Nb, Ta), which have previously been reported [18, 19]. More importantly, consistent results are obtained using identical approaches, which indicates that ordered solid solutions may be a better approximation to the transition metal substitution in this family of Bi_2O_3-based compounds.

REFERENCES

1.   Tseng, T.K., *et al.*, *A review of photocatalysts prepared by sol-gel method for VOCs removal.* International journal of molecular sciences, 2010. **11**(6): p. 2336-2361.

2.   Gamage, J. and Z. Zhang, *Applications of photocatalytic disinfection.* International Journal of Photoenergy, 2010. **2010**(764870): p. 1-11.

3.   Malato, S., *et al.*, *Decontamination and disinfection of water by solar photocatalysis: Recent overview and trends.* Catal. Today, 2009. **147**(1): p. 1-59.

4.   Blanco-Galvez, J., P. Fernandez-Ibanez, and S. Malato-RodrÃguez, *Solar photocatalytic detoxification and disinfection of water: Recent overview.* Journal of solar energy engineering, 2007. **129**(1): p. 4-15.

5.   Al-Rasheed, R.A. *Water treatment by heterogeneous photocatalysis an overview*. 2005.

6.   Zaleska, A., *Doped-TiO$_2$: a review.* Recent Patents on Engineering, 2008. **2**(3): p. 157-164.

7.   Wei, Y.L., K.W. Chen, and H.P. Wang, *Study of chromium modified TiO$_2$ nano catalyst under visible light irradiation.* Journal of nanoscience and nanotechnology, 2010. **10**(8): p. 5456-5460.

8.   Chen, X. and C. Burda, *The electronic origin of the visible-light absorption properties of C-, N-and S-doped TiO$_2$ nanomaterials.* J. Am. Chem. Soc. , 2008. **130**(15): p. 5018-5019.

9.   Fuerte, A., *et al.*, *Visible light-activated nanosized doped-TiO$_2$ photocatalysts.* Chemical Communications, 2001(24): p. 2718-2719.

10.   Yu, H., H. Irie, and K. Hashimoto, *Conduction band energy level control of titanium dioxide: Toward an efficient visible-light-sensitive photocatalyst.* J. Am. Chem. Soc. , 2010. **132**(20): p. 6898-6899.

11.   Kudo, A., K. Omori, and H. Kato, *A novel aqueous process for preparation of crystal form-controlled and highly crystalline BiVO$_4$ powder from layered vanadates at room temperature and its photocatalytic and photophysical properties.* Journal of the American Chemical Society, 1999. **121**(49): p. 11459-11467.

12.   Zou, Z., J. Ye, and H. Arakawa, *Role of R in Bi2RNbO7 (R= Y, rare earth): Effect on band structure and photocatalytic properties.* The Journal of Physical Chemistry B, 2002. **106**(3): p. 517-520.

13. Ropero-Vega, J., *et al.*, *Photophysical and photocatalytic properties of Bi_2MNbO_7 (M= Al, In, Ga, Fe) thin films prepared by dip-coating.* Mater. Sci. Eng., B, 2010. **174**(1): p. 196-199.

14. Li, Y., *et al.*, *Electronic structure and photocatalytic properties of $ABi_2Ta_2O_9$ (A= Ca, Sr, Ba).* Journal of Solid State Chemistry, 2008. **181**(10): p. 2653-2659.

15. Torres-Martinez, L.M., *et al.*, *Bi_2MTaO_7 (M= Al, Fe, Ga, In) photocatalyst for organic compounds degradation under UV and visible light.* WSeAS Trans environ dev, 2010. **6**: p. 286-295.

16. Tian, M., W. Shangguan, and W. Tao, *The photocatalytical activities for water decomposition of $K_4R_2M_{10}O_{30}$ (R= Y, La, Ce, Nd, Sm; M= Ta, Nb) and their photophysical properties based on the first principle calculation.* Journal of molecular catalysis A: chemical, 2012. **352**: p. 95-101.

17. Zou, Z., *et al.*, *Photocatalytic and photophysical properties of a novel series of solid photocatalysts, $BiTa_{1-x}Nb_xO_4$ (0< x<1).* Chem. Phys. Lett. , 2001. **343**(3): p. 303-308.

18. Perenlei, G., *et al.*, *Electronic structure studies and photocatalytic properties of cubic $Bi_{1.5}ZnNb_{1.5}O_7$.* International Journal of Photoenergy, 2015. **2015**(575376): p. 1-11.

19. Perenlei, G., *et al.*, *Synthesis, characterization and electronic structure studies of cubic $Bi_{1.5}ZnTa_{1.5}O_7$ for photocatalytic applications.* International Journal of Photoenergy, 2015. **2015**(349030): p. 1-8.

20. Zou, Z., J. Ye, and H. Arakawa, *Preparation, structural and optical properties of a new class of compounds, Bi_2MNbO_7 (M= Al, Ga, In).* Mater. Sci. Eng., B, 2001. **79**(1): p. 83-85.

5.3 ARTICLE 5: ''BAND GAP ENGINEERING OF Bi$_{1.5}$MM'$_{1.5}$O$_7$ (M= Zn, Cu, Ni, Co; M'=Ta, Nb, V) COMPOUNDS''

Ganchimeg Perenlei,[1] Jose A. Alarco,[1,2] Peter C. Talbot[1,2] and Wayde N. Martens[1]

[1]*School of Chemical, Physics and Mechanical Engineering, Science and Engineering Faculty,* [2]*Institute for Future Environments, Queensland University of Technology, Brisbane, QLD 4000, Australia*

ABSTRACT

Systematic trends in the optical properties and electronic band structures of Bi$_{1.5}$MM'$_{1.5}$O$_7$ (M = Zn, Cu, Ni, Co; M' = Ta, Nb, V) compounds have been investigated using optical absorption measurements and first principle DFT calculations. The effect of substitutions on the electronic band structures has been a main focus of this work in order to modify wide-band gap photocatalysts (active in the UV region) to narrow their band gaps and make them active under visible light irradiation. The BZT structure with formula Bi$_{1.5}$ZnTa$_{1.5}$O$_7$ has been used as the initial compound. Selected metals with similar ionic radii have then been substituted for Zn and Ta. Optical absorption data has been used as criteria to establish the more reliable theoretical band structure determinations. Structural properties that lead to good agreement between experimental band gaps and calculations of the electronic band structures have been identified. These observations may guide further modification and optimization of this family of Bi$_2$O$_3$-based photocatalysts.

INTRODUCTION

Effective solar energy utilization is highly desirable for the sustainable application of heterogeneous photocatalysis. This has prompted an intensive search for low-energy-responsive photocatalysts, which is active in visible light irradiation, which has increased significantly in the recent literature [1]. Among the most common approaches to achieve this objective are making solid solutions or doping with other elements already existing wide-band gap semiconductor materials [2, 3].

The selection of proper dopants/substituents is challenging because foreign elements can cause defects in the crystal structure, introduce impurity bands in the electronic band structure of the host material and consequently decrease the photocatalytic activity [4, 5]. Nevertheless, previous attempts to modify the electronic band structure of known semiconductors, such as TiO_2, using dopants have often focused on reducing their band gaps by raising the valence band (VB) level to higher energy levels [6-8]. Various non-metals, such as N, S, C, P, B, I or F, have commonly been used as dopants for oxide materials due to their higher energy levels than O $2p$ orbitals [6-10].

Similar modification of the electronic band structure of oxide semiconductors has also been achieved using a wide range of transition metals as dopants [11-13]. A number of reports on TiO_2 doped with transition metals (TM), such as Zn, Cu, Ni, Co, Fe, Mn, Cr, V, Nb, Ta, Mo, W, Ru, Ag, Au or Pt, have been published in the literature [2, 3, 11, 14]. However, TM dopants suffer from several drawbacks and there are controversial views about them [5, 15]. Some reports suggest that photocatalysts doped with high concentration of TM perform with poor activity because the dopants form impurity bands in the band gap and act as traps for electron

and holes, resulting in low charge-carrier mobility. Based on correlations between dopant concentration and density of states, a low concentration of dopants (up to 20 %) has been recommended [13].

Most of the above-mentioned observations and recommendations have been experimentally determined and driven; however, systematic theoretical analyses on the effect of TM substitutions on the electronic band structure are scarce in the literature. Electronic band structure analyses using density functional theory (DFT) calculations of many complex materials containing $3d$, $4d$ or $5d$-metals usually require more advanced, sophisticated DFT approaches to deal with the strong correlations/localization of the main d-electron orbital configurations [4]. The electronic band structure calculations of many crystal structures containing d-orbitals, using standard DFT have therefore been considered as unreliable and have remained largely unexplained [16].

Recent studies suggest that co-doping is more effective than mono-doping for the modification of electronic structures to design visible-light photocatalysts [12, 15, 17]. Simultaneous doping/substitutions of pairs of atoms (metal, non-metal, or both) as donor-acceptor combinations have been introduced in two sites of the crystal structure of host materials [10, 18]. It has been assumed that these combinations may lead to reduction of both the VB and conduction band (CB) levels to meet suitable band gap criteria in new types of photocatalysts and achieve high optical absorption and high charge-carrier mobility [11].

Bi-based oxide semiconductors (and also In, Sn, Ag-based oxides) that contain $6s^2$ electronic configurations or lone pairs in the VB have been investigated as potential materials for electronic band structure modification. In these materials, the valence

band energy level of hybridized M 6s with O 2p are slightly higher than that of pure O 2p orbitals, which may allow for hybridization of s, p and d-orbitals from additional elemental substitutions [19, 20].

In this work, bismuth zinc tantalum oxide (BZT) that contains Zn cations in both the A (Bi) and B (Ta) sites of the crystal structure has been selected for the systematic investigation of electronic band structure modifications. In the literature, BZT has been experimentally synthesized, well characterized and partially substituted with a wide range of metals that targeted specific properties of interest not including photocatalysis [21-26]. We have substituted Zn and Ta cations of the BZT structure with a series of TM: $Bi_{1.5}MM'_{1.5}O_7$ (M = Zn, Cu, Ni, Co; M' = Ta, Nb, V) to investigate the effects of these substitutions on the optical properties and electronic band structures with photocatalytic applications in mind.

In addition, it is also well known that standard LDA and GGA approximations are not very accurate for the determination of electronic band gaps for a majority of semiconductor materials [16]. This work also addresses the question why random, fractionally occupied, cubic solid solutions produce no band gaps in the DFT calculated electronic band structures. We have previously found that the random solid solution, cubic structure may be hiding subtle structural distortions, which when allowed to exist, produce improved band gap results for BZN and BZT [27, 28]. This work investigates additional $Bi_{1.5}MM'_{1.5}O_7$ examples, where the assumption of slightly distorted cubic structures consistently leads to improved match between experimental band gaps from optical absorption measurements and DFT calculated band gaps.

EXPERIMENTAL SECTION

Material Preparation

All starting materials used in the experiments are of analytical grade ($\geq$ 99.9%), purchased from Aldrich (Australia), and have been mixed and reacted in the required stoichiometric ratio to prepare $Bi_{1.5}MM'_{1.5}O_7$ (M = Zn, Cu, Ni, Co; M' = Ta, Nb, V). Bismuth oxide (Bi_2O_3), niobium oxide (Nb_2O_5), tantalum oxide (Ta_2O_5), vanadium oxide (V_2O_5), zinc oxide (ZnO), copper nitrate tetrahydrate ($Cu(NO_3)_2\bullet4H_2O$), nickel sulfate hexahydrate ($NiSO_4\bullet6H_2O$) and cobalt nitrate hexahydrate ($Co(NO_3)_2\bullet6H_2O$) have been used as starting reagents. A solid-state reaction technique has been employed for the preparation of samples at 1000 °C for 5 h of sintering duration.

Material Characterization

The crystal structures of the synthesized powders have been characterized using X-ray diffraction (XRD). The diffraction patterns have been collected in Bragg-Brentano geometry in the range 5.0 - 90 °2θ on a spun stage using a Philips PANalytical X'Pert PRO X-Ray Diffractometer. The incident X-rays have been produced from a PW3373/00 Co X-ray tube operating at 40 kV and 40 mA, providing Kα1 wavelength of 1.7903 Å. The optical properties of the powders have been characterized by Ultraviolet-Visible (UV-Vis) spectroscopy. The optical absorption spectra have been recorded in the wavelength regions of 200 - 800 nm using a UV-Vis-NIR Cary 5000 Stheno spectrometer.

THEORETICAL CALCULATIONS

Density Functional Theory (DFT), as implemented in the Cambridge Serial Total Energy Package (CASTEP) of Materials Studio 8.0, has been used in the electronic band structure and density of states (DOS) calculations. All structures have been optimized for geometry and cell parameters. The generalized gradient approximation with Perdew-Burke-Ernzerhof (GGA-PBE) functional and norm-conserving pseudopotentials has been adopted along with 100 empty orbitals, non-metal, non-spin and customized convergence tolerance setups as mentioned in our previous reports [27, 28].

The *Crystallographic Information File* (CIF) for the BZT structure (JCPDS PDF, 04-013-6484) from the Inorganic Crystal Structure Database (ICSD) has been used as the initial structure for all DFT calculations, after appropriate substitutions. The starting structure contains fractionally occupied cations with ratios of Bi/Zn=75:25 and Ta/Zn=75:25 in the *A* and *B* sites, respectively. This fractionally occupied BZT solid solution structure has been further modified to obtain ordered or partially ordered solid solution structures, respectively, assuming the Zn substitutions are at specific sites in the structure, which introduces new periodicities as described in our previous reports [27, 28]. For some metal choices, the CIF has not been found in the ICSD. In those cases, appropriate replacements of Zn cations have been carried out. Zn cations have been changed to Cu, Ni or Co cation, while Ta cations to Nb or V cations, respectively.

RESULTS AND DISCUSSION

Experimental Analysis

XRD patterns of $Bi_{1.5}MM'_{1.5}O_7$ (M = Zn, Cu, Ni, Co; M' = Ta, Nb, V) compounds are shown in Figure 5-5. The main XRD peaks of the Ta series (BZT, BCuT, BNiT and BCoT) and the Nb series (BZN, BCuN, BNiN and BCoN) are well-matched with the peak patterns of space group of *Fd-3m* in the ICSD database (Figure 5-5(a, b)). For example, the main diffraction peaks of BZT are indexed to $Bi_{1.5}ZnTa_{1.5}O_7$ (JCPDS PDF, 04-013-6484), while the peaks of BCuN are matched with $Bi_{1.5}CuNb_{1.5}O_7$ (JCPDS PDF, 00-056-0999), respectively. This is an indication that cubic structures have been successfully prepared. Most of the diffraction peaks in the XRD patterns of Ta and Nb compounds correspond to fairly pure phases. In the XRD patterns for BCoT compound, however, some impurity peaks are observed (Figure 5-5(a)).

In contrast, the peak positions of all the compounds in the V series (BZV, BCuV, BNiV and BCoV) correspond to orthorhombic structures; however, they do not match with any patterns in the ICSD database. Figure 5-5(c) shows that the overall peak patterns for all compounds look similar. Peak position and peak intensities of the BZV and BCoV compounds are very similar to each other; but, some peak positions in the patterns of BCuV and BNiV compounds show slight shifts to the lower angles when compared to those of BZV and BCoV compounds.
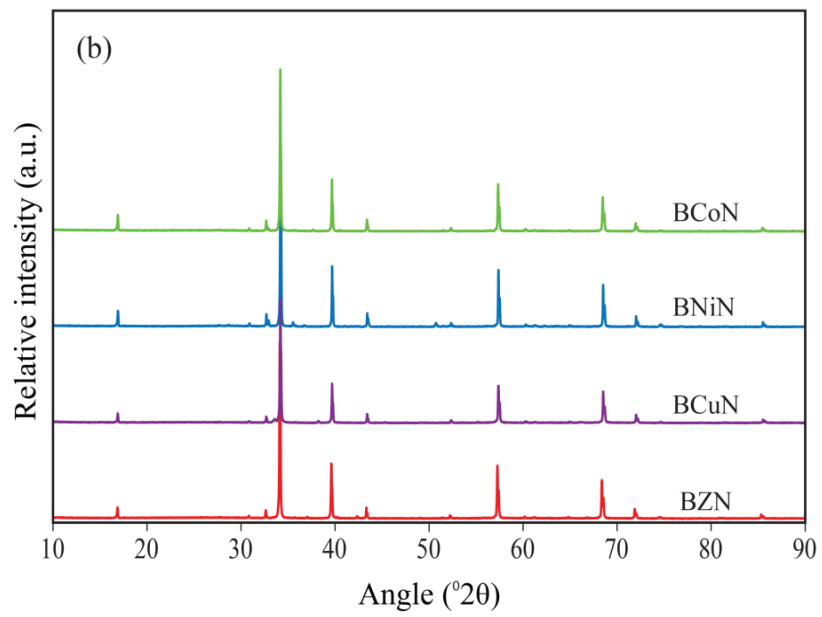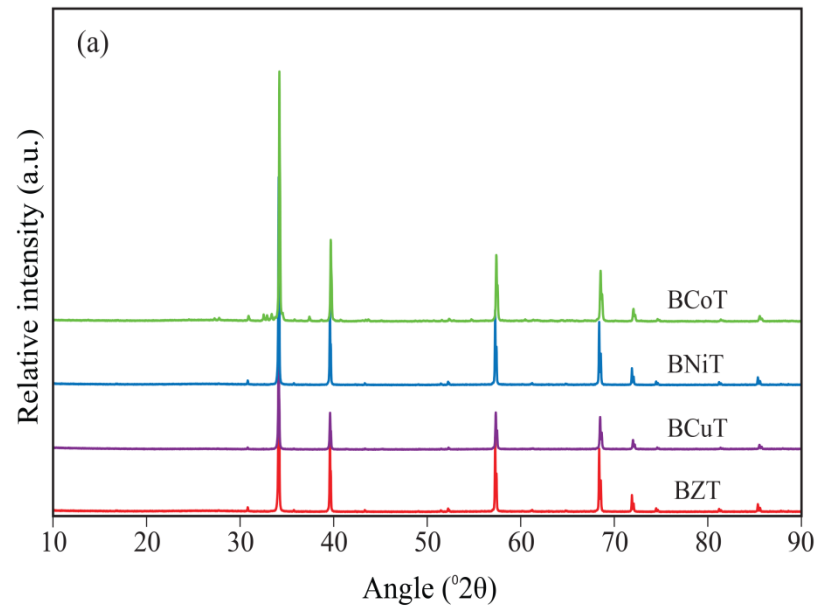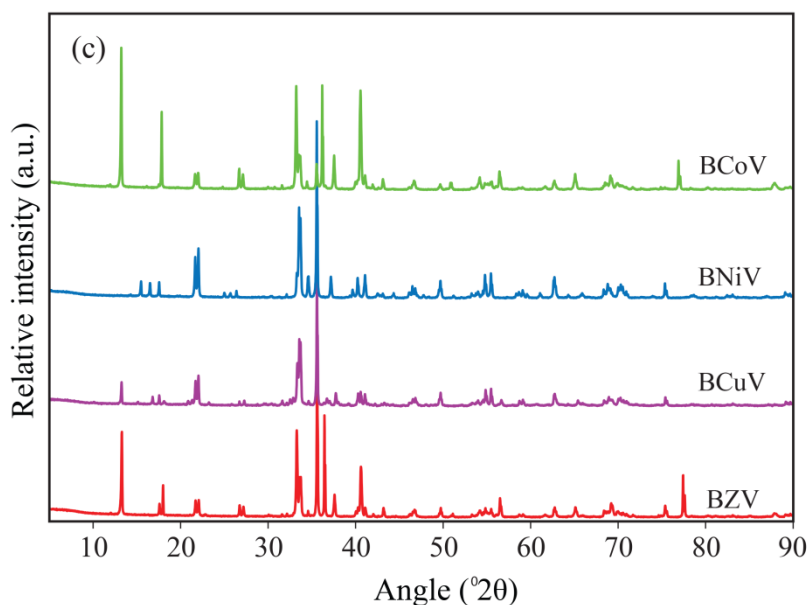
Figure 5-5: XRD patterns for (a) BMT (b) BMN and (c) BMV (M = Zn, Cu, Ni, Co)

The optical absorption results for most of the compounds are shown in Figure 5-6. As reported in our previous works, BZT and BZN show optical absorption in the UV light region [27, 28]; however, BZV presents a blue shift towards the visible light region, which can be seen in Figure 5-6(a). The measured band gaps are estimated to be about 3.05, 2.85 and 2.1 eV for BZT, BZN and BZV powders, respectively.

Similar trends are also observed for the Ni compounds as shown in Figure 5-6(b). Absorption edge shifts to the visible light region are obtained for BNiV and several sets of absorption edges observed for the pure BNiT and BNiN become reduced or completely removed. The difference between absorption curves for the Cu and Co compounds, such as BCuM and BCoM (M = Ta, Nb, V), are very minor. V containing compounds (curves are not shown in the Figure 5-6) do not show any significant blue shifts compared to Nb and Ta compounds.

If we compare the effect of 3*d*-transition metals in the optical absorption properties of the compounds, desirable lower energy (blue shift) absorption edges have been achieved with substitutions of Cu, Ni and Co metals into the BZT and BZN crystal structures. Among them, the optical absorption edges of BCuT and BCuN compounds have shown potential to be active in the visible light region.
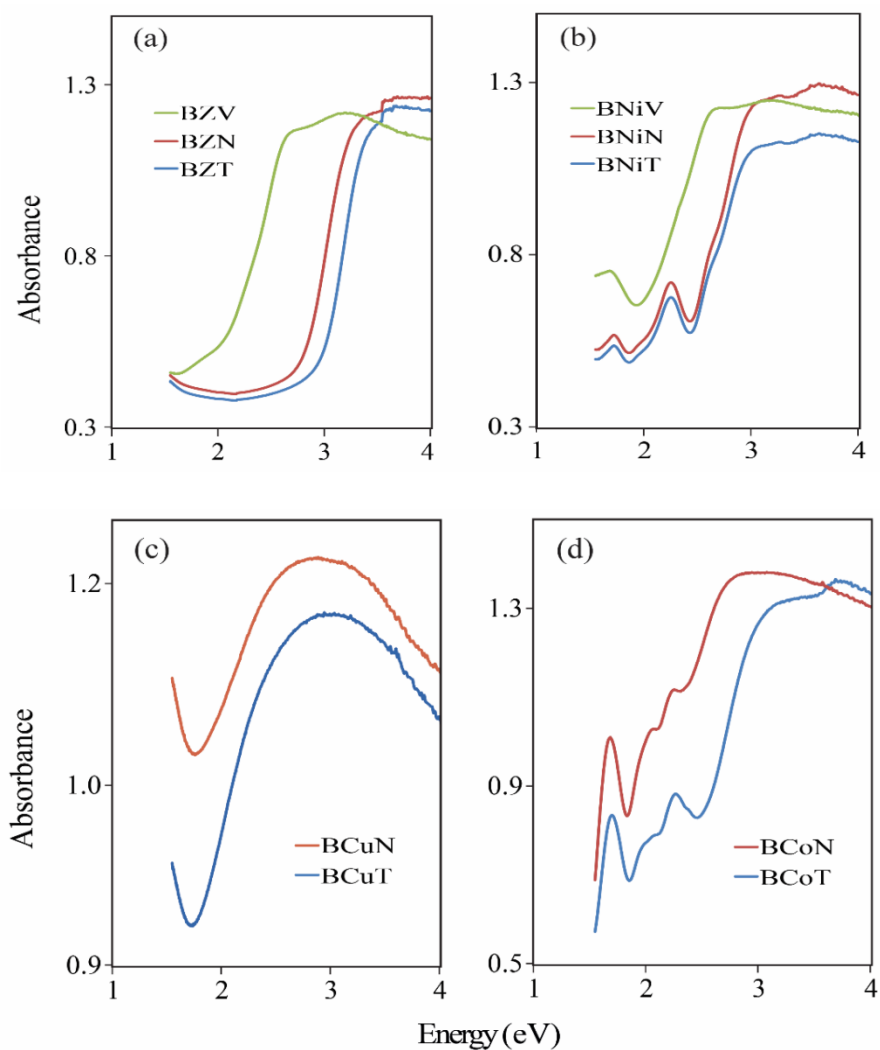

Figure 5-6: Optical absorption curves for $Bi_{1.5}MM'_{1.5}O_7$ (M = Zn, Cu, Ni, Co; M' = Ta, Nb, V) powders

Electronic Structure Calculations

Various combinations of $Bi_{1.5}MM'_{1.5}O_7$ (M = Cu, Ni, Co; M' = Ta, Nb, V) compounds have been systematically investigated using DFT calculations in order to identify materials with suitable electronic band structures. Structures of above mentioned compounds have been treated as random, ordered and partially ordered solid solutions as described in our previous reports [27, 28]. The absence of band gap obtained in the calculations using random solid solution structures for all the combinations mentioned above. However, the calculations on both ordered and partially ordered solution structures, present gaps in the electronic band structures. Structures containing a combination of both random and ordered cation substitutions in the *A* and *B* sites, respectively, have been considered as partially ordered solid solutions in the DFT calculations. It is because fractional occupancy of cation substitutions in the *B* site of the structures mainly controls the formation of energy gap.

Electronic band structures for BZT, BZN and BZV ordered solid solutions are shown in Figure 5-7. In the BZT structure, the top of the VB is predominantly composed of hybridized O $2p$ + Bi $6p$ + Bi $6s$ orbitals, while the bottom of the CB is mainly formed by the mixture of Ta $5d$ + O $2p$ orbitals [28]. Thus, it is expected to downshifts the CB level with the substitutions of Nb or V cations instead of Ta in the BZT structures. It can be seen that the band gaps of the compounds become narrower with the decrease in principal quantum number *n* of the *d* orbitals.

The band gaps are calculated to be about 3.12, 1.76 and 1.62 eV for BZT, BZN and BZV, respectively. Thus, substituting Ta (*5d*) by Nb (*4d*) or V (*3d*) in the *B* site of the BZT crystal structure reduces the band gap by a downshift of the CB level due to lower energy level of Nb *4d* in NbO_6 or V *3d* in VO_6 orbitals than Ta *5d* in TaO_6 orbitals. Also, calculated lattice parameters for the final structures are slightly different due to the slight differences in the ionic radii of the cations: Ta (0.68 Å), Nb (0.69 Å) or V (0.59 Å).

The above trend and effects in the electronic band structure observed for Zn cations is also observed in the case for Cu cations. The DFT calculations on ordered solid solutions of BCuM (M = Ta, Nb, V) show consistent band gap reductions. The calculated band gaps are about 2.65, 1.52 and 1.1 eV for BCuT, BCuN and BCuV, respectively, from the band structures shown in Figure 5-8.
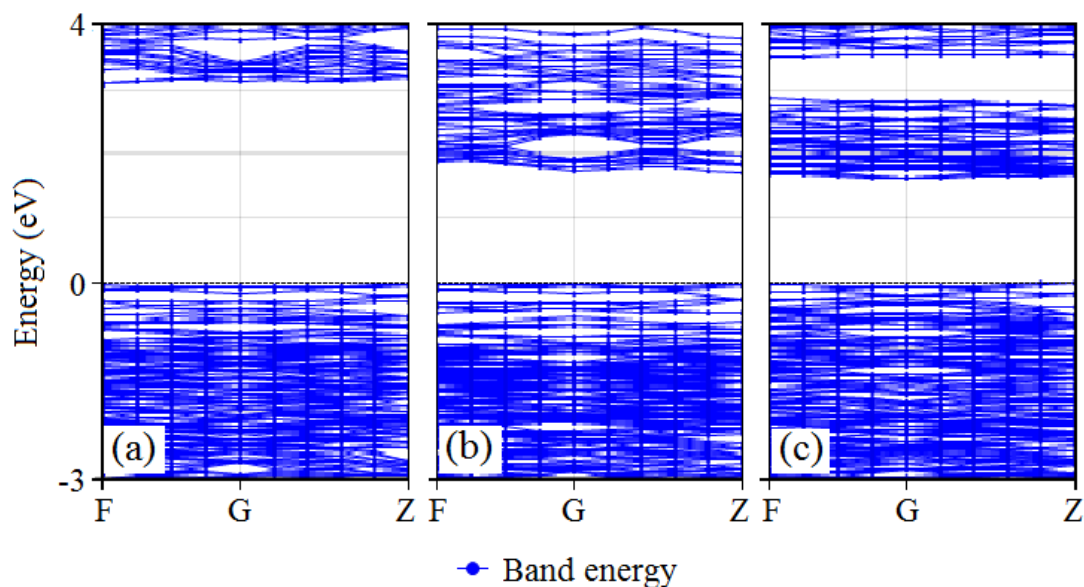

Figure 5-7: Band structure for (a) BZT (b) BZN and (c) BZV ordered solid solution

The band gap reduction in the V-containing structures does not reflect the results obtained from the optical absorption data in the cases of both BZV and BCuV compounds. Moreover, in their band structures, secondary band separations have been found in the CB levels, which are different that the Ta and Nb containing band structures. These observations also have been found from the calculated band diagrams of the same structures with other cation substitutions, indicating that BMV (M = Zn, Cu, Ni, Co) probably does not exist as a cubic structure, and this is confirmed by the XRD analysis on the powders.
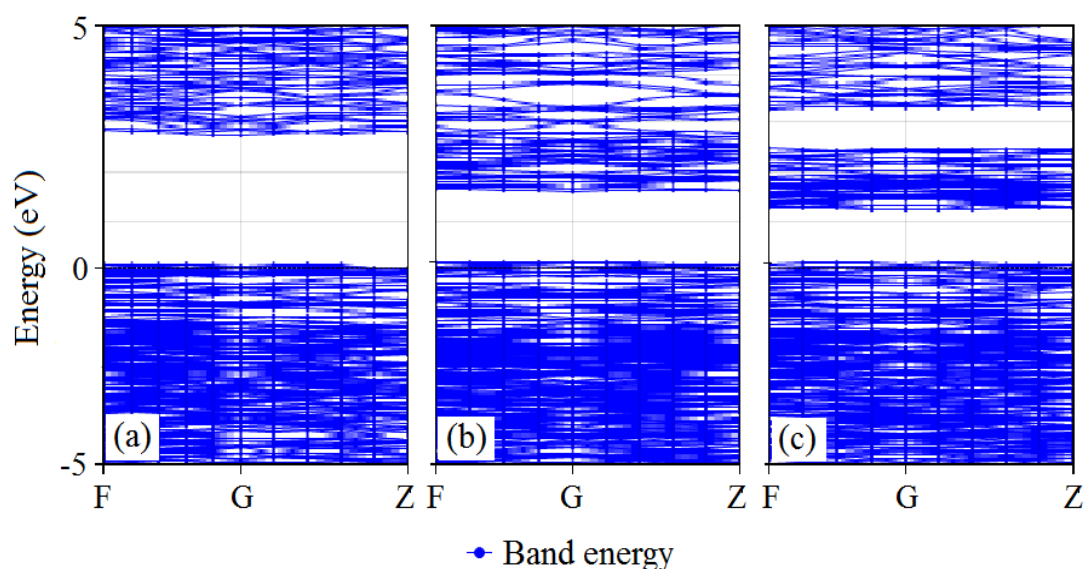
Figure 5-8: Band structure for (a) BCuT (b) BCuN and (c) BCuV ordered

solid solution

Although, these calculated band gap values are slightly different than the experimental values for the above compounds, the overall band gap reduction trend in the Ta, Nb, V order is consistent in both Zn and Cu substituted structures. However, in the cases for Ni or Co substitutions, DFT calculations on the ordered solid solution structures do not converge. Therefore, the structures of the partial solid

solution, which have been completely calculated for all the cation substituted cases, have been considered in the calculations.

Comparison of band structures for the BMT (M= Zn, Cu, Ni, Co) partially ordered solid solutions are shown in the Figure 5-9. The electronic band structures for partially and fully ordered solid solutions of BZT and BCuT are very similar. The only difference is a few localized impurity bands in ''the forbidden gap'' as shown in Figure 5-9, which are separated from the main bands in the CB level and downshifted due to the effect of random solid solution in the *A* site of the structures. That is why the partially ordered structures have shown slightly larger energy gap values than those of the ordered structures; however, the overall features of electronic structures for the ordered and partially ordered solid solutions are practically similar. The ordered solid solution structures have a rhombohedral structure, while the partial solid solution structures have a cubic one.

Several additional optical absorptions edges observed in the UV-Vis spectra for the BNiT and BCoT compounds have also been obtained in the electronic band structures calculated using DFT for partially ordered solid solutions, indicating the electrons can be excited from several sets of occupied orbitals in the VB level. These observations also apply to experimental and calculated electronic band structures for ordered solid solutions (not shown in the graph) and other Ni and Co containing compounds, which are very similar. Although the DFT calculated band gaps are slightly smaller than the experimentally obtained band gap results, the general trend displaying reduction of the band gap with different metal substitution is obvious.
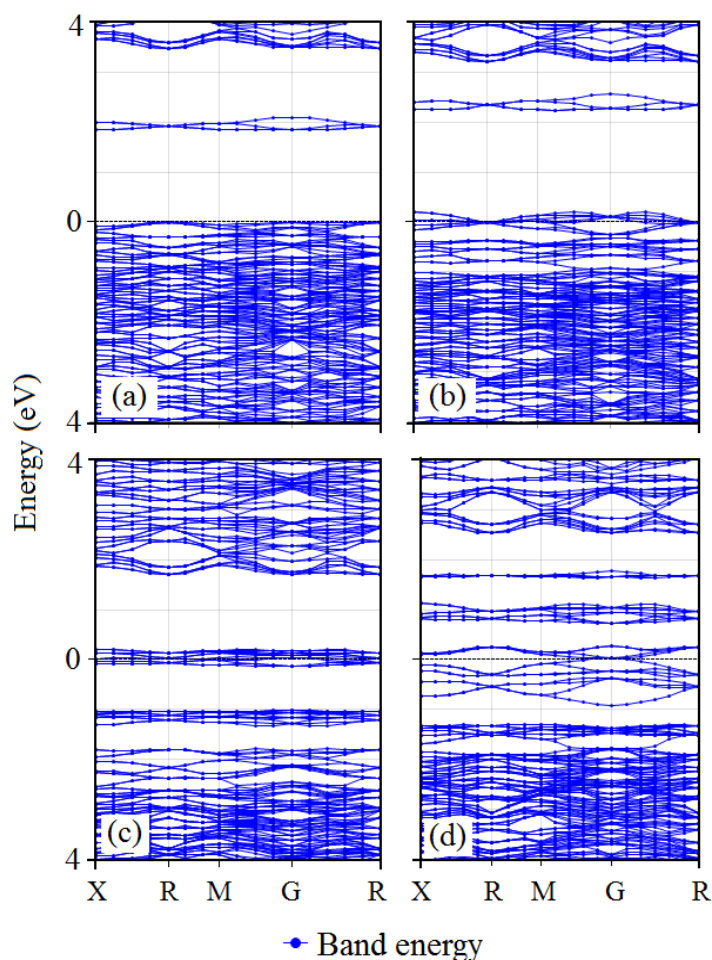
Figure 5-9: Band structures for (a) BZT (b) BCuT (c) BNiT and (d) BCoT partially

ordered solid solutions

Similarly, substitution of *3d*-transition metals with higher energy level instead of Zn

metals in the both *A* and *B* sites of the BZT crystal structure results in narrower band

gaps. In particular, a rise of the VB level is observed. However, the results vary

depending on the nature of the electronic configuration of the dopant metals.

Increased hybridization with different orbitals appears to contribute to the DOS.

Figure 5-10 shows the total and partial DOS for various transition metals (Cu, Ni,

Co) in substituted BZT compounds, including BCuT, BNiT and BCoT ordered solid

solution structures.

The calculated band gaps are about 3.12, 2.65, 1.43 and 1.0 eV for the BZT, BCuT, BNiT and BCoT, respectively. The band gap of BZT is the largest of all and it is reduced in the following order of the substitutions: Zn 3*d*, Cu 3*d*, Ni 3*d* and Co 3*d*, which follows the atomic number/relative position in the periodic table. A sharp peak of Zn 3*d* is present at relatively low energy of -7 eV as shown in Figure 5-10(a). Thus the contribution of these low energy 3*d*-orbitals in the determination of the band gap does not seem to be very significant.

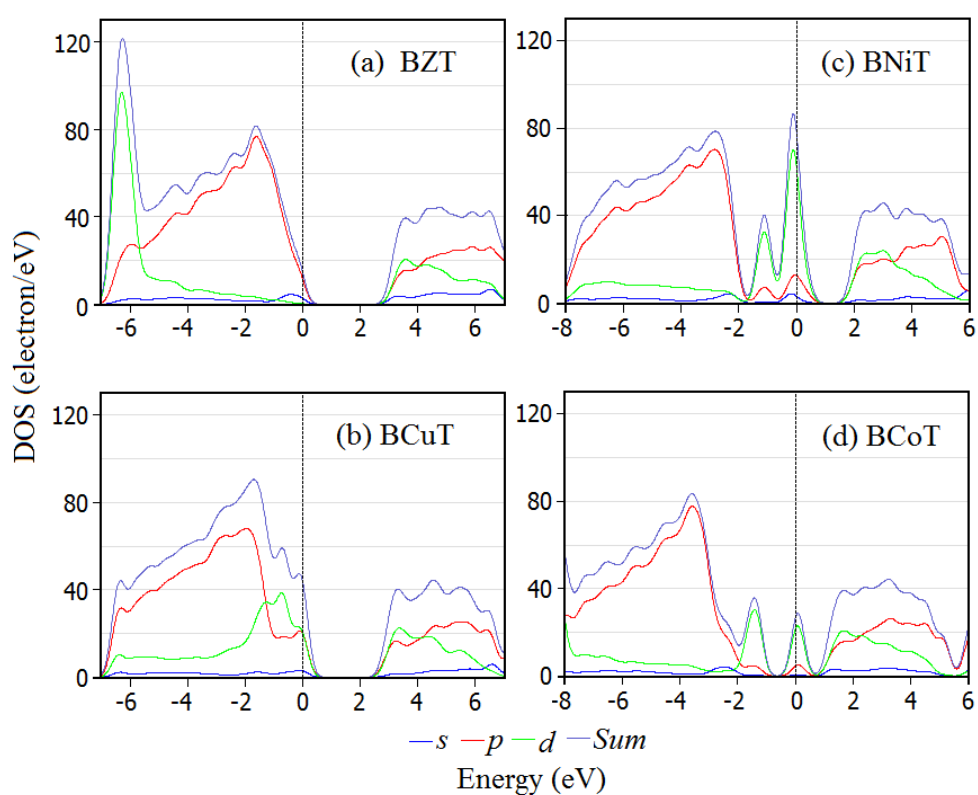**Figure 5-10:** Total and partial DOS for (a) BZT, (b) BCuT, (c) BNiT and (d) BCoT ordered solid solution structures

In the case of other metal substitutions, additional bands appear at the top of the VB, and this has influence on the size of the band gap. In these cases, partially occupied $3d$-orbitals become involved in hybridization with O $2p$ and Bi $6s$ orbitals. The DFT calculation results show that the rise of VB due to the $3d$ orbital contribution is relative to BZT for substitutions of Cu and Ni cations, but not for Co cations. An explanation is that the number of electrons decreases (Cu $3d^9$, Ni $3d^8$ and Co $3d^7$), the positive nuclear charge increases and the energy levels shift [13]. This observation clearly applies to the electronic band structure of BCuT as can be seen in Figure 5-10(b); however, the band gap reduction is relatively small due the only contribution to its reduction is a rise of VB level, without an accompanying lowering of the CB level.

In the band gap of octahedral crystals, $3d$-orbitals split into two states: the lower energy t_{2g} states and the higher energy e_g states [13]. It is likely that the lower energy state of $3d$-orbitals interact with the hybridized Bi $6p$, O $2p$ or Bi $6s$ states in the VB level, while the higher energy state can influence the CB level by driving Ta $5d$ states to the lower energies. Thus, the band gap of BNiT becomes narrower, is almost half that of BZT as can be seen in Figure 5-10(c). Depending on the nature of orbitals, the newly formed energy bands can also end up separated from the main bands as localized impurity bands in the forbidden gap, which weakens the photocatalytic activity of the materials. This phenomenon clearly appears in the case BCoT as can be seen in Figure 5-10(d). Because BNiT and BCoT show splitting of the VB, the BCuT has been chosen as the material with most potential for further development of visible light active photocatalysts. Besides, DFT calculations for the structures containing combinations of Ni, Co with Nb, V seem, in general, much

more difficult to complete, this is maybe due to the overlap of energy levels of *d* states.

Moreover, it can also be observed from supplementary calculations (not shown) that single site substitutions of 3*d*-metals in the crystal structures (either the *A* or *B* site) show unbalanced electronic structure. The single site Cu substitutions in the *A* site of the crystal structure shifts the Cu 3*d*-band to higher energies. This causes band splitting in the forbidden gap, and, undesirable, localized impurity bands begin to form. This result suggests that the substitution of Cu 3*d*-cations should preferably be made into both sites of the crystal structure to obtain more stable density of states. Thus, the electronic band structure results for BCuN indicate that it could be a suitable material choice for further development of visible light active photocatalysts.

CONCLUSIONS

The optical properties and the electronic structures of various transition metals substituted BZT structure have been systematically investigated using UV-Vis spectroscopy and DFT calculations. It is well know that the LDA and GGA approximations in DFT calculations typically underestimate the band gap energies [27, 28]; yet, in some cases, theoretical and experimental results reach good agreement (such as for Ta compounds) when the structure is assumed to be an ordered solid solution. The band gap values of BCuN and BNiN compounds have been found in the lower energy absorption region. However, both computation and experimental results have shown that BCuN could be suitable material for the development of visible light active photocatalyst.

REFERENCES

1. Tong, H., *et al.*, *Nano-photocatalytic materials: Possibilities and challenges.* Advanced Materials, 2012.

2. Zaleska, A., *Doped-TiO$_2$: a review.* Recent Patents on Engineering, 2008. **2**(3): p. 157-164.

3. Fuerte, A., *et al.*, *Visible light-activated nanosized doped-TiO$_2$ photocatalysts.* Chemical Communications, 2001(24): p. 2718-2719.

4. Zaanen, J., G. Sawatzky, and J. Allen, *Band gaps and electronic structure of transition-metal compounds.* Physical Review Letters, 1985. **55**(4): p. 418.

5. Herrmann, J.-M., *Fundamentals and misconceptions in photocatalysis.* Journal of Photochemistry and Photobiology A: Chemistry, 2010. **216**(2): p. 85-93.

6. Chen, X. and C. Burda, *The electronic origin of the visible-light absorption properties of C-, N-and S-doped TiO$_2$ nanomaterials.* J. Am. Chem. Soc. , 2008. **130**(15): p. 5018-5019.

7. Chen, X. and C. Burda, *The electronic origin of the visible-light absorption properties of C-, N-and S-doped TiO$_2$ nanomaterials.* Journal of the American Chemical Society, 2008. **130**(15): p. 5018-5019.

8. Sheng, Y., *et al.*, *Preparation of N-doped TiO$_2$ visible photocatalyst under low temperature via sol-gel process.* Chinese Journal of Inorganic Chemistry, 2008. **24**(1): p. 78.

9. Huang, W.L. and Q. Zhu, *Electronic structures of relaxed BiOX (X= F, Cl, Br, I) photocatalysts.* Computational Materials Science, 2008. **43**(4): p. 1101-1108.

10. Wang, B., *et al.*, *Band gap engineering in BiNbO$_4$ for visible-light photocatalysis.* Appl. Phys. Lett. , 2012. **100**(18): p. 182102-182102-5.

11. Yin, W.-J*., et al.*, *Band structure engineering of semiconductors for enhanced photoelectrochemical water splitting: The case of TiO$_2$.* Physical Review B, 2010. **82**(4): p. 045106.

12. Almeida, C.G., *et al.*, *Photocatalytic hydrogen production with visible light over Mo and Cr-doped BiNb(Ta)O$_4$.* International journal of hydrogen energy, 2014. **39**(3): p. 1220-1227.

13. Ye, J. and Z. Zou, *Visible light sensitive photocatalysts In$_{1-x}$M$_x$TaO$_4$ (M= 3d transition-metal) and their activity controlling factors.* Journal of Physics and Chemistry of Solids, 2005. **66**(2): p. 266-273.

14. Dvoranova, D., *et al., Investigations of metal-doped titanium dioxide photocatalysts.* Applied Catalysis B: Environmental, 2002. **37**(2): p. 91-105.

15. Kudo, A. and Y. Miseki, *Heterogeneous photocatalyst materials for water splitting.* Chem. Soc. Rev., 2008. **38**(1): p. 253-278.

16. Calaminici, P., *et al., Density functional theory optimized basis sets for gradient corrected functionals: 3d transition metal systems.* Journal of Chemical Physics, 2007. **126**(4): p. 44108-44300.

17. Nisar, J., *et al., Mo-and N-doped $BiNbO_4$ for photocatalysis applications.* Appl. Phys. Lett. , 2011. **99**(5): p. 051909-051909-3.

18. Lim, S.T., *et al., Effects of p-and d-block metal co-substitution on the electronic structure and physicochemical properties of $InMO_4$ (M= Nb and Ta) semiconductors.* Chemical physics letters, 2007. **434**(4): p. 251-255.

19. Zhou, B., *et al., Visible-light sensitive cobalt-doped $BiVO_4$ (Co-$BiVO_4$) photocatalytic composites for the degradation of methylene blue dye in dilute aqueous solutions.* Applied Catalysis B: Environmental, 2010. **99**(1): p. 214-221.

20. Yao, W., H. Iwai, and J. Ye, *Effects of molybdenum substitution on the photocatalytic behavior of $BiVO_4$.* Dalton Transactions, 2008(11): p. 1426-1430.

21. Valant, M. and P. Davies, *Synthesis and dielectric properties of pyrochlore solid solutions in the Bi_2O_3-ZnO-Nb_2O_5-TiO_2 system.* J. Mater. Sci., 1999. **34**(22): p. 5437-5442.

22. Qasrawi, A., B.H. Kmail, and A. Mergen, *Synthesis and characterization of $Bi_{1.5}Zn_{0.92}Nb_{1.5-x}Sn_xO_{6.92-x/2}$ pyrochlore ceramics.* Ceram. Int. , 2012.

23. Qasrawi, A. and A. Mergen, *Structural, electrical and dielectric properties of $Bi_{1.5}Zn_{0.92}Nb_{1.5-x}Ta_xO_{6.92}$ pyrochlore ceramics.* Ceram. Int. , 2012. **38**(1): p. 581-587.

24. Mergen, A., *et al., Fabrication and characterisation of Cr and Co doped $Bi_{1.5}Zn_{0.92}Nb_{1.5}O_{6.92}$ pyrochlores.* J. Am. Ceram. Soc. , 2011. **31**(14): p. 2633-2639.

25. Mergen, A., *et al., Dielectric properties of Sm, Nd and Fe doped $Bi_{1.5}Zn_{0.92}Nb_{1.5}O_{6.92}$ pyrochlores.* Ceram. Int. , 2011. **37**(1): p. 37-42.

26. Du, H., X. Yao, and H. Wang, *Dielectric properties of pyrochlore $Bi_{1.5}Zn_{0.5}Nb_{0.5}M_{1.5}O_7$ (M=Ti, Sn, Zr, and Ce) dielectrics.* Appl. Phys. Lett. , 2006. **88**(21): p. 212901-212901-3.

27.   Perenlei, G., *et al.*, *Electronic structure studies and photocatalytic properties of cubic Bi$_{1.5}$ZnNb$_{1.5}$O$_7$.* International Journal of Photoenergy, 2015. **2015**(575376): p. 1-11.

28.   Perenlei, G., *et al.*, *Synthesis, characterization and electronic structure studies of cubic Bi$_{1.5}$ZnTa$_{1.5}$O$_7$ for photocatalytic applications.* International Journal of Photoenergy, 2015. **2015**(349030): p. 1-8.

CHAPTER   6

GENERAL CONCLUSIONS AND RECOMMENDATIONS FOR FUTURE WORK

6.1 OVERALL CONCLUSIONS

This work contributes to the scientific literature dealing with the engineering of the electronic band structure of complex metal oxides for photocatalytic applications in several ways. The optical absorption, photocatalytic properties and electronic structures of compounds in the Bi_2O_3-ZnO-Nb_2O_5/Ta_2O_5 systems have been explored with both experimental and theoretical methods.

Aiming for photocatalytic application, starting compounds, such as BZN and BZT, have been prepared using different synthetic methods and their properties have been characterised using various techniques. In particular, the diol-based sol-gel reaction, which provides suitable properties, has been successfully employed for the first time to obtain single phase BZT at low crystallisation and sintering temperatures. The phase transformation from precursors to final products as a function of temperature has been studied using various techniques to control the synthesis conditions. Optical properties of BZN and BZT compounds have been characterised using UV-Vis diffuse absorption spectra and their band gaps have been estimated. Other properties, such as crystallite and particle sizes, surface areas and chemical compositions of the parent compounds have also been extensively analysed for optimised photocatalytic properties. The photocatalytic activities of the BZN and BZT compounds have been tested for the decolorisation of organic dye in aqueous solution for the first time. It has found that these catalysts are active under UV light irradiation and the photocatalytic performance of the catalysts for the dye degradation experiments are highly dependent on the properties of the materials, particularly number of active sites on the surface.

This work has also expanded the knowledge of the electronic structures of Bi_2O_3-based complex metal oxides substituted with transition metals using DFT calculations. The CIF structure files of BZN and BZT compounds, obtained from the ICSD database, were used as initial structures for DFT calculations of the electronic band structures. However, DFT calculated using the local density approximation (LDA) or generalized gradient approximation (GGA) approximation band structure for the BZN random solid solution did not display any band gap. This result did not reflect the experimentally observed band gap results. Therefore, this research has subsequently expanded the exploration to different compositions and assumption on the degree of order incorporates new periodicities for the substitutions of Zn cations in the crystal structures of parent compounds.

The new approaches of ordered solid solutions have been investigated for the electronic structures of BZN and BZT compounds with several different combinations of Zn substitutions. Under these new assumptions, DFT calculated band gaps have resulted in much better matches with experimentally measured optical band gap values. The BZT compound shows exceptionally good match between experimental and theoretical band gaps, however, both the LDA and GGA approaches in the DFT calculation for the BZN compound still displays some band gap underestimation, which is, nevertheless, a significant improvement compared to no band gap at all. However, the final structures for the ordered solid solutions obtained were slightly distorted cubic, either orthorhombic or rhombohedral structures.

Since the computational investigations of electronic structures for the parent BZN and BZT structures have revealed the band energies and suggested slight distortions of the cubic structure, this work has then extended the investigation to the effect of additional transition metal substitutions in the structures. This has had a three-fold purpose; (i). to identify further correlation between the experimental values and a consistent theoretical approach; (ii). to find cases where the distortion of the structures may become more obvious; and (iii). to further identify the optimal substitutions to obtain narrow band gap materials suitable for visible light absorption. The overall results obtained from DFT calculations for various combinations of transition metals substituted $Bi_{1.5}MM'_{1.5}O_7$ compounds (M = Zn, Cu, Ni, Co; M' = Ta, Nb, V), have been consistent using identical approaches. This has indicated that the ordered solid solutions may be a better approximation to the other transition metal substitutions in this family of Bi_2O_3-based, complex metal containing pyrochlore compounds.

All transition metal substituted compounds have been experimentally prepared and their structures have been identified by XRD. Diffraction patterns of some of the compounds have been compared with that of BZN to identify the phase formations due to them not being in the diffraction database. The optical band gaps of the compounds have been measured and compared with the DFT band gap values. Blue shifts in the optical absorption edges have been obtained with substitutions of Cu, Ni and Co metals into the BZN and BZT crystal structures. These experimental results have also been consistent with calculated values from DFT and confirm the hypothesis that suitable band gap reductions are viable to make new semiconductor materials, which operate in the visible solar spectrum range. This research has also confirmed that all prepared vanadium (V) containing compounds have orthorhombic

structures, which explains why DFT calculations incorporating V into the cubic structures are difficult to complete. This study however successfully modelled V containing using the orthorhombic structure.

This thesis has presented preliminary structural evidence that BZN and other related compounds may not be cubic and that some degree of structural distortion may be present. This argument has been previously conceived by other researchers, but without further corroborating evidence in the published literature. The structural distortion effect has been more clearly identified in the substitutions of cations with larger ionic radii, such as Cd, in the crystal structure. This has also suggested that very slight splitting in XRD peaks, which on a first pass may be incorrectly attributed to $K\alpha_1$ and $K\alpha_2$ splitting effects, corresponds to slight structural distortion.

Moreover, when partially ordered solid solutions (the cation at either the *A* or *B* sites is randomly substituted, while the other site is ordered, or vice versa) have been assumed for the compounds in the DFT calculations, the geometry-optimized structures have been shown to be cubic. Depending on which site is allowed to remain disordered, a band gap can be retained, which is not too different from those obtained with completely ordered solid solutions. Thus, this later approach of partially ordered solid solution structure allows for the determination of which site (the *A* or *B* site) may display an ordered substitution, resulting in further consistency and improved match between XRD determinations of cubic structures and measurements of electronic band gaps. The computational results have revealed that the ordered solid solution of Zn cations at the *B* (Nb) site of the crystal structure is responsible for the band gap opening, which is maybe due to the overlapping of *d*-orbitals of two different transition metals.

Finally, this thesis has identified important information for the engineering of the electronic band structure of Bi_2O_3-based complex metal oxides, through transition metal doping of original wide band gap semiconductors. The methodology developed also clearly demonstrates that some subtle structural changes have very significant effects, which could hardly be recognizable without the assistance of DFT investigations.

6.2   RECOMMONDATIONS FOR FUTURE WORK

This work has investigated the optical properties and established theoretical DFT tools applicable to a wide range of Bi_2O_3-based pyrochlore structured compounds with substituted transition metals: $Bi_{1.5}MM'_{1.5}O_7$ (M = Zn, Cd, Cu, Ni, Co; M' = Ta, Nb, V). There are several unresolved questions identified by this research.

The newly identified photocatalysts, BZN and BZT materials, have been only examined for catalytic activity in the photooxidative decolouring of organic dyes. For the photodecompositon of dyes, the possible intermediate products without colour in the solution should be further examined using TOC and/or HPLC to monitor the whole reaction process. The photoreduction reaction using BZN and BZT materials also should be tested for solar hydrogen production application via water splitting under UV-light irradiation. This work also provides a good platform for further extension of the work to aspects of photoconduction and recombination effects, which are key aspects for a more complete design of the ideal photocatalyst.

The new types of band gap reduced materials, such as BZV, BCuN, BCuT, BNiN and BNiT, have been prepared by solid-state reaction; however, this research suggests that they should be prepared by an optimised, low temperature sol-gel method in order to examine their photocatalytic properties. The narrow band gap materials should be applied for photocatalytic applications under visible light irradiation, which requires a modified testing protocol to avoid the likely interference from the dye used for the photocatalytic tests using visible light source. Therefore, photocatalytic activity of visible-light-responsive materials should be examined for the decomposition of organic compounds such as phenol or dimethyl sulfoxide (DMSO) under visible light irradiation.

Preliminary evidence of slight distortions in the crystal structures of BCdN and BCdT have been observed due to the substitutions of Zn cations by Cd cations with larger ionic radii. This result should also be further investigated using complementary techniques, such as transmission electron microscopy (TEM), synchrotron XRD and/or neutron diffraction.

In the literature, most metal dopants investigated (Ca, Sr, Ba, In, Cd) have been aimed at and assumed to go exclusively into the *A* site of the BZN structure as $(Bi_{1.5}Zn_{0.5-x}M_x)(Zn_{0.5}Nb_{1.5})O_7$ (x = 0.1 - 0.5) [1-4]. These *A* site substitutions have mainly been experimentally driven and there are no fundamental explanations of their effects beyond a discussion of induced polarization of the crystal lattice associated with displacement of the *A* site by the substitutions [5]. It would be interesting to confirm these reports on a more grounded DFT basis and to make use of different dopants in combination at different sites to get synergistic effects and optimal utilisation of the solar spectrum.

Finally, this research work has shown that the failure of DFT to produce band gaps is not completely attributable to the LDA and GGA approaches [6]. The lack of band gaps appears to be largely due to the random solid solution assumptions in the CIF files from XRD structural determinations. The findings of improved match between experimentally determined and DFT calculated band gaps, together with a predicted and experimentally confirmed, slight structural distortion from cubic structures constitutes a much better starting point for application of the more accurate, but much more computationally intensive, GW method for band gap determinations [7].

6.3 REFERENCES

1. Pang, L.X., D. Zhou, and H. Wang, *Effect of Ca substitution on phase compositions and dielectric properties of Bi_2O_3-ZnO–Nb_2O_5 pyrochlore ceramics.* Ceram. Int. , 2012.

2. Mergen, A., O. Özyoldaş, and İ. Küçük, *Production and properties of In and Ir doped $Bi_{1.5}Zn_{0.92}Nb_{1.5}O_{6.92}$ pyrochlores.* J. Am. Ceram. Soc. , 2011.

3. Du, H. and X. Yao, *Cadmium substituted $(Bi_{1.5}ZnNb_{1.5})O_7$ dielectric ceramics.* J. Mater. Sci., 2007. **42**(3): p. 979-982.

4. Du, H. and X. Yao, *Effects of Sr substitution on dielectric characteristics in $Bi_{1.5}ZnNb_{1.5}O_7$ ceramics.* Materials Science and Engineering: B, 2003. **99**(1): p. 437-440.

5. Wu, M.-C., *et al.*, *Comparison of microwave dielectric behavior between $Bi_{1.5}Zn_{0.92}Nb_{1.5}O_{6.92}$ and $Bi_{1.5}ZnNb_{1.5}O_7$.* Journal of the European Ceramic Society, 2006. **26**(10): p. 1889-1893.

6. Stampfl, C., *et al.*, *Electronic structure and physical properties of early transition metal mononitrides: Density-functional theory LDA, GGA, and screened-exchange LDA FLAPW calculations.* Physical Review B, 2001. **63**(15): p. 155106.

7. Fulde, P., *Correlated electrons in quantum matter*. 2012: World Scientific.